NTNU
Norwegian University of
Science and Technology

Micro-Oscillations in Seismic Signals

An Investigation Into Possible Multi-Bubble Origins

Marcus Bolle Wikstøl

Petroleum Geoscience and Engineering
Submission date: June 2018
Supervisor: Martin Landrø, IGP

Norwegian University of Science and Technology
Department of Geoscience and Petroleum

To my parents, who always indulged and encuraged my childhood fascination of watching water swirl down the bathtub drain.

I might never have pursued a degree in physics if not for those high water bills.

Abstract

Since its first use in the early 20^{th} century, seismic acquisition has become the most utilised method of marine hydrocarbon exploration. At its core, the method relies upon pressure imbalances between a bubble of pressurised air and the water it was released into to create an image of the subsurface: In an idealised world, the interplay between the two would only cause periodic pressure wave emissions of decreasing magnitudes. These are indeed seen in the real world, but they are often superpositioned by a number of weaker oscillations with a higher frequency. Traditionally these have been considered as noise, but a recent survey experiment performed in the Trondheim Fjord indicates that they are highly repeatable. If a theory could predict their behaviour, they could be used to increase the signal-to-noise record in seismic datasets - which in essence is the goal of seismic processing. However, to predict them it is first necessary to ascertain their origin. This thesis is hence an investigation into the possible phenomena and mechanisms that might generate such "micro-oscillations", and deals primarily with two hypotheses:

I The oscillations are created by the precursor "bubble", which forms before the dominant bubble in the system (henceforth referred to as the "main bubble"), and oscillates with its own period. Through its proximity to the main bubble it is subject to large amounts of incident acoustic radiation, which might at every major pressure pulse "charge" it and extend its lifetime.

II The oscillations owe their existence to smaller bubbles which by some process split from the main bubble. Evidence is presented here that the partition might be due to the bubble interacting with the surface.

In order to investigate these hypotheses, bubble oscillation needed to be modelled under a wide range of conditions. With this in mind, a composite bubble dynamics equation was put together by including elements from a number of authors. The main bubble's behaviour was modelled by iteratively solving said equation under the guidance of a genetic algorithm developed for the occasion. Having isolated the main bubble's behaviour,

it was subtracted from the dataset to yield the micro-oscillations. The same inversion-scheme was used to inverse-model these smaller oscillations. Succinctly, the results of said inverse-modelling provide a strong argument for discarding the precursor hypothesis. The precursor, forming before the main bubble, will not retain the high-frequency oscillations otherwise expected from its initial pressure-volume imbalance for long. Rather, it will oscillate at near the same period as the larger bubble whose pressure emissions it is subject to.

If a bubble instead is allowed to form in the interlude between the main bubble's pressure pulses (hypothesis II), inverse-modelling proves it capable of generating some of the micro-oscillations observed. This does not necessarily prove the validity of the bubble spawn hypothesis, but it is a strong point in its favour until a dedicated experiment is performed to investigate it. The most convincing results were produced in the time between the first main bubble expansion and collapse. Worse results were achieved for the post-collapse micro-oscillations: Only the modelling of the deeper dataset treated managed to reproduce the measured signature to an acceptable degree. This drop in correlation might be due to the collapse causing an intensification of bubble spawning through the ensuing turbulence: The increased number of spawned bubbles (potentially of varying sizes) is likely to interact to a higher degree, and their combined signature could not be reproduced by modelling just one of them.

When determining the optimal frequency range for inverse-modelling the micro-oscillations, it was for thoroughness deemed necessary to compare their power spectra to that of an equally long noise record. The datasets available for analysis had, however, had their pre-shot record muted. A process was thus developed to find the time at which the main bubble no longer influenced measurements, and a noise record unbiased by bubble oscillation could be extracted.

Sammendrag

Seismikk ble først tatt i bruk for leting etter olje og gass tidlig i det 20. århundre, og har siden da blitt den mest anvendte metoden på markedet. Den går i hovedsak ut på å slippe ut et volum av svært komprimert luft under vann, og derved generere en boble med et høyere internt trykk en vannet rundt. Ideelt sett ville dette resultert i en periodisk emisjon av trykkbølger med synkende amplituder. Den faktiske oppførselen av et slikt system gjenspeiler tildels dette, men de store trykksvingningene er ofte ledsaget av en rekke mindre svingninger med en høyere frekvens. Disse har tidligere både blitt vurdert og behandlet som støy, men et eksperiment nylig utført i Trondheimsfjorden gir sterke indikasjoner på at de er repeterbare.

En teori som forutså deres oppførsel ville kunne bli brukt til å øke signal/støy-forholdet i datasettene, noe som faktisk er ett av hovedmålene med seismisk prossesering. Denne masteroppgaven er et skritt i denne retningen, og går ut på å undersøke av fenomener og mekanismer som potensielt kan generere slike "mikro-oscillasjoner". Av disse går den hovedsakelig gjennom to hypoteser:

I Oscillasjonene skyldes "forløperboblen" (precursor bubble) som oppstår før hovedboblen, og oscillerer med sin egen periode. Da disse dannes nært hverandre vil forløperboblen motta store mengder akustisk energi som teoretisk sett kan "lade" den, og dermed forlenge dens levetid.

II Oscillasjonene genereres av en rekke mindre bobler som separeres fra hovedboblen mellom hver store trykkemisjon. Bevis blir her presentert for at separeringen forårsakes av interaksjon mellom hovedboblen og overflaten.

For å teste disse hypotesene er det nødvendig å modellere bobleoppførsel under svært varierende omstendigheter. En ny bobledynamikkslikning med mange frihetsgrader ble av denne grunn satt sammen. Hovedboblens oppførsel ble så modellert gjennom å iterativt løse den under styring av en genetisk algoritme utviklet for anledningen. Mikro-oscillasjonene ble isolert ved så å subtrahere bidraget fra den modellerte hovedboblen

fra datasettet. Videre ble disse mindre oscillasjonene forsøkt inversmodellert med den samme fremgangsmåten. Resultatene fra inversmodelleringen gir et sterkt grunnlag for å forkaste den første hypotesen: Forløperboblens nærhet til hovedboblen fører nemlig til at den mister den høye oscillasjonsfrekvensen forventet fra dens initielle volum-/trykkubalanse til omgivelsene. Den vil altså isteden oscillere med samme periode som den større boblen hvis trykkemisjoner den er utsatt for. Gode resultater oppnås imidlertid ved å isteden inversmodellere under antagelsen om at bobler dannes i tiden mellom hovedboblens trykkpulser. Dette bekrefter nødvendigvis ikke den andre hypotesen, men er et sterkt punkt i dens favør til et eksperiment blir utført for å verifisere den. De beste resultatene ble oppnådd tiden mellom starten på hovedboblens første ekspansjon og dens første kollaps. Dårligere resultater ble oppnådd for mikro-oscillasjonene etter den første kollapsenen: Kun modelleringen av det dypere datasettet behandlet klarte å reproduserte den målte signaturen til en akseptabel grad. Den lavere korrelasjonen er antatt å skyldes selve kollapsen da enda flere bobler dannes gjennom den påfølgende kaotiske oppførselen. Dette økte antallet av bobler (potensielt av varierende størrelser) vil trolig påvirke hverandre, og deres kombinerte signatur kunne ikke bli reprodusert ved å modellere en enkelt av dem.

Da de optimale frekvensområdene for inversmodellering av mikro-oscillasjonene skulle bestemmes ble det valgt å inkludere et frekvensspekter av støy for sammenlikning av energier. Datasettene tilgjengelig for analyse hadde imidlertid hatt deres pre-shot målinger satt til null. En prosess ble derfor utviklet for å finne tidspunktet hvor hovedboblen ikke lenger påvirket datasettet, og en støymåling upåvirket av boblesystemet kunne bli isolert.

Acknowledgements

For the first month of this semester I was actually working on another thesis. Due to unforeseen changes in the global strategy of the company I was writing for, this thesis unfortunately had to be abandoned. Given the opportunity here I would like to express my sincere gratitude to Martin Landrø who provided me with this alternate topic of investigation, and in so doing averted a delay to my degree. I am also grateful for all the ideas and suggestions he provided over the course of the semester.

Equinor deserves recognition as well - both for financing the field test, and for granting access to the results for academic research institutions.

I am also very grateful to friends and family lending me an ear for my rubber duck debugging. Lastly, a special thanks goes out to Erik Sullivan, who diligently read through my final draft and fine-combed it for Americanised spellings and typos.

Trondheim, June 2018

Marcus Bolle Wikstøl

Table of Contents

List of Tables

List of Figures

List of Symbols and Abbreviations

Latin Symbols

c_∞	Pressure wave propagation velocity
D	Dataset
f	Frequency
H	Enthalpy at bubble wall
k	Unknown constant
$p(t)$	Internal bubble pressure
$\dot{p}(t)$	Rate of change of internal bubble pressure
$p_{atm}(t)$	Atmospheric pressure
$p_A(t)$	Absolute external pressure outside the bubble wall
$p_{Dyn}(t)$	Incident-/dynamic pressure
$p_{FF}(t)$	Farfield pressure
$p_{NF}(t)$	Nearfield pressure
$p_{Sat}(t)$	Vapour saturation pressure
p_0	Initial internal bubble pressure
p_∞	Hydrostatic pressure

r	Distance between center of bubble oscillation and a point of measurement
R_{Eq}	Equilibrium bubble radius
R_G	Universal gas constant
$R(t)$	Bubble radius
$\dot{R}(t)$	Bubble wall velocity
$\ddot{R}(t)$	Bubble wall acceleration
$S(f)$	Signal in frequency-domain
$S(t)$	Signal in time-domain
t	Time
T_{Boil}	Boiling temperature of water at atmospheric pressure
T_{Sat}	Temperature of water at saturation pressure
v_r	Bubble rise velocity
V_0	Initial bubble volume
w	Weighting

Greek Symbols

α	Damping coefficient
β	Coefficient affecting bubble oscillation period
$\eta(t)$	Proportionality to number of bubble oscillations
κ	Adiabatic index
ρ	Density of given medium
τ	Bubble oscillation period
ΔH_{vap}	Latent heat of vaporisation
Γ	Deviation between datasets
$\Xi(f)$	Power spectrum of signal in the frequency domain
Ψ	Empirical factor to shape bubble pulses

Abbreviations

CFD	Computational Fluid Dynamics
RMS	Root-Mean-Square
$NRMS$	Normalised Root-Mean-Square

Chapter 1

Introduction

1.1 Layman's Introduction to Oil and Seismics

Oil is old. About 70% of all present-day deposits formed during the Mesozoic age, 252 to 66 million years ago, and has therefore been present throughout mankind's existence *(Energy Education, 2006)*. For oil to form, organic matter must first be buried in an anoxic environment, and then exposed to high temperature and pressure for the necessary chemical reactions to occur. Being lighter than water it will, granted a pathway, escape from its source rock and migrate upwards. Without the presence of an impermeable barrier, it might end up surfacing as an oil seep. These are indeed the means by which man first came into contact with petroleum - a contact which has persisted throughout the ages; some historians even date the first use of the substance to 70.000-year-old tool bindings *(Boeda et al., 2008)*.

Skipping forward to the present day, oil has become an integral part of life. As the main fuel for transportation and an important component of everything from plastics to cosmetics, the demand for it has soared: The *International Energy Agency (2018)* predicts the world's average daily consumption of oil for 2018 to be 99.1 million barrels per day. Converted into SI units this is nearly 15.8 million cubic metres - enough to fill over 6300 Olympic-sized swimming pools! Such high demand well exceeds the volumes extractable through seeps, and it is therefore necessary to search for the oil which did not surface, but was trapped (stored) beneath impermeable subsurface barriers in reservoirs. Petroleum prospectors searching for these natural stockpiles have a toolbox of

high-precision geophysical methods available to them. By measuring the apparent values of elastic, electric, magnetic, and gravitational parameters a model of the subsurface can be constructed and interpreted to infer the location and volume of potential hydrocarbon resources. When such prospecting is done offshore, seismic surveying is arguably the method most widely used. In short, this is done by towing a seismic source and listening devices (hydrophones/streamers) behind a ship specialised for the task. At periodic intervals the source emits an acoustic signal which then propagates through the ocean and, upon reaching the seafloor, into the subsurface. Through interaction with geological structures some of the signal is refracted, diffracted or reflected. Consequently, a fraction of the emitted energy will return to the surface, and become registered by the streamers. The data gathered is later processed, and turned into a model of the underground geology. The topic of interest for this master thesis are the direct signals, meaning those that have not yet propagated into the subsurface. Two measurements of these have been included, and overlay each other in Figure 1.1.

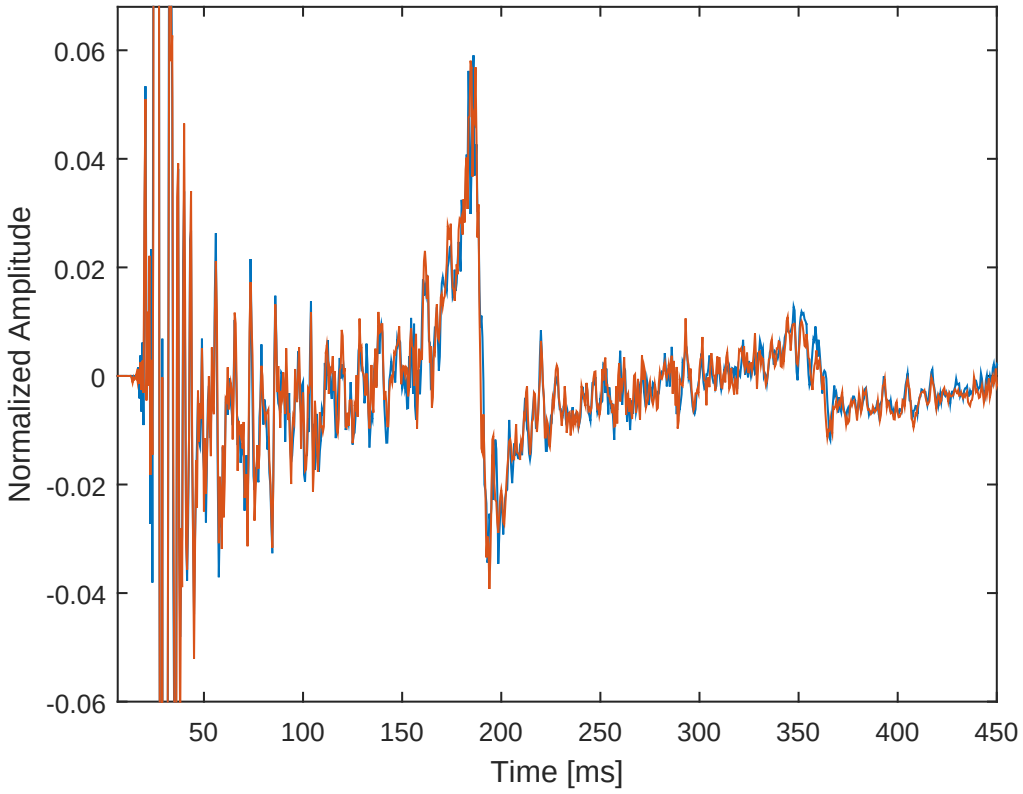

Figure 1.1: Unprocessed (raw) measurements taken with the source at 3 metres depth, showing high repeatability both at the macro- and micro-level.

Direct wave signals are time-variant, with the majority of the energy being radiated as the bubble expands from its radial minimum. These two signals were created under the same experimental conditions (depth, internal pressure, instrument setup, etc.) and their macro-behaviours are, as expected, nearly identical. Rather more surprising is the close match in oscillation at the microscale: While commonly attributed to be non-repeatable noise, Figure 1.1 seems to indicate that the micro-oscillations superpositioned on the larger pressure cycle are repeatable signals. It is the aim of this master thesis to investigate their nature and ascertain their origin.

1.2 Acquisition Setup and Thesis Data

Data for this thesis were acquired on the vessel "Gunnerus" during a field test in the Trondheim Fjord. A dynamic positioning system kept the craft stationary over the course of the operation, which was carried out during excellent weather conditions to reduce the amount of ambient noise. Reducing noise is also the appeal of performing signal tests in fjords in the first place, as they are generally more quiet than the open sea. The signal-to-noise ratio was further improved by using a relatively large air gun (600 in^3). Due to the water depth at the acquisition site (approximately 390 m), the water-layer multiple is registered after the signal of interest.

The air gun and hydrophone were attached to the same wire 20 metres apart, and kept vertically aligned using a weight. 36 shots were fired at depths spanning 3-40 metres, with a recording window of 10 seconds. All depths are approximate, and the magnitude of any errors thus becomes relatively greater closer to the surface. As such, deeper shots were used to fix global parameters such as water velocity, etc. The sampling frequency of the survey was 2000 Hz, corresponding to a timestep of 0.0005 seconds. For a visual illustration of the setup of the experiment and the tools used, see Figures 1.2 and 1.3.

It should be noted that the survey was not performed for the purposes of this thesis, but rather spawned it through the high repeatability of the data acquired. For the purposes of this investigation there were hence a few shortcomings which needed to be overcome: The "raw" data did undergo some on-board processing, and therefore does not contain pre-shot noise. It has also been normalised, and the absolute values of the pressure readings have thus been lost. Furthermore, a causal filter has been applied, delaying output samples best representing inputs, and shifting polarities. This has a number of applications (estimation of noise from post-shot data, ignoring certain signal parts) which will be discussed later.

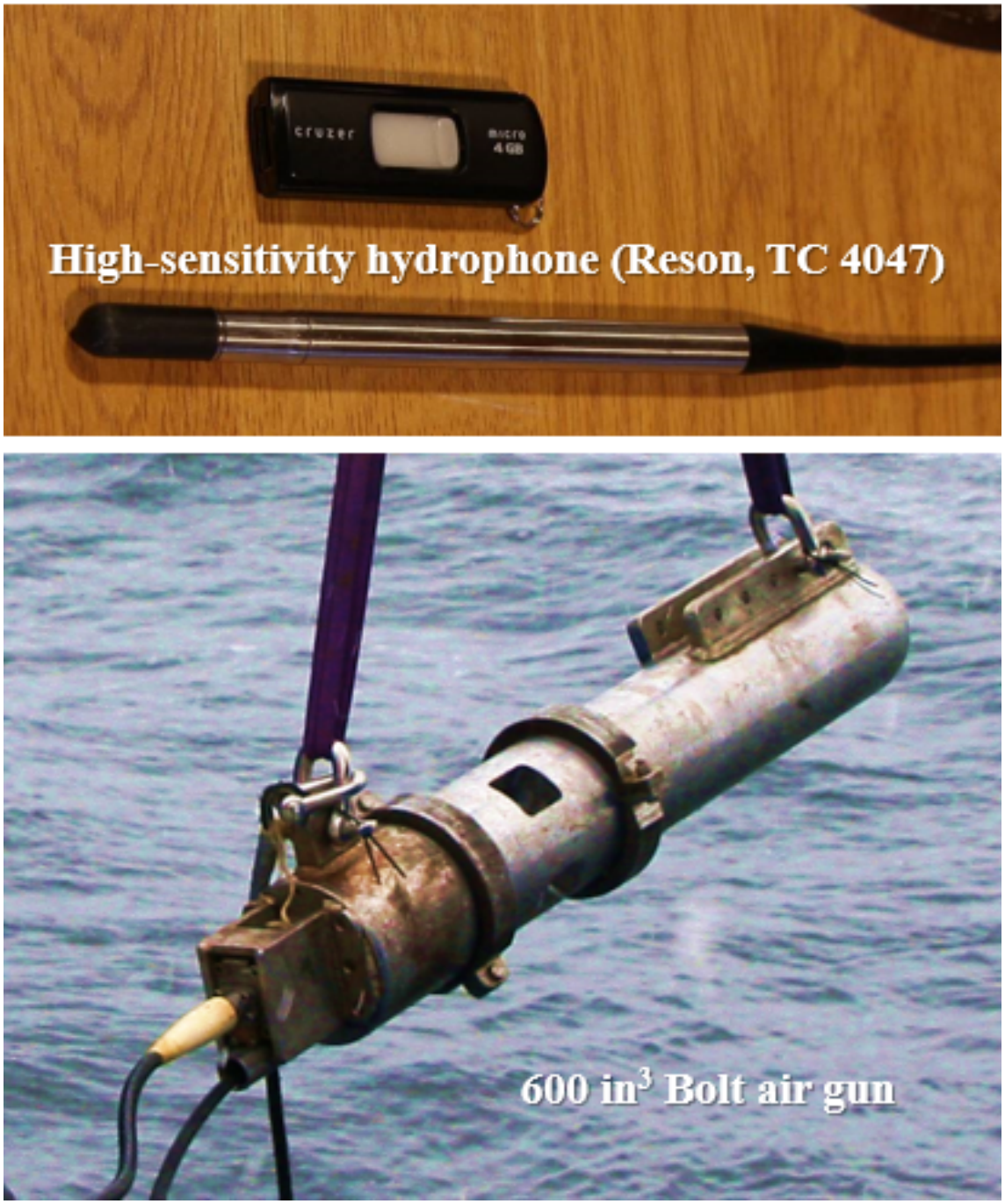

Figure 1.2: Photographs taken during the survey of the instruments used to generate and record the seismic data analysed in this thesis. The memory stick is included to give an indication of scale. Both images courtesy of *Pedersen (2009)*.

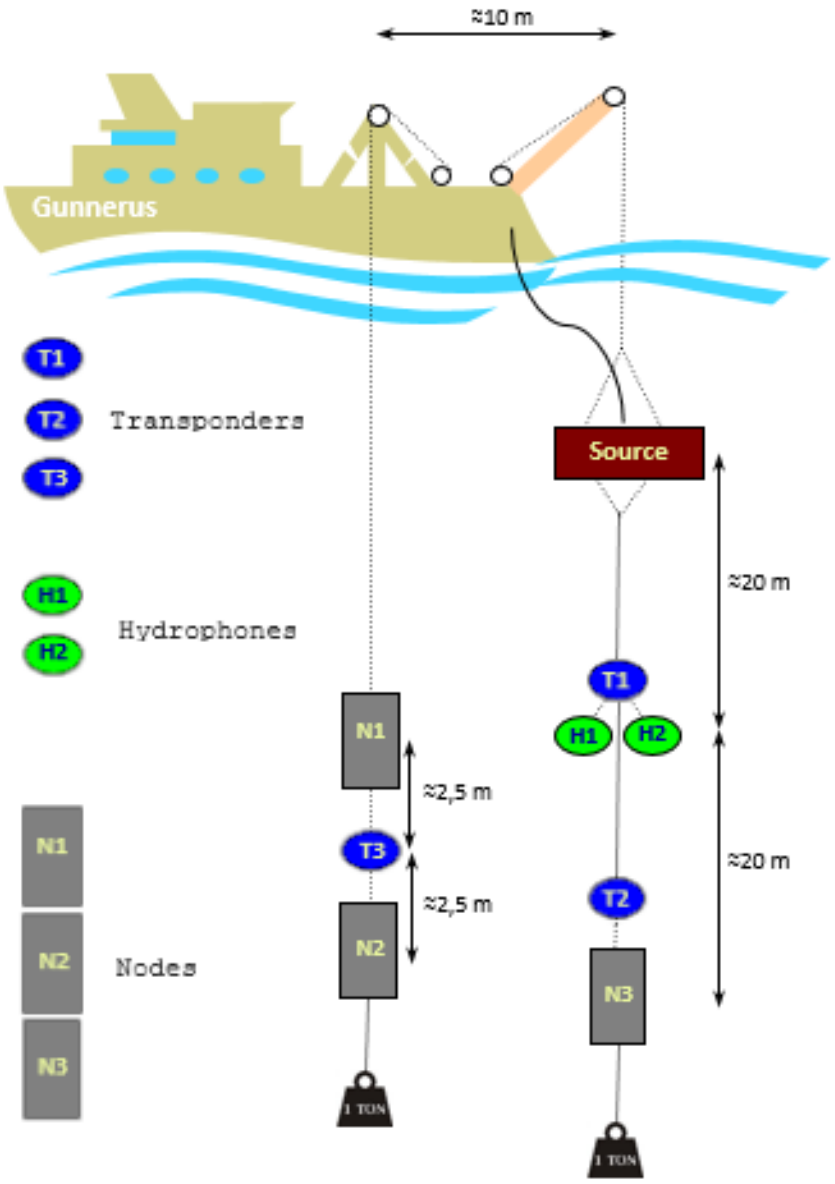

Figure 1.3: Instrument setup of the survey. Data gathered from the 4C autonomous nodes/transponders was not made available for the purpose of this thesis. Image modified from *Pedersen (2009)*.

Chapter 2

Theory

One of the most important distinctions to make in signal processing is the difference between seismic data and noise. Many definitions of these two classifications exist, but separation between them is often done on the basis of origin and repeatability: Seismic data can be reproduced under the same initial conditions if generated by a seismic source. If a data point is generated by another outside phenomenon, it is often non-repeatable and is considered a contaminant. In theory, there is nearly an infinite variety of noise sources in the ocean. Besides the intuitive ones such as wind, waves, currents, marine life, rain, equipment vibration, and mechanical noise, it is also necessary to take into account incident anthropogenic noise from, for example, other crafts. Noise source categorisation within a dataset is no easy task, but inferences can be made on the basis of energy distribution across various frequency ranges. This is found through calculating the so-called power spectrum $\Xi(f)$, or the spectral density, of the signal S following the formula in Eq. (2.1).

$$\Xi(f) = \frac{1}{N}\left|S(f)\right|^2 = \frac{1}{N}\left|\sum_{t=1}^{N} S(t)e^{(t-1)(f-1)(-2\pi i/n)}\right|^2 \tag{2.1}$$

This is essentially Fast Fourier transform of the signal squared, and divided by the its length. Doing an equivalent operation in the time-domain (squaring the amplitude) yields a rough estimation of the energy distribution over time.

The seismic source utilised to create the (repeatable) seismic data is usually a so-called "air gun", which in a nutshell is a canister of highly compressed air. Towed at depth below the surface it will, upon firing, evacuate its contained air into the surrounding water

through four ports along its axis. The four resulting bubbles promptly coalesce into one single bubble, which expands rapidly as its internal pressure exceeds the hydrostatic Pressure. Such expansion then invariably imparts an outward momentum on the surrounding water, and causes the transmission of a pressure pulse. Analogous to the classical mass-spring system, the outward momentum forces the bubble to overshoot its equilibrium radius, and oscillation about this stable value ensues until one of three scenarios occur: Oscillations may ground to a halt by energy dissipation, the bubble may lose its cohesion and break up, or it may reach the surface and vent into the atmosphere.
The bubble behaviour, and thus indirectly the characteristics of the emitted signal, is heavily influenced by the pressure surrounding the bubble. This pressure is predominantly a function of the source depth, but is also affected by incident acoustic energy from (nearby) reflections and other bubbles. Most work on the topic of bubble behaviour has, however, been done on the simple, one-bubble-system. The following subsection will introduce a number of findings which nevertheless tie in with a multiple-bubble thesis hypothesis.

2.1 Air Gun Bubble Behaviour

The next section offers a short introduction to the history of bubble oscillation modelling while delving deeper into the actual modelling done in this thesis. By drawing on the works of others, this section focuses more on the observed bubble behaviour rather than on its modelling. Of particular importance to this thesis is *Langhammer and Landrø (1996)*. In this article, Langhammer et al. used high speed photography to visually study oscillating bubbles generated by a 1.6 inch^3 Bolt air gun. A subset of the photos taken has been included in Figure 2.1. While the volume of the gun used by *Langhammer and Landrø (1996)* was considerably less than that of this thesis, their designs are comparable.

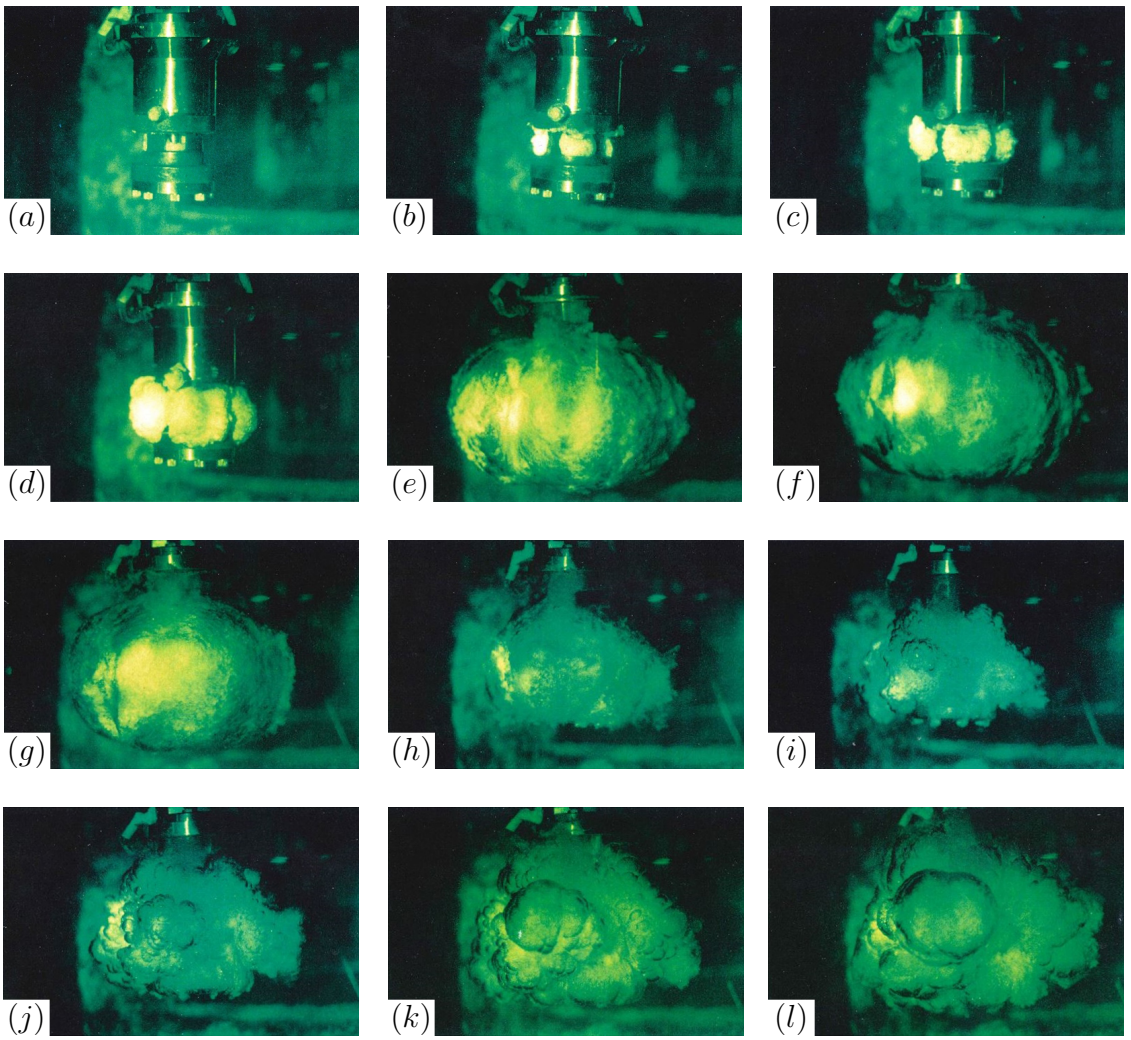

Figure 2.1: High-speed photographs taken over the first and second oscillations of the main bubble formed by a 1.6 inch^3 Bolt air gun. The gun was fired with an initial pressure of 100 bars. Notice especially the turbulent behaviour after the first collapse. Each image has been labelled with a letter (a)-(l) to mark the point in time at which the photo was taken. For exact timing see Figure 2.2. All photos produced with permission by Martin Landrø from *(Langhammer and Landrø, 1996)*.

An attempt at modelling the bubble in Figure 2.1 was carried out by inserting Langhammer and Landrø's initial conditions into Eq. (2.6). The resulting bubble radius, displayed in Figure 2.2, closely match those found by in the original study, lending credence to the fidelity of the applied algorithm.

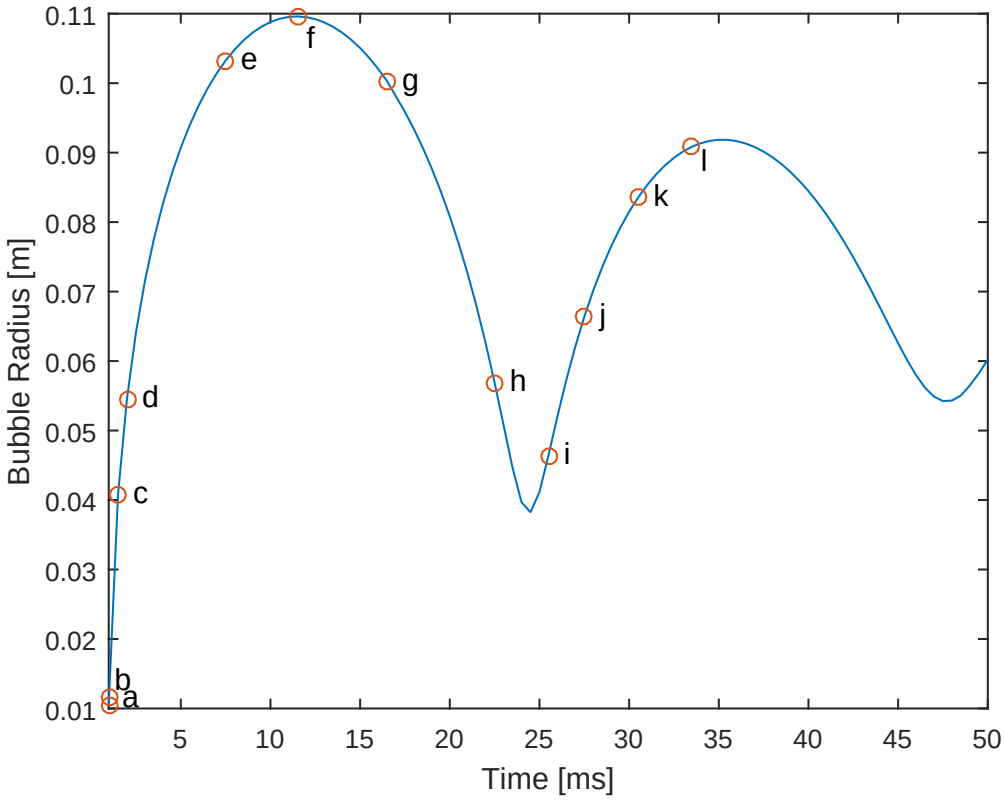

Figure 2.2: Bubble radius modelled under the conditions put forth in *Langhammer (1994)* using Eq. (2.6). The labelled points *a*-*l* correspond to the likewise labelled images in Figure 2.1.

To explain the phenomena observed, it is necessary to delve deeper into the actual workings of an air gun. Figure 2.3 is a cross-section of a typical example of such an instrument, and illustrates its operation: The gun is comprised of two air chambers - the operating chamber (top) and firing chamber (bottom). High-pressure air is supplied to the former by a compressor on-board the seismic vessel via a hose, and it slowly seeps into the lower chamber through the shuttle. Before firing, the downward force exerted on the shuttle thus cancels out or slightly exceeds the upward force exerted by the air in the firing chamber, keeping the shuttle in a sealed position. The gun fires when an electric pulse is sent to its solenoid valve. Upon receiving this pulse it vents a small quantity of the air in the operating chamber, and the pressure in the firing chamber becomes dominant. This accelerates the shuttle upwards, allowing air to escape through the ports and into the water. Once enough air has escaped for the air pressure in the control chamber to become dominant, the shuttle is promptly forced back into its original position - cutting off the flow. As the shuttle re-seals the ports, gun dynamics should no longer affect the bubble, and free os-

cillation ensues. Still, sudies such as *Groenaas et al. (2016)* have noted that the shuttle of the Bolt model air guns may repeatedly bounce, causing a number of air re-injections into the water before completely sealing the firing chamber. Still, these latter air injections are relatively small, and should not have a significant impact on the macro-signal. Due to the time it takes for the shuttle to bounce up from its locked position (approximately 175 ms for the 155 inch^3 air gun used by *Groenaas et al. (2016)*) they are also unlikely to cause the micro-oscillations which arise immediately after the primary and ghost in Figure 1.1 (see Section 2.1 for definitions).

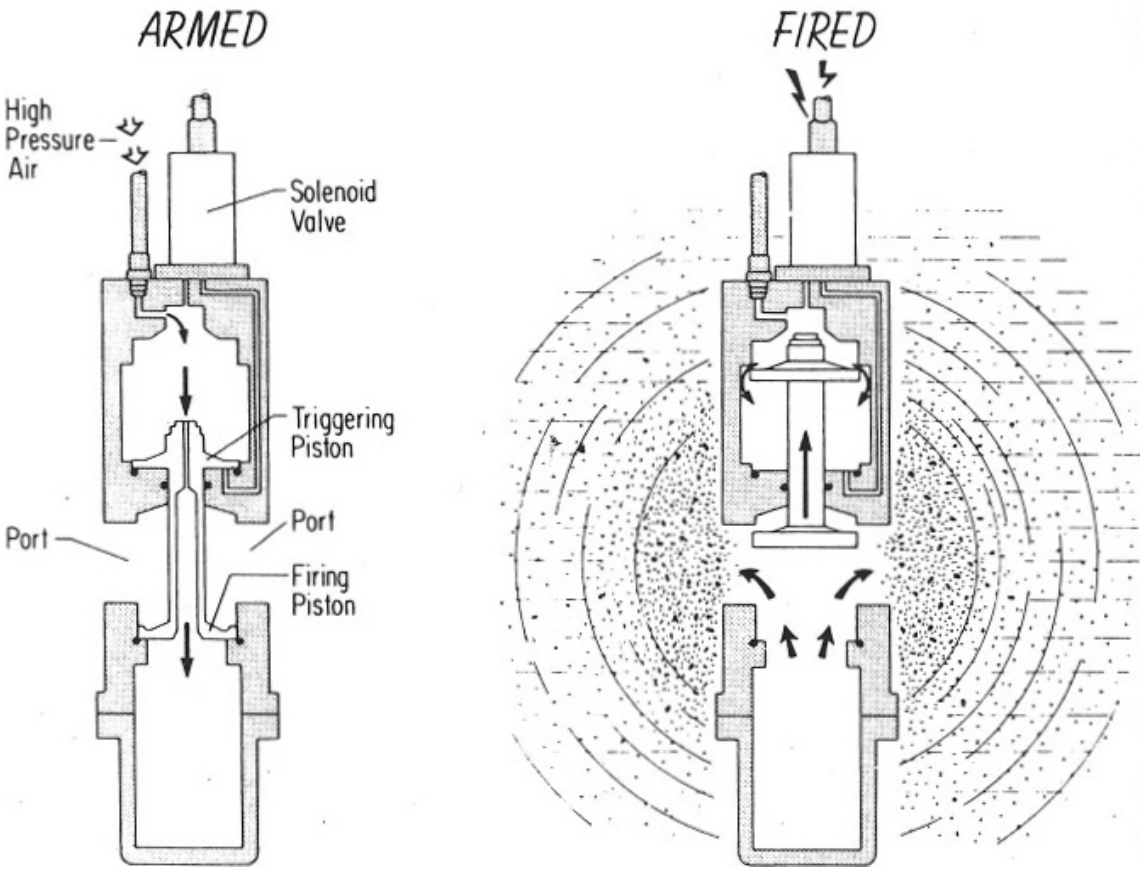

Figure 2.3: Cross-section of an air gun and its operation. Image reprinted with permission from Springer Nature: Marine Geophysical Research *(Hutchinson and Detrick, 1984)*.

2.1.1 The Precursor Hypothesis

Neither Figure 2.3 nor incomplete venting do, however, explain the generation of the smaller bubble (henceforth referred to as the "precursor") seen in subplot "(a)" of Figure 2.1. According to *Groenaas et al. (2016)*, it is formed in the time between the shuttle starting to move and it reaching the ports. More specifically, it is formed by air escaping through an "*annular gap between the shuttle and the surrounding housing*". This annular gap is small, and is a included in the design as trade-off between "*[minimising] acoustic noise, and preventing mechanical contact between moving parts that would cause wear and compromise reliability*". While the precursor was absorbed by the main bubble in the study by Langhammer et al, it is possible that the precursor of the larger air gun used in the survey remains a separate entity. Although this needs to be verified experimentally, the slightly altered configuration of the larger gun might have displaced the annular gap sufficiently far from the ports for the bubble walls to never come into physical contact. Still, as previously touched upon, the bubbles still interact. Like the main bubble, the precursor also oscillates due to a pressure/volume imbalance with regards to the absolute exterior pressure p_A. However, for the precursor this pressure is significantly influenced by acoustic radiation (dynamic pressure pulses, p_{Dyn}) from the main bubble, in addition to the hydrostatic pressure p_∞. In other words, it becomes time-variant:

$$p_A(t) = p_\infty + p_{Dyn}(t) \tag{2.2}$$

According to *Ronald (1999)*, the resulting effect on the precursor can be a net gain of energy. In turn, this could allow it to continue oscillating, and emitting of its own pulses well beyond the time it would be able to do so alone in an infinite water domain. The precursor's proximity to the main bubble may also induce relative translation, time-variant share forces, and shape changes. Some of these are exceedingly hard to model in a programming platform like MATLAB; and any study devoted to quantifying their effect should opt for a dedicated CFD-software to do so (computational fluid dynamics).
Due to the dominance of the main bubble in the oscillatory system described, the influence of the precursor on its behaviour is assumed negligible.

2.1.2 The Bubble Spawn Hypothesis

Another possible hypothesis for the micro-oscillations is that they are caused by bubbles spawned by the actions of the main one. There are many potential methods by which these smaller bubbles may form: Revisiting Figure 2.1, many are clearly generated by the first collapse. Other high-speed photography studies such as *de Graaf et al. (2014)* investigate this further:

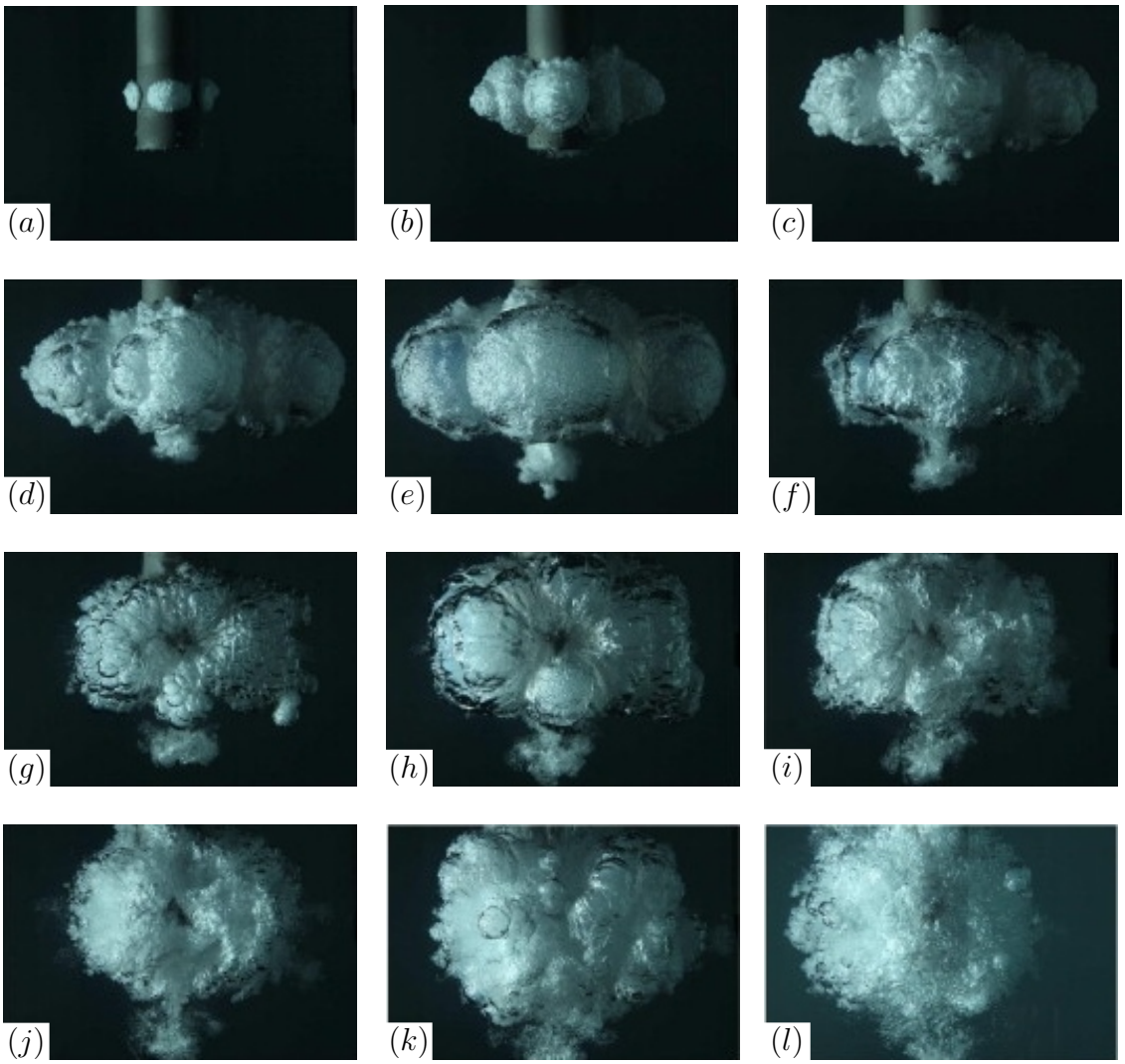

Figure 2.4: High-speed photographs of a bubble generated by a 0.885 inch^3 air gun fired at an initial pressure of 100 bars. Image reprinted from *(de Graaf et al., 2014)* with permission from Elsevier. The labelling of the figure is not to be confused with that of Figures 2.1 and 2.2. In short, $(a) \rightarrow (f)$ display the initial bubble formation, growth, and collapse. $(g) \rightarrow (h)$ and $(i) \rightarrow (k)$ show the first and second free-bubble oscillations. At point (l) the bubble is at its fourth growth-phase, but has been broken up into a cloud of bubbles.

For image (a) in Figure 2.4, the perturbations seen are hypothesised to be due to the

Rayleigh-Taylor instability which may form at interfaces where a light fluid displaces a more dense one. This effect is, however, dominated in the later photos by the violent airflow through the ports driving the bubble growth. In their paper, de Graaf et al. estimated the Reynolds number of said airflow to be in the vicinity of 1×10^7, well into the turbulent domain. From Figure 2.4 (b)-(d) it is hence possible to hypothesise that turbulence would cause the detachment of one or more smaller bubbles, which could then oscillate at their own natural frequencies. Nevertheless, it should be noted that both Langhammer et al. and de Graaf et al. worked with air guns considerably smaller than that used this study, and it is conceivable that neither of the behaviours seen scale with firing chamber-volume. Whether this effect is more prevalent on a larger air gun remains a topic for further investigation.

A strong counterpoint to the idea of turbulence causing the early micro-oscillations can be made as the bubble wall is relatively smooth at its first radial maximum (see Figures 2.1(e) and 2.4(e)): From Figure 1.1 one expects the micro-oscillations to be emitted throughout all parts of the main bubble's oscillatory cycle. Another speculation which takes into account this issue can also be made on the basis of *de Graaf et al. (2014)*. In addition to investigating (relatively) unperturbed oscillation they also studied the effect of nearby boundaries on an air gun bubble. If a shot is fired near the surface, what appear sudden drops in pressure will be recorded at regular intervals from the pressure peaks. These are called ghosts, and are the reflections of acoustic signals off the sea-water interface. Their mathematical foundation will be handled in Section 2.2, but of particular concern for this thesis is their effect on the main bubble itself: Figure 2.5 illustrates the effect of a down-going ghost on a bubble close to the surface.

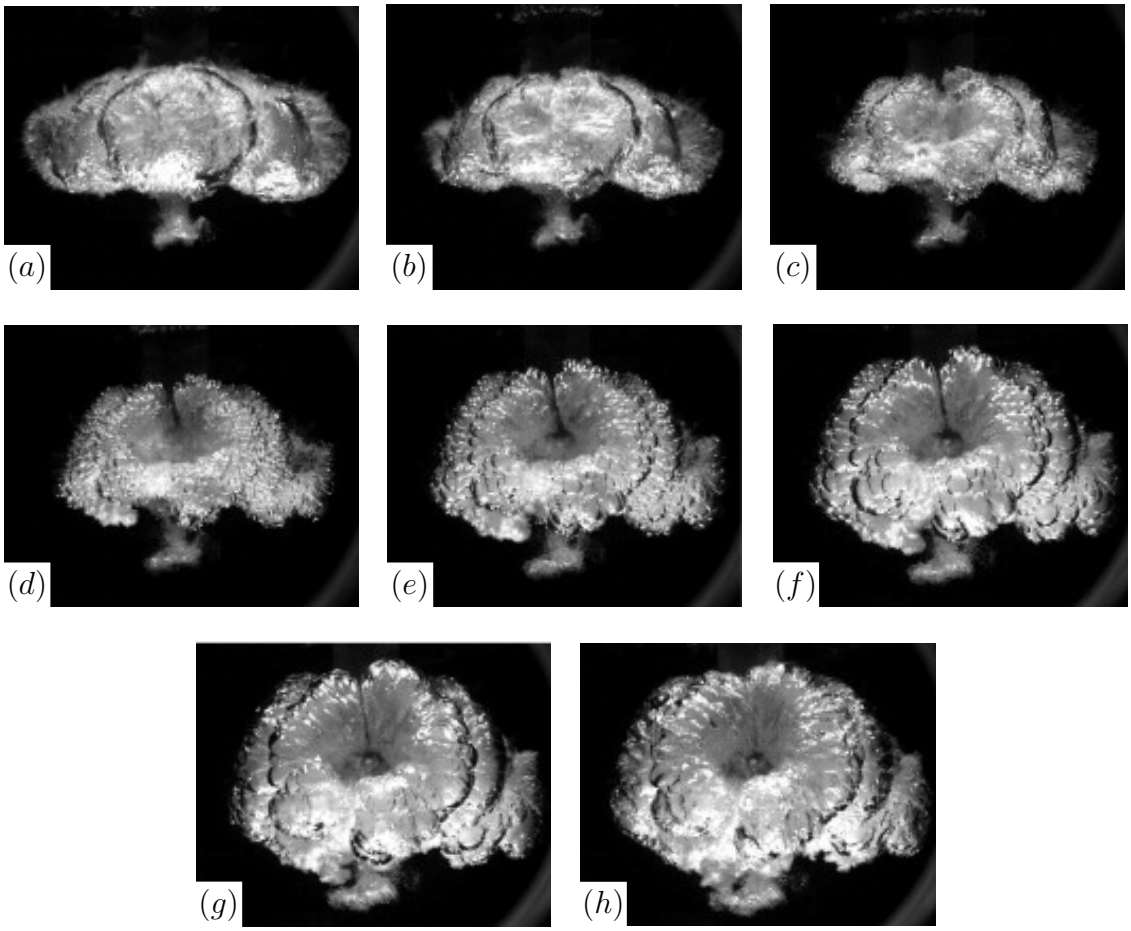

Figure 2.5: A ghost striking a bubble when it is at its first radial maximum. The bubble was generated using the same 0.885 in^3, 100 bar gun as Figure 2.4. Image reprinted from (de Graaf et al., 2014) with permission from Elsevier.

As can be discerned, in this experiment the ghost reaches the bubble when it is close to its maximum size. Upon contact a re-entrant jet forms away from the free surface, splitting the main bubble and forming a cascade of smaller ones. As these bubbles have a different internal pressure from the main bubble, they will oscillate at a higher frequency. The larger gun used in this study creates a bubble with a longer period than that of de Graaf, and such interaction can be assumed to happen already in the initial growth-phase for the shallower depths. Bubbles being formed by ghosts in this fashion may theoretically oscillate without much outside influence until the next main bubble expansion. Thus, they can be modelled using a surrounding pressure close to the hydrostatic. As already pointed out, the first collapse assists in breaking the bubble apart by increasing the turbulence in the surrounding water *(Langhammer et al., 1995)*. As they are generated by the combination of two influences and shaped by their interplay, the post-collapse micro-oscillations

are likely to be more complex, and harder to reproduce through modelling than the pre-collapse ones.

If the micro-oscillations were present in the pressure measurements made over the course of de Graaf's tests, they are likely to have been masked by the reverberations of the tank wall, and removed alongside them by the filtering applied. As academic bubble research has largely been done with air guns placed in tanks, such wall reverberations could conceivably be the reason as to why repeatable micro-oscillations have not previously been investigated in detail.

2.2 Air Gun Bubble Modelling

Investigations into the physics of bubble dynamics has a long and interesting history, and is considered by many to have begun with *Rayleigh (1917)*. In the comprehensive paper referenced, Rayleigh ascribed the sounds made by boiling water to the collapse of (steam) bubbles as they rose towards the surface. By so doing, he also derived Eq. (2.3), which is now known as the "Rayleigh equation".

$$\frac{p(t) - p_\infty}{\rho} = R(t)\ddot{R}(t) + \frac{3}{2}\dot{R}(t)^2 \tag{2.3}$$

This equation describes the time-dependent radius $R(t)$ and internal pressure $p(t)$ of a spherical bubble in an incompressible medium of density ρ, exposed to a hydrostatic pressure of p_∞ ($p_A(t)$ if accounting for incident pressure pulses). Throughout this thesis, time derivatives are denoted by "˙", making $\dot{R}(t)$ and $\ddot{R}(t)$ the bubble wall velocity and acceleration respectively. A later great advance was made by *Ziolkowski (1970)*: For any bubble with a stable equilibrium radius R_{Eq}, its internal pressure is at any point in time determined by Eq. (2.4).

$$p(t) = p_\infty \Big(\frac{R_{Eq}}{R(t)}\Big)^{3\kappa} \tag{2.4}$$

The exponent κ is known as the adiabatic index, and may for air - a predominantly diatomic gas - take on values between 1.0 and 1.4. These two limits describe either perfect heat transfer (between the bubble's air and the surrounding water), or none at all. In other

words, the cycles of bubble expansion and contraction can either occur isothermally, adiabatically, or somewhere in-between these two extremes. Ziolkowski estimated its value "*for most air guns*" (bubbles) to be in the vicinity of 1.13, and κ has been set accordingly in the modelling. Still, the air gun employed for this thesis is much larger than those used by Ziolkowski, and its true κ-value is likely to be higher.

Since Rayleigh's time many other equations describing bubble dynamics have been developed. The method adopted for this thesis will nevertheless be based mainly on Rayleigh's work, incorporating some modifications from other authors to increase fidelity. One of these modifications can be traced back to *Johnson (1994)*, and is the inclusion of the term $\dot{p}(t)/(\rho c_\infty)$, where c_∞ is the pressure wave propagation speed. Replacing $\dot{p}(t)$ with the time-derivative of Eq. (2.4) and inserting an empirical factor Ψ to shape bubble pulses, the new bubble dynamics equation becomes

$$\begin{aligned}\frac{p(t)-p_\infty}{\rho} &= R(t)\ddot{R}(t)+\frac{3}{2}\dot{R}(t)^2+\frac{\dot{p}(t)}{\rho c_\infty}\Psi \\ &= R(t)\ddot{R}(t)+\frac{3}{2}\dot{R}(t)^2-\frac{3\kappa p_\infty}{\rho c_\infty}\frac{\dot{R}(t)}{R(t)}\Big(\frac{R_{Eq}}{R(t)}\Big)^{3\kappa}\Psi.\end{aligned} \tag{2.5}$$

Based on the work of *Kirkwood (1942)* and *Landrø (1992)*, the last additions to the operating equation are $\alpha\dot{R}(t)$ and $(\beta_1+\beta_2 t)\dot{R}(t)^2$, influencing damping and bubble oscillation period respectively, and yielding Eq. (2.6).

$$\begin{aligned}\frac{p(t)-p_\infty}{\rho} = R(t)\ddot{R}(t)+\frac{3}{2}\dot{R}(t)^2-\frac{3\kappa p_\infty}{\rho c_\infty}\frac{\dot{R}(t)}{R(t)}\Big(\frac{R_{Eq}}{R(t)}\Big)^{3\kappa}\Psi \\ -\alpha\dot{R}(t)-(\beta_1+\beta_2 t)\dot{R}(t)^2\end{aligned} \tag{2.6}$$

Succinctly, Eq. (2.6) describes how the bubble's characteristics (e.g. internal pressure, radius, etc.) changes over time. Following the derivations of *Keller and Kolodner (1956)*, it is possible to use these to estimate the dynamic pressure caused by bubble oscillation with centre a distance r from the measurement. The dynamic pressure is commonly decomposed into a farfield and nearfield component such that

$$p_{Dyn}(t) = p_{FF}(t)+p_{NF}(t). \tag{2.7}$$

Excluding the function arguments to improve readability, these components are

$$p_{FF} = \rho \frac{R}{r}\Big(H + \frac{\dot{R}^2}{2}\Big), \tag{2.8}$$

and

$$\begin{aligned} p_{NF} = -\frac{\rho}{2c^2}\frac{R^2}{r^2}\Bigg(&\frac{R^2}{r^2}\Big(c\dot{R} - H - \frac{\dot{R}^2}{2}\Big)^2 + \big(H + \frac{\dot{R}^2}{2}\big)^2 \\ &+ \frac{2R}{r}\Big(H + \frac{\dot{R}^2}{2}\Big)\Big(c\dot{R} - H - \frac{\dot{R}^2}{2}\Big)\Bigg), \end{aligned} \tag{2.9}$$

where H is the enthalpy at the bubble wall. It is itself largely dependent on the internal pressure, and is calculated following Eq. (2.10).

$$H = \int_{p_\infty}^{p(t)} \frac{dp}{\rho} \approx \frac{p(t) - p_\infty}{\rho}, \tag{2.10}$$

If working independently from the starting conditions in *Keller and Kolodner (1956)* when deriving the farfield and nearfield terms, Eqs. (2.8) and (2.9) are the final results. However, within their own derivation Keller et al. drop many terms without thoroughly investigating their relative magnitudes: In calculating the farfield, enthalpy is neglected[1], and in Eq. (2.9) all terms to order c_∞^{-1} are dropped - yielding the revised Eq. (2.11).

$$p_{NF} = -\frac{\rho}{2}\frac{R^4}{r^4}c^2\dot{R}^2 \tag{2.11}$$

Not taking these approximations at face-value, their validities were investigated by calculating the relative sizes of the neglected terms using the shot fired in Figure 4.5.

For the farfield equation it is from Figure 2.6 evident that the enthalpy-term dominates the one related to bubble wall velocity. Although smaller on average, this latter term still provides an important contribution around radial maxima where the internal pressure is less than the external, and should thus also be included. Equation (2.8) is hence chosen in favour of the farfield-formula derived by Keller et al.

[1] Keller et al. actually also make a small mistake, writing Eq. (2.11) as $p_{FF} = \rho R^2 \dot{R}/r$, which through dimensional analysis is easily seen to be wrong ([kg /ms] instead of [kg /ms^2].

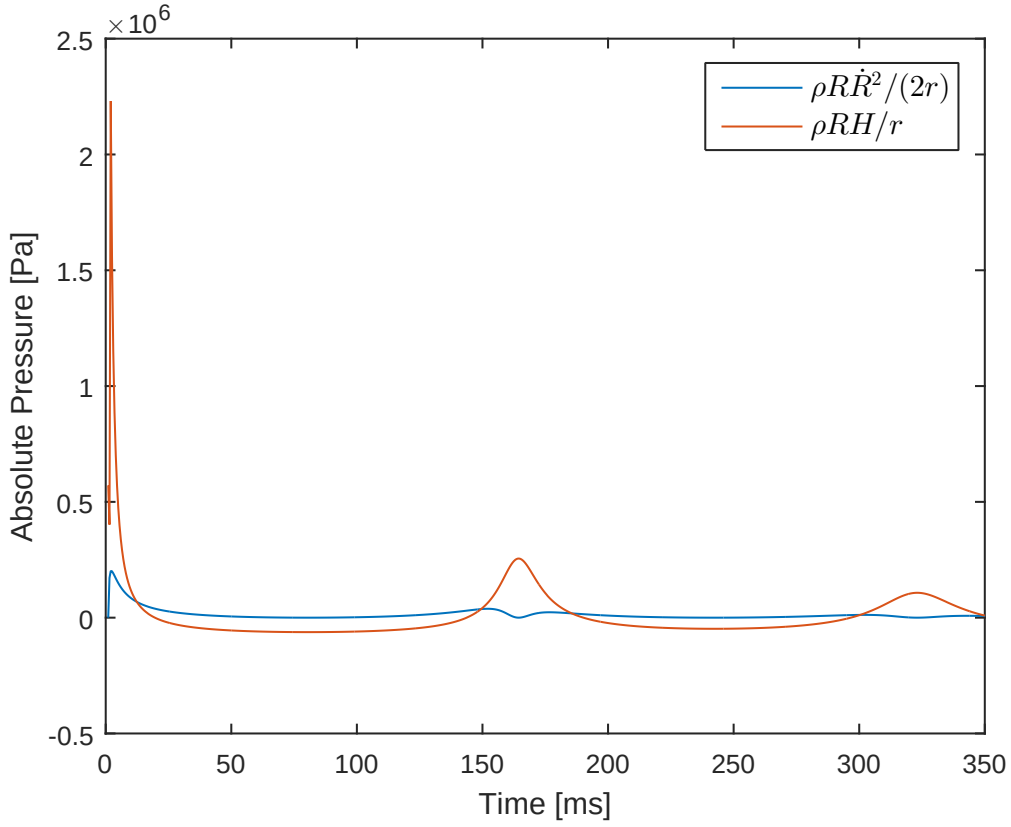

Figure 2.6: Relative magnitudes of the components in Eq. (2.8) for a typical bubble generated by a seismic air gun at a distance of 0.5 metres from the bubble wall. Their sum are displayed in the lower plot of Figure 4.12.

When investigating the approximations made to get to Eq. (2.11) it is arguably only necessary to investigate the relative magnitudes of $c^2\dot{R}^2$, $c\dot{R}H$ and H^2 as one, or a combination of these will invariably dominate the signal. Figure 2.7 is a plot of these, and provides ample support for discarding all terms in Eq. (2.9) to order c_∞^{-1}. Hence, the second approximation done by Keller et al. was adopted, and Eq. (2.11) was hence chosen as a favourable trade-off between fidelity and speeding up computing time.

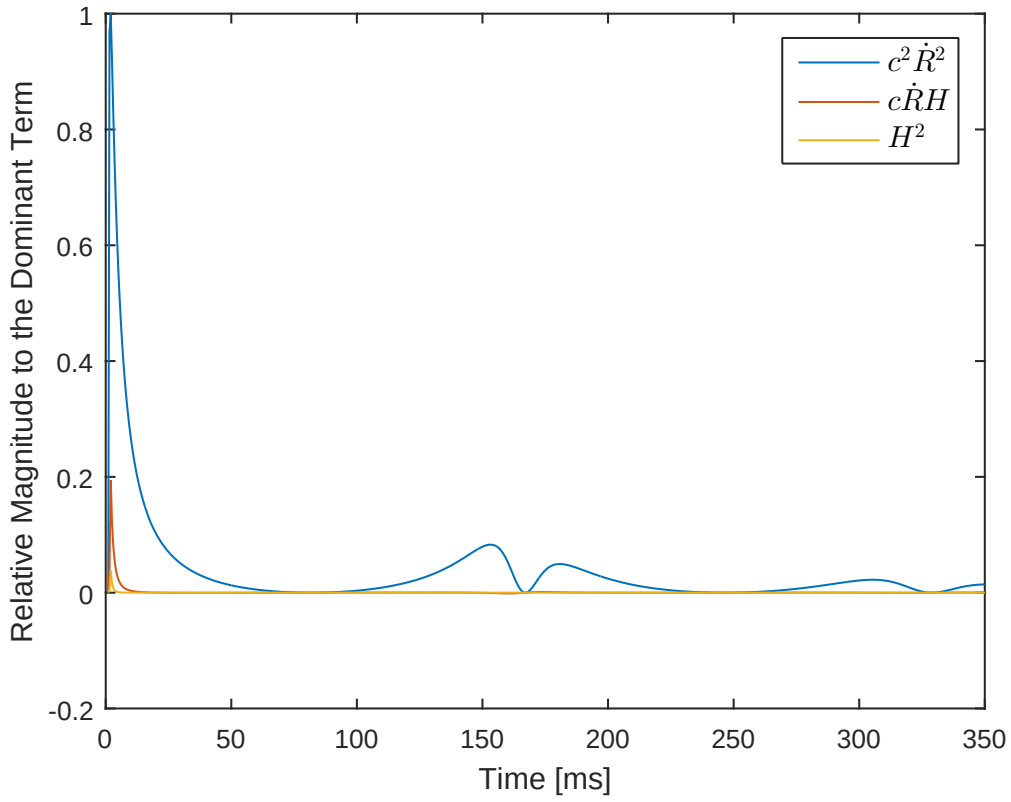

Figure 2.7: Relative magnitude of the three dominant terms in the nearfield equation's kernel at a distance of 0.5 metres from the main bubble's wall.

There is, however, some controversy on the validity of including the nearfield-term (sometimes called the afterflow-term) in modelling at all. One of the papers arguing for its exclusion was written by *Ziolkowski et al. (1984)*, which stated that the marriage between Bernoulli's equation and the wave equation in deriving it is unlawful. As put in his article: "*The problem is that the wave equation and Bernoulli's equation are not compatible. The wave equation, with constant speed of sound, is valid for linear elastic fluids in which the particle velocity is very small. The Bernoulli equation does not depend upon infinitesimal deformations, and it is applicable in a much wider sense than the linear wave equation*". For thoroughness, this thesis investigated the precursor hypothesis (where incident acoustic radiation is a concern) both including and excluding Eq. (2.11) in the modelling.

From both Eq. (2.8) and Eq. (2.11) it is easily seen that the strength of the emitted acoustic signal scales with internal bubble pressure at the point of maximum compression. Consequently, the highest pressure peak (called the "primary") will originate from the main bubble upon its release from the firing chamber. When reaching the sea-water interface both the primary and later pressure pulses turn into ghosts. This means that the waves incident on said interface undergo a shift in polarity and experience a near-perfect reflection back into the depths. The mathematical foundation for this phenomenon is described by the Zoeppritz equations, but can for vertically travelling waves be reduced to Eq. (2.12), where R is the reflection coefficient.

$$R = \frac{(\rho c_\infty)_{air} - (\rho c_\infty)_{water}}{(\rho c_\infty)_{air} + (\rho c_\infty)_{water}} \approx -1 \tag{2.12}$$

Equations taking into account focusing and defocusing due to wave curvature exist (see *Ayzenberg et al. (2009)* and *Landrø et al. (2016)*), but these effects are assumed to be incorporated by constricting the possible values of R slightly beyond -1 in the inversion process.

Figure 2.8 has been included below to give the reader a visual illustration of the signal decomposition hereto described looks in a shot record. In addition to the four main signal partitions, two other phenomena have been given a separate colour. These are the pre-shot record (muted already in the "raw" data), and what is thought to be an effect of causal filtering (also applied to the raw data): The apparent green drop in pressure is assumed to be a part of the primary signal which, through processing (causal filtering), has been delayed and suffered a change in polarity.

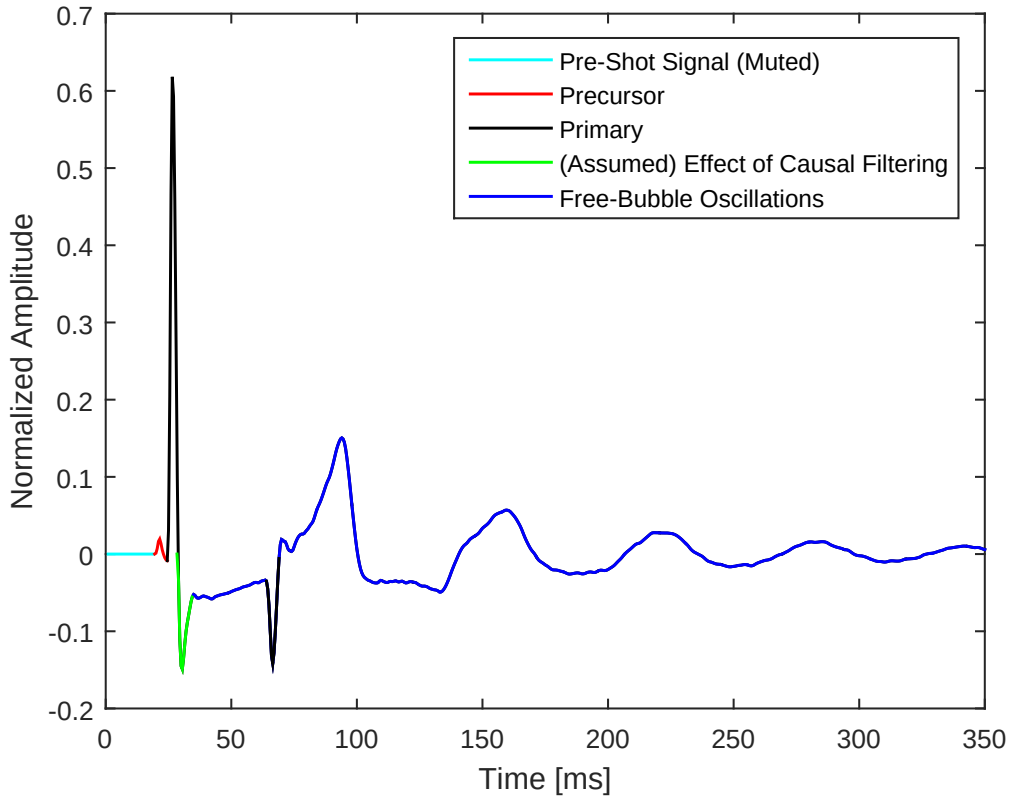

Figure 2.8: Shot signature nomenclature. The signal labelled has been frequency-filtered, and was recorded with the source at 30 metres depth. The second black peak is the ghost of the primary, and have thus been labelled in the same colour.

Chapter 3

Method

Bubble behaviour was modelled through solving Eq. (2.6) using an explicit Runge-Kutta solver (a slightly modified version of MATLAB's variable order method ode23) with adaptive time stepping. The solution vectors were later interpolated back to a regular time-stepping. Amongst other parameters, these vectors encompassed bubble radius and internal pressure. On a side note, the latter of these was scaled for the first 0.75 ms of the main bubble's modelling to extract a sensible primary-to-bubble ratio (not done for the micro-oscillations due to them losing relatively more energy at a faster rate). Passing the vectors through Eqs. (2.10) to (2.11), the dynamic pressure fluctuations generated by the bubble was found. The distance between the pressure emission source and measurement r either takes up values of 0.5 metres from the bubble wall (hypothesised precursor-separation), or 20 metres (gun-hydrophone-separation). As described in Section 1.2, no attempts were made at verifying the vertical alignment of air gun and hydrophone, leading to some uncertainty when modelling. Taking the intended separation of 20 metres to be exact, ghost arrivals that were recorded at unexpected times were numerically attributed to the source being located at slightly deeper or shallower depths than desired. Naturally, this depth is not constant, but decreases gradually as the bubble rises. Change in bubble-hydrophone distance has not been accounted for in the inverse-modelling. Actually including this characteristic would require multiple runs of the scheme (at minimum one to determine the bubble rise and another to implement it in the later behaviour), hence increasing modelling time. Changing depth does of course slightly change the bubble behaviour, so the implementation would at best be approximate. Without addressing this

issue, one would expect modelling to progressively diverge more and more from the measured signal. The inclusion of the β-term in Eq. (2.6) gives the inversion-scheme a way of correcting for it if necessary.

Summation of all incident waves (both direct ones and ghosts) on the modelled hydrophone was done in the frequency domain after passing them through a Fast Fourier Transform. The generated signal was subsequently inverse-transformed back to the time domain, and re-sampled to match the gathered dataset in both time-step and length.

By employing a system of MATLAB functions to perform all the operations hereto described, an inversion-scheme was put together: Synthetic signatures were generated through an initial run, with input parameter values picked by the Monte Carlo method. This run was then followed by subsequent ones, where the parameters were chosen by a genetic algorithm introducing small random mutations in the best fit model. If the resulting "offspring" had a lesser deviation from the measured signal than their progenitor - they replaced it before the next generation. An unfortunate trait of this method is the possibility of ending up in a local minimum. Thus, to increase confidence in the results the analysis was run multiple times for each depth. Development of the genetic algorithm had to be done from scratch, and proved to be a very time-consuming task.

Fidelity can largely be correlated with model complexity. The simplest model necessarily features a singular bubble. However, as seen in Figure 2.1, air guns do not strictly give rise to a single spherically pulsing bubble; rather, a profusion of smaller bubbles are formed by the actions of, or in addition to, the main one. Furthermore, the bubble might lose sphericity due to the presence of the gun. These effects cannot be accounted for in the modelling by Eq. (2.6) directly, but their combined effect can be approximated. Still, depending on the number of other such effects acting on the bubble, the approximation might be unable to cover all parts of the signal equally. When modelling a signature it is therefore exceedingly important to weigh its constituent parts according to their presumed importance. To exemplify this issue, without weighting component parts of the dataset desired recreated "S_{Raw}", the synthetic signal "$S_{Synthetic}$" converged upon by the inversion-scheme might neglect free-bubble oscillations in favour of adhering more closely to flat sections of the measured signal. As such, the weighting w needs to be tailored manually for each shot. The deviation "Γ" between each index of the signal was quantified using their Euclidean

distance, with lower values signifying a better match.

$$\Gamma = \sqrt{\sum_{i}^{N} \left(S_{Synthetic,i} - S_{Raw,i} \right)^2 \cdot w_i} \tag{3.1}$$

here, i represents one of N measurements in the time-domain. Anomalous sections of the measured signal (e.g. the green area of Figure 2.8) were given a zero-weighting.

Inverse-modelling the macro-behaviour of the signature (i.e. minimising Γ) serves two main purposes: For one, it is possible to infer the main bubble characteristics (internal pressure, radius and rise velocity) over time. Naturally, the fidelity of this inference increases with non-normalised data: Equation (2.6) has many degrees of freedom, and there are therefore many potential local minima of convergence when minimising the deviation. While the inversion-scheme was run multiple times, it is possible that the solution repeatedly converged to is an easily accessible local minimum - the global being hard to reach. With the actual pressure-readings available, rather than their normalised counterparts, some of the local minima could conceivably have been eliminated - and the parameters determined with more confidence. The secondary purpose of inverse-modelling is that it makes it possible to isolate the anomalous micro-behaviour. By subtracting the modelled signal from that which was measured, one is left with the parts of the signal which cannot be explained by the actions of the main bubble. As a side-note, this "differential" can also be found by repeatedly applying a smoothing filter to the original signal, and subtracting the result from it. However, through modelling one is sure to subtract *only* the effect of the main bubble.

The result of said subtraction, the differential, was attempted inverse-modelled in parts under two separate hypotheses - the first of which being that it was caused by the precursor bubble. Seeing as the precursor forms before the main bubble it experiences all of its pressure emissions, whose magnitudes therefore had to be modelled for the conjectured distance between the two. The resulting dynamic pressure was assumed to act uniformly on the precursor's surface, and incorporated in the inverse-modelling as outlined in Eq. (2.2). Modelling with the bubble spawn hypothesis is relatively simpler, as only low to negligible amounts of incident acoustic radiation can be expected. No bubble's surface-interaction with itself was modelled. In theory, some effects of said interaction could

have been modelled by slightly altering the iteration-scheme, splitting it into a pre- and post-ghost inversion where the latter used the dynamic pressure of the primer as an input. This would not, however, have modelled the more complex effects such as reentrant jets, seeing as Eq. (2.6) assumes a perfectly spherical bubble and the incident dynamic pressure is taken as uniform across the bubble wall. Modelling with this scheme could therefore not have determined whether the ghost indeed does cause the spawning of new bubbles. The end-goal when inverse-modelling the main bubble is to remove its influence on the dataset. Thus, given that the inversion-scheme operates faster without this alteration and still gives a satisfactory result, it does not need to be included when isolating the micro-oscillations (see Section 4.1). According to *de Graaf et al. (2014)*, the degree of surface interaction is proportional to the radius of the bubble and the distance to the surface. With both the precursor and bubble spawn hypotheses assuming the micro-oscillations to be caused by relatively small bubbles, surface interaction was assumed negligible for these cases.

Chapter 4

Results and Discussion

4.1 Inverse-Modelling Micro-Oscillations

As stated in Section 1.2, the amplitudes of the survey have been normalised. However, according to *Vaage et al. (2006)*, the magnitude of the primary is independent of air gun depth, and the amplitudes seen in unprocessed plots can be assumed to be approximately comparable. Reviving the approximation that bubbles operate much like mass-spring systems, increasing the depth can be likened to installing a stiffer spring: Less energy is lost per oscillation, but due to the oscillation frequency increasing, more energy is lost over time. Effectively, this means that the amplitudes of the main bubble's initial (low-frequency) free-bubble oscillations are expected to be greater for deeper shots. For slightly longer time spaces the micro-oscillations should conversely drop in amplitude and peter out faster at depth as their already high oscillatory frequency increases further. Both these expected phenomena are in fact observed in Figures 4.1 to 4.4. Note here also the micro-oscillation revitalisation after every large free-bubble oscillation.

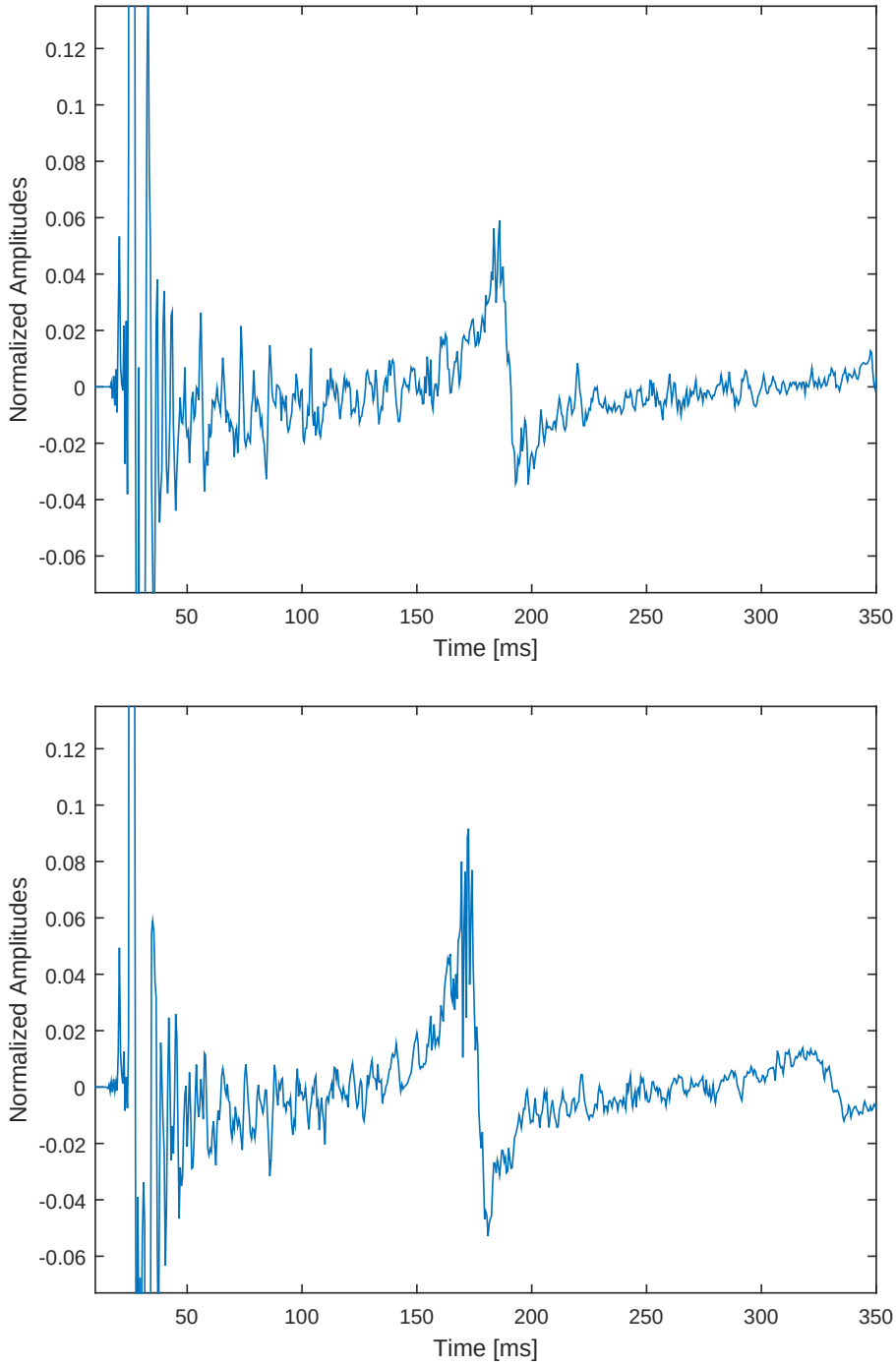

Figure 4.1: Zoomed plot of unprocessed direct wave signatures generated with the source at 3 and 5 metres depth. The same scales have been used in Figures 4.2 to 4.4 to ease comparison.

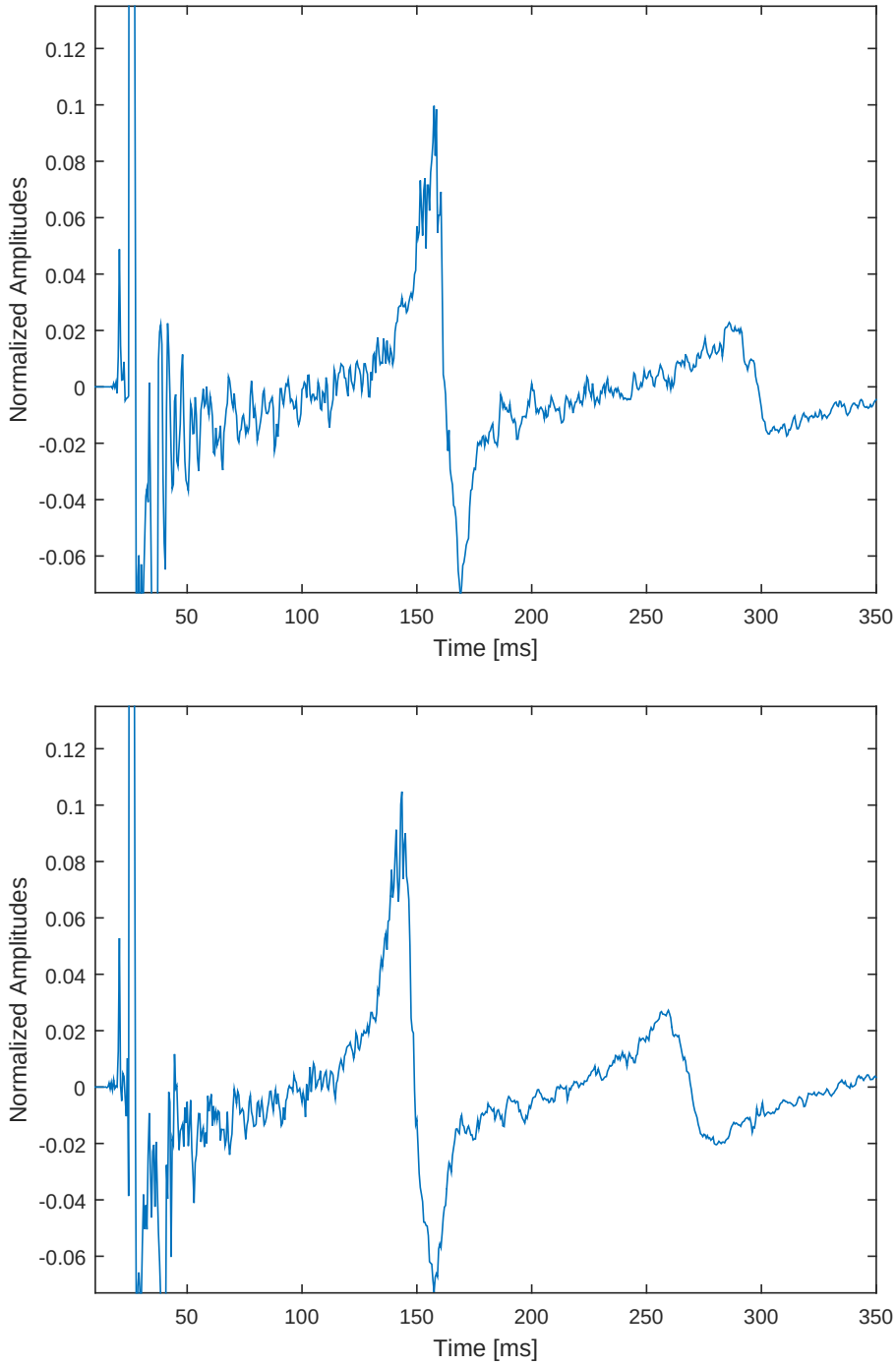

Figure 4.2: Zoomed plot of unprocessed direct wave signatures generated with the source at 7.5 and 10 metres depth. An anomalous spike in the 7.5 metre source depth dataset has been damped.

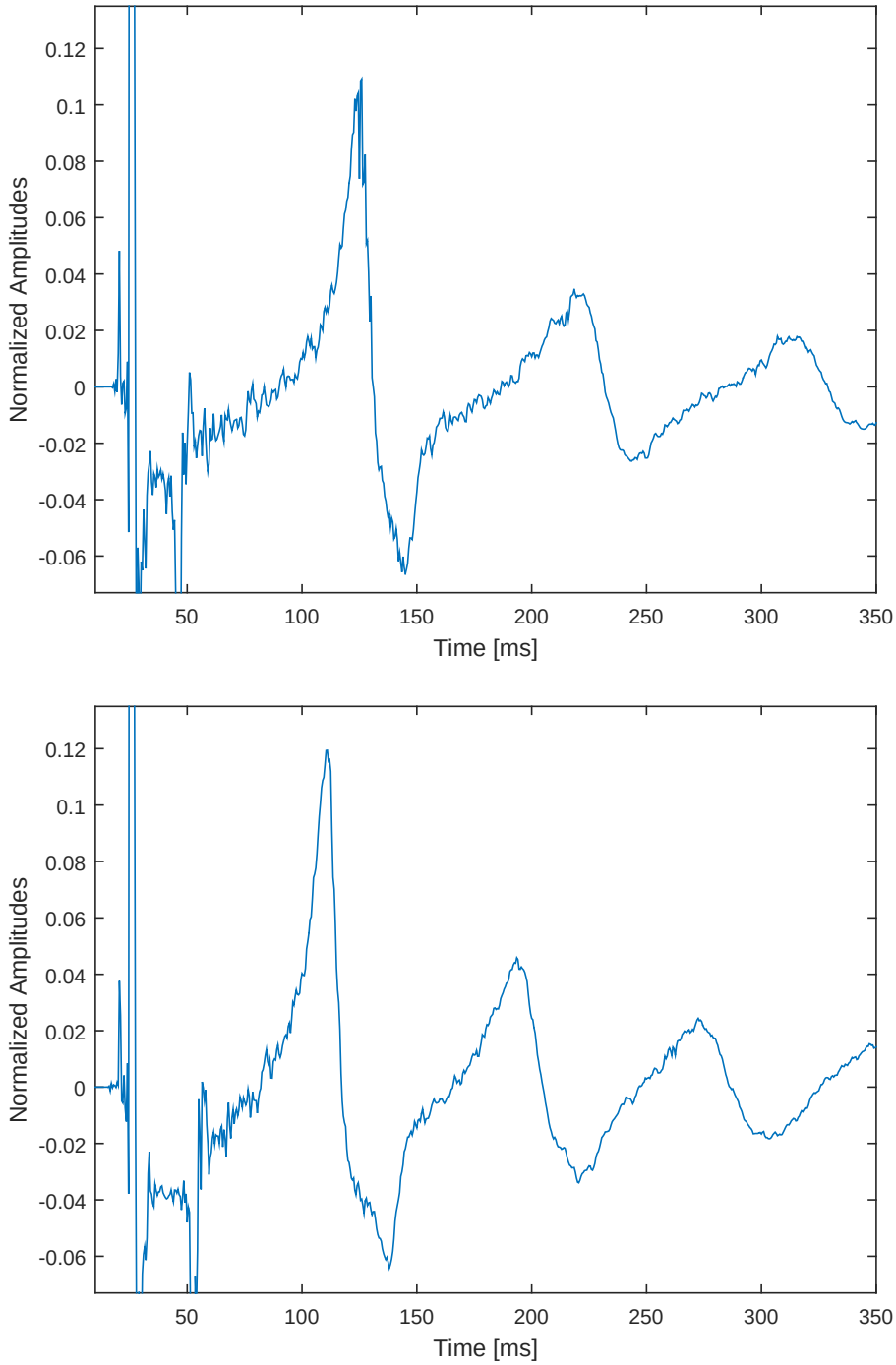

Figure 4.3: Zoomed plot of unprocessed direct wave signatures generated with the source at 15 and 20 metres depth. An anomalous spike in the 15 metre source depth dataset has been damped.

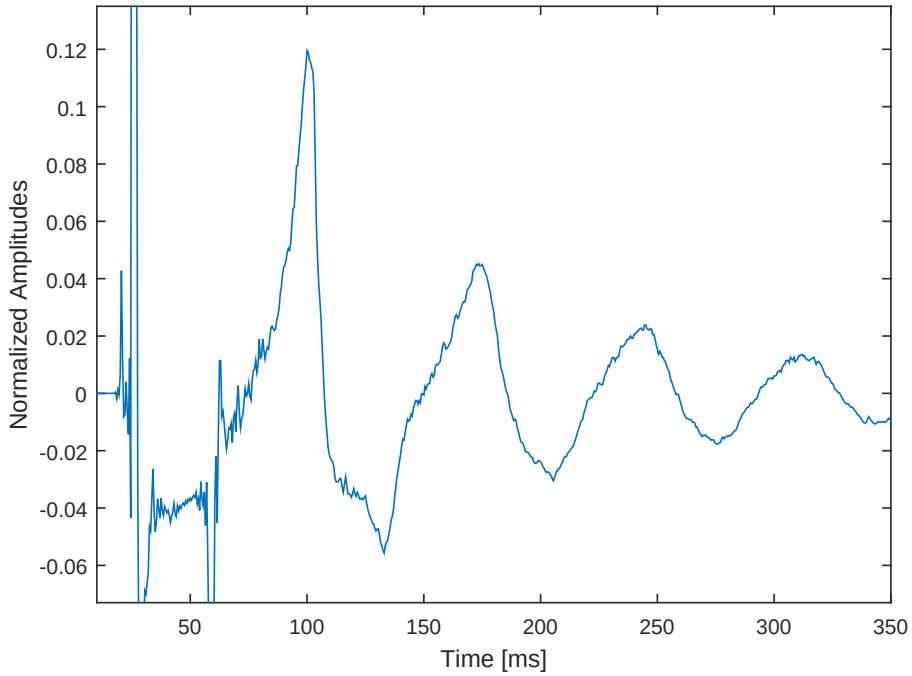

Figure 4.4: Zoomed plot of unprocessed direct wave signature generated with the source at 25 metres depth. Beyond 25 metres the micro-oscillations become barely discernible.

When performing an analysis such as that presented in this thesis, it is desirable for the initial signal-to-noise ratio to be as high as possible. Seeing as decreasing the depth causes the average micro-oscillation amplitudes to increase, the datasets used in the analysis has predominantly been the ones gathered with the source close to the surface. A minimalist style has been chosen in presenting the report findings, meaning that the bulk of them are illustrated using only the 3 metre source depth datasets. Still, the same analysis was also performed on the 5 metre datasets to verify the results. Plots generated in this latter analysis are found in the appendix, but some have also been included in this chapter to communicate particular points to the reader.

The observed trend of smaller micro-oscillations with depth lends some credence to the precursor/bubble spawn hypotheses - lower hydrostatic pressure allowing for more sustained oscillations. It could, however, also be an indirect effect of reduced hydrostatic pressure on the main bubble: When it expands, volume around the air gun previously occupied by water is suddenly occupied by (relatively) low-pressure air. This might create a pull on the gun, which could cause movement and mechanical noise, the effect being greater with a lower external pressure to work against. Conversely, the gun could also be rattled by the acoustic emissions of the main bubble. Whatever the causal mechanism,

any induced gun movement will inevitably also affect the hydrophone (see the instrument setup of Figure 1.2). Thus, the micro-oscillations could possibly be the result of minute hydrophone movements. Conversely, the acoustic emission of the bubble could rattle the air gun and therefore cause mechanical noise. Testing of such gun-related hypotheses would, however, require experimental studies themselves. As the equipment was unavailable at the time of writing this thesis, these possibilities were left for future studies.

4.1.1 Isolation

In order to investigate the micro-oscillations more thoroughly, it is first necessary to isolate them. As previously outlined, the chosen method for doing so was to inverse-model the behaviour of the main bubble, and subtract its influence from the dataset. The measured signature and its inverse-modelled counterpart are displayed together in Figure 4.5.

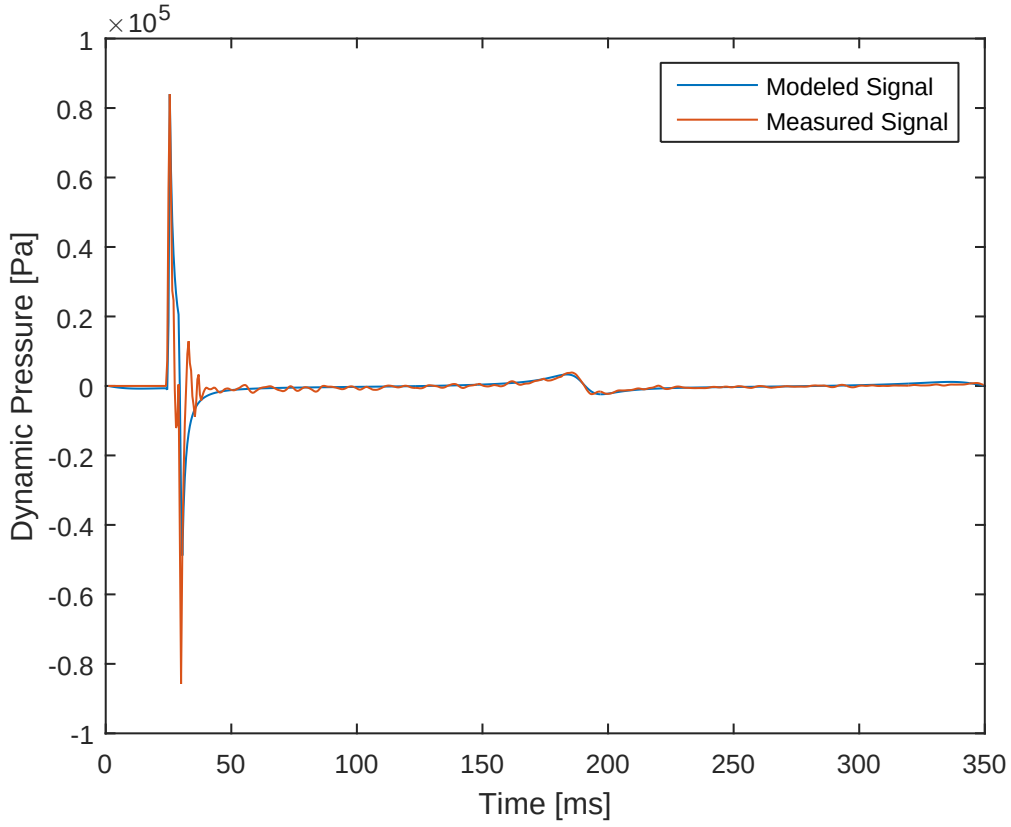

Figure 4.5: Measured- and inverse-modelled signatures overlain each other for a shot fired at 3 metres depth. Magnitudes displayed in the plot are the ones found through inverse-modelling, and cannot be verified due to the normalisation of the measured dataset. They do, however, fall close to those converged upon when inverse-modelling the 5 metre dataset (see Figure A.1 in the appendix). The signal labelled "measured" has undergone a lowpass for illustrative purposes.

It should be noted that for 3 metre source depths the ghost coincides with the energy shifting of the causal filter, yielding an anomalously strong apparent ghost. The source is also sufficiently close to the surface (i.e. the ghost is strong enough) for the causal filter to shift and invert its energy to (at least) a second spike. The parameter values used to model the signal in Figure 4.5 have been summarised in Table 4.1. Here p_0 and V_0 are the bubble's initial internal pressure and volume.

Table 4.1: Parameters used to model the 3 metre source depth main bubble signal in Figure 4.5. The values of this, and all following tables have been rounded to the third decimal point.

R	Ψ	α	β	β_2	p_0	V_0
[ø]	[ø]	[m^2/s^2]	[m^4/s^4]	[m^4/s^5]	[Pa]	[in^3]
-1.278	7.380	0.336	0.017	0	139 $\times 10^5$	578

Subtracting the modelled signal from the measured yields the "differential" (the isolated micro-oscillations). Figure 4.6 illustrates differentials from the three datasets at this depth, and showcases the micro-oscillation repeatability. The causal filter creates some uncertainty as to where in Figure 4.5 filter-effects end, and oscillations begin. When inverse-modelling the micro-oscillations using the scheme developed, it is very important to avoid the primer. Consequently, a conservative starting estimate was made, and only the weighted parts of the differential have been included in Figure 4.6. All "flat" sections can hence be thought of as areas with no constraint on bubble behaviour in later modelling.

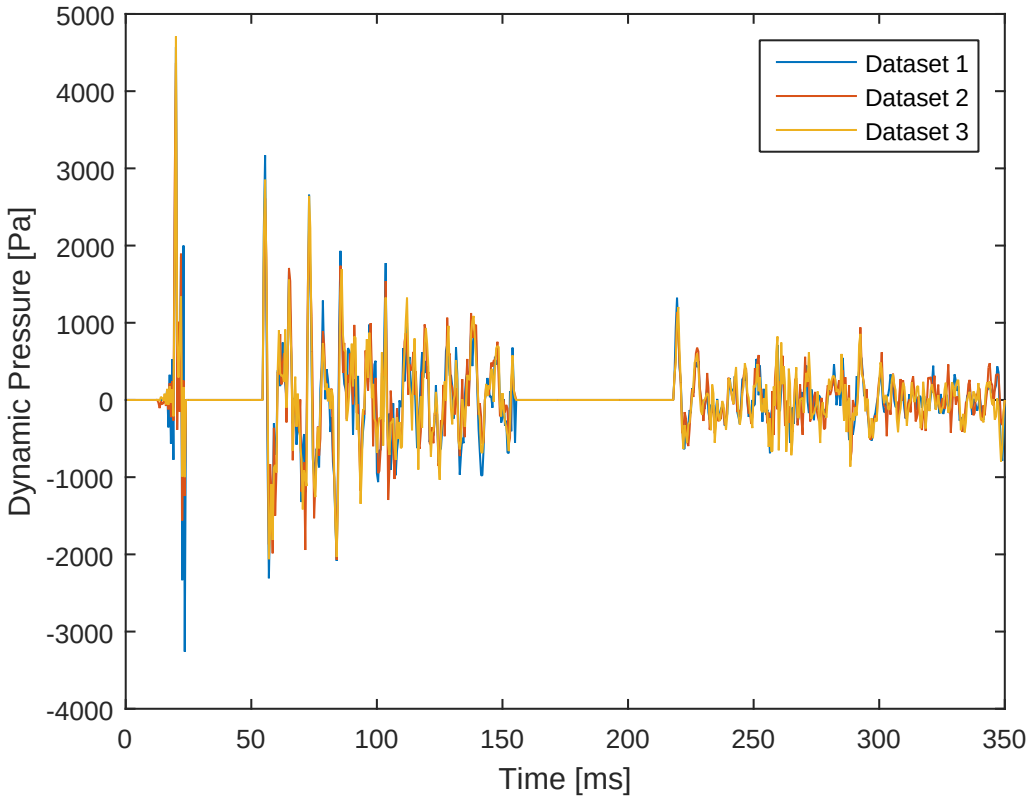

Figure 4.6: Results of subtracting the modelled behaviour of the main bubble from the dataset. From left to right: Precursor, pre-collapse micro-oscillations, and post-collapse micro-oscillations. The differentials have been zeroed for times where the margin of error is the greatest (around the main bubble pressure peaks and where filter effects are assumed to skew the results).

4.1.2 Frequency and Noise

As outlined in Chapter 2, separating data from noise is of prime importance in processing. This subsection has therefore been included early to dispel any notion of the micro-oscillations being caused by incident noise from a source external to the experiment, and to quantify the actual influence of such noise on the dataset. A strong argument for the oscillations being shot-related is the observed repeatability: If originating from a non-shot related source, such a close match in magnitude and time across surveys is highly unlikely. Furthermore, if approximating the energy distribution over time, as has been done for the differential in Figure 4.7 one finds that the energy of the micro-oscillations gradually diminishes to the noise level.

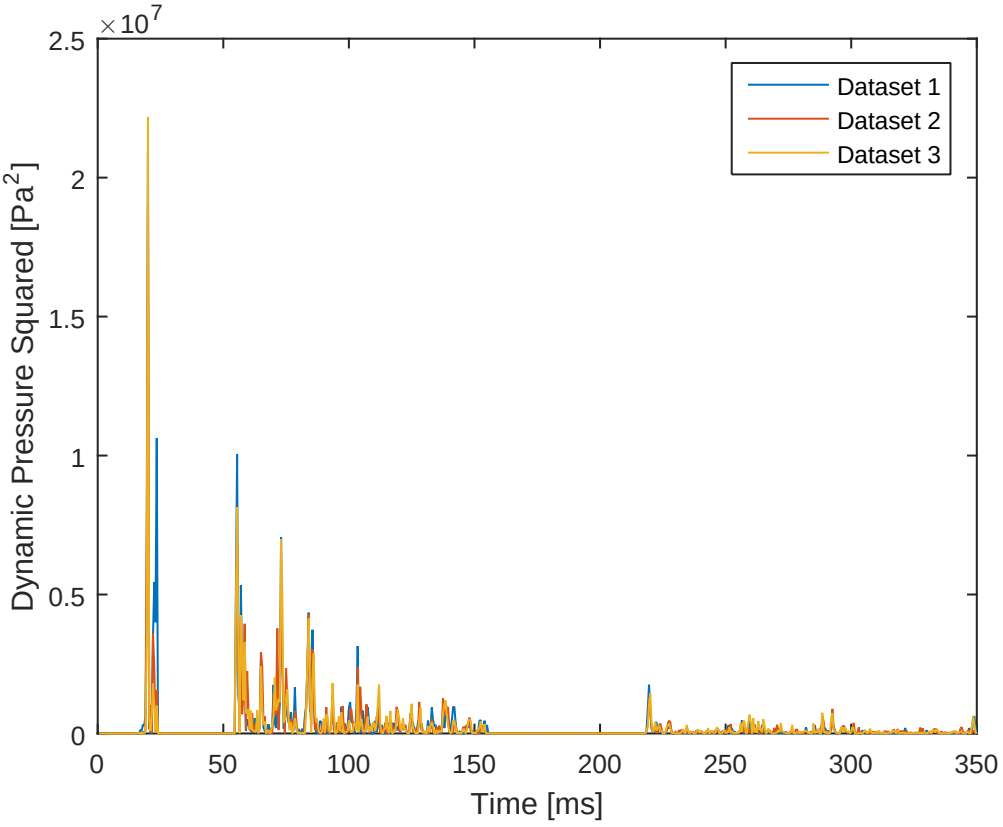

Figure 4.7: The 3 metre source depth differential squared, illustrating energy drop-off to the noise level.

The same point can be made by contrasting the power spectrum of the differential (Figure 4.9) against an equal length power spectrum of the ambient noise. As previously stated the pre-shot data has been removed, and there is hence no unbiased registry of the noise in the area. However, a good "noise estimate" can be made using the measurements at the end of the recording window (Figure 4.8). Notice in particular that the highest peak of Figure 4.8 is several orders of magnitude smaller than that of Figure 4.9, and consists of low-frequency swell noise. Hence, ambient noise is considered to have a negligible influence on the micro-oscillations. A more in-depth analysis of the post-shot noise will be done in Section 4.2

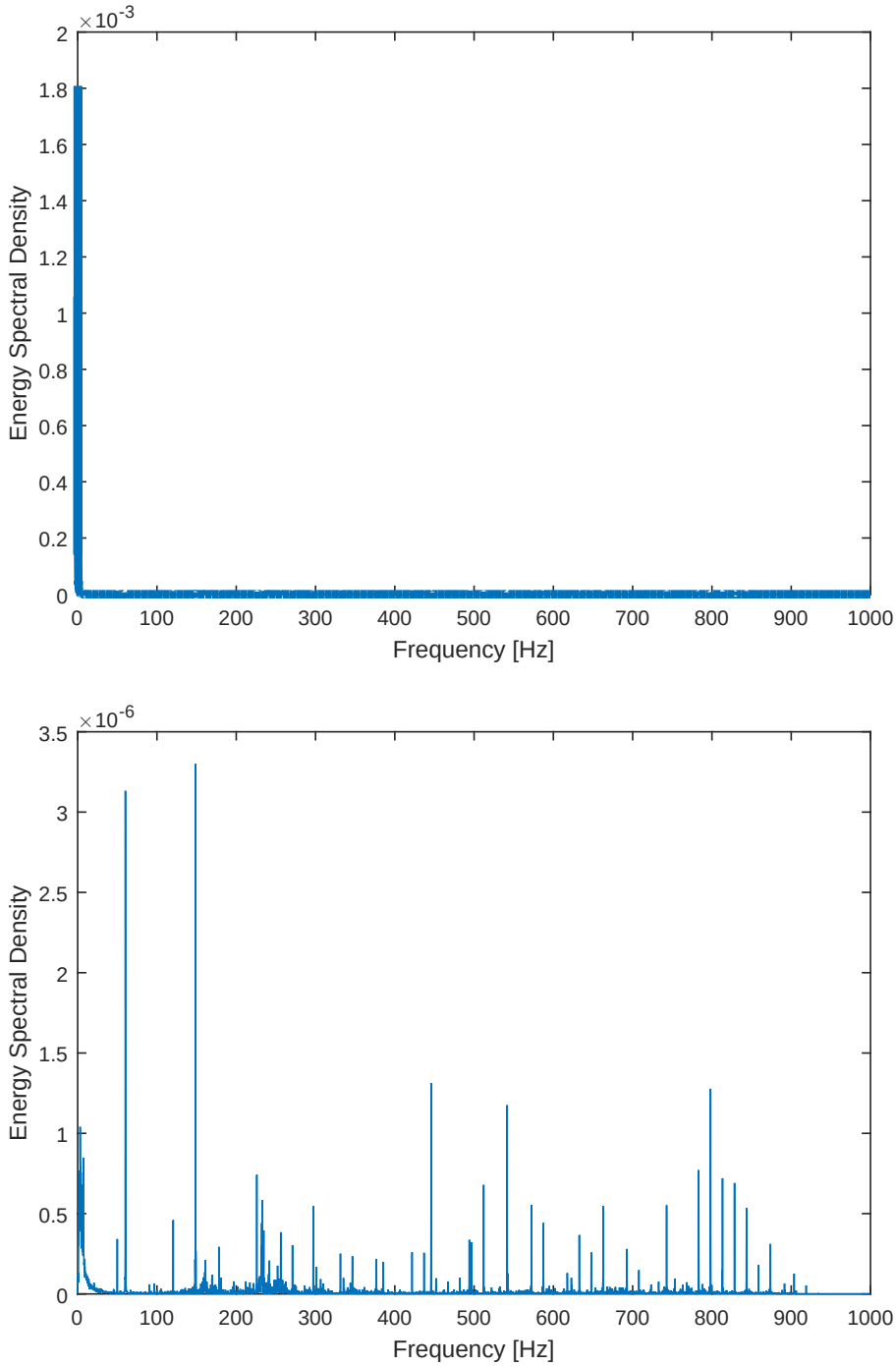

Figure 4.8: Average energy distribution over frequency for post-shot noise between the three 3 metre source depth datasets. The line in the topmost graph has been made thicker to increase discernibility. A highpass filter have been applied to yield the graph below it.

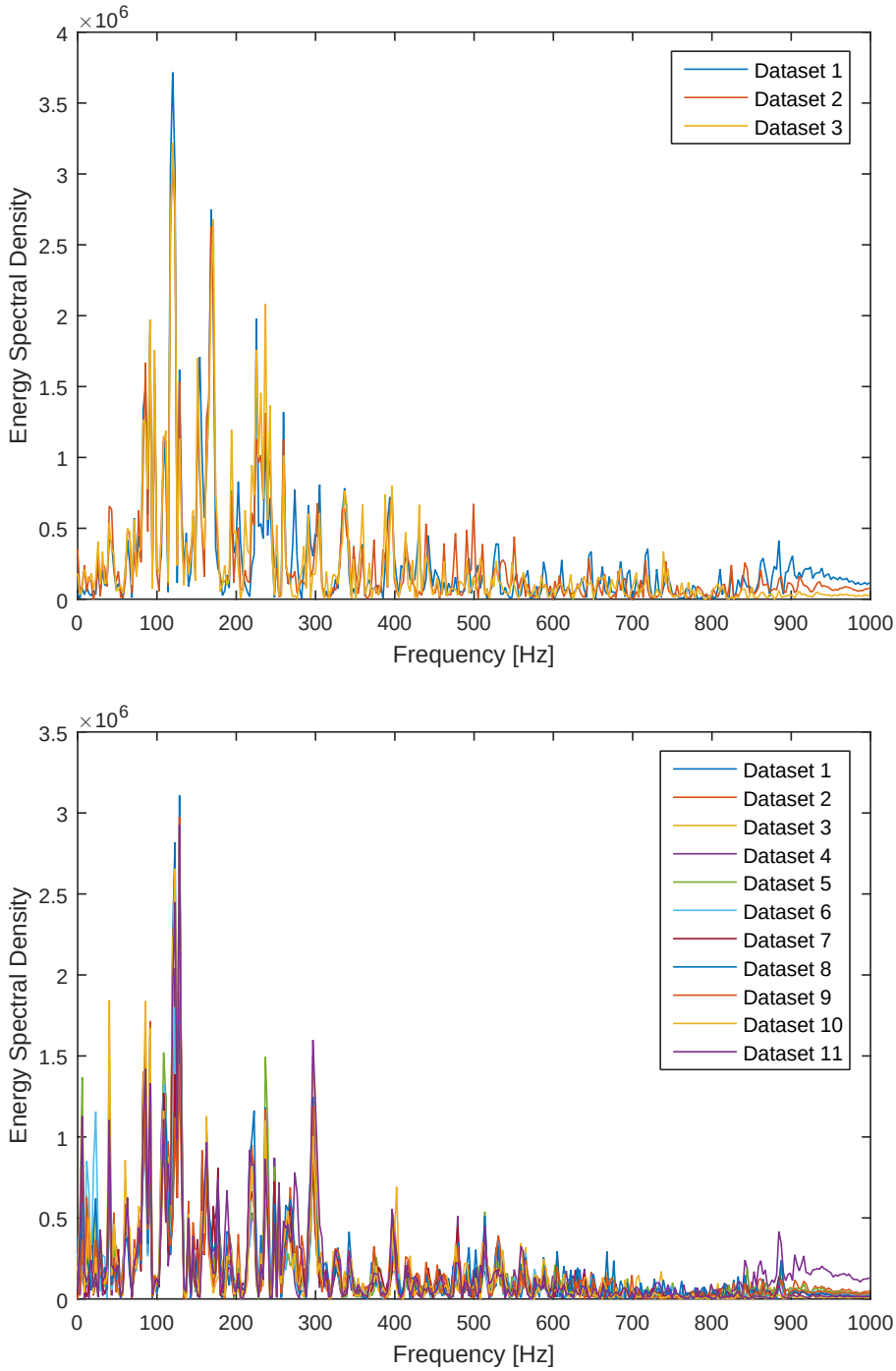

Figure 4.9: Energy spectral density of the differentials for the 3 and 5 metre source depths respectively.

The spectral densities of the 5 metre source depth differentials have been included from Appendix A to illustrate that, besides the introduction of some low-frequency noise, there is a general shift to higher frequencies and lower energies with depth. As earlier stated, this is to be expected if the micro-oscillations were caused by the pressure emissions from small bubbles.

4.1.3 Cleaning of Data

Despite the high repeatability of Figure 4.6, the signals do on first sight appear quite messy. This might be for a number of reasons. For one, bubbles of varying sizes and pressures (and thus with distinct oscillation periods) may be formed. Gun-related noise (solenoid clicking, mechanical contact between moving parts, etc.) may also in places partly obscure the data.

To simplify the inversion, the dominant frequencies of the datasets were thus identified from Figure 4.9. As is to be expected, the frequency spectra of the three datasets also showcase their repeatability. The dominant range was determined to be between 75 and 180 Hz. A Butterworth filter using these limit values was hence applied to the dataset, resulting in Figure 4.10. This same process was also done exclusively on the main peak (115-125 Hz) with a nearly identical resulting curve. The end-goal of this investigation is to examine the feasibility of small oscillating bubbles being able to generate the signal, not finding the actual parameters of the bubbles doing so in this exact experiment. For this reason the frequency range chosen is largely arbitrary as long as it covers a representative segment. The peak between 200 and 300 Hz for the 3 metre source depth dataset appears isolated from the others, and was kept out of the analysis on the assumption of it being created by bubbles of yet smaller sizes than the others.

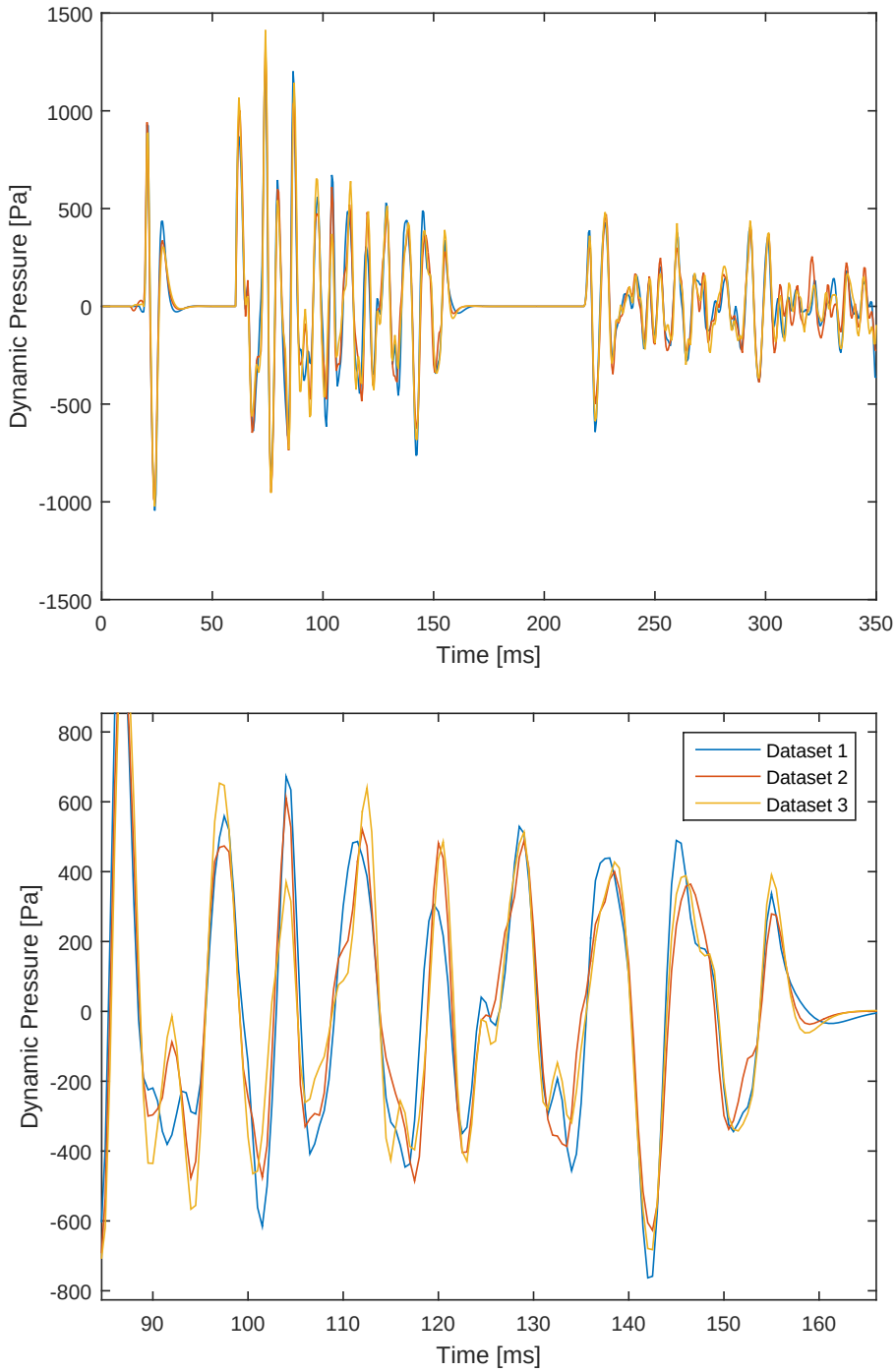

Figure 4.10: Figure 4.6 after application of a bandpass filter. The lower plot is a zoom of the upper, illustrating signal skipping in detail.

While the previous operations have cleaned up the data somewhat, there are still incongruities at the micro-level, primarily in the form of signal skipping (energy occasionally recorded at one time-index separation). This is partly remedied through stacking, which also suppresses the already limited amount of noise in the data. It should here be noted that the first peak of the pre-collapse micro-oscillations is lower than some of the succeed-

ing ones. This is not the case for Figure 4.6, and is an effect of the frequency-filtering applied. Less weighting has hence been given to this peak than the following ones.

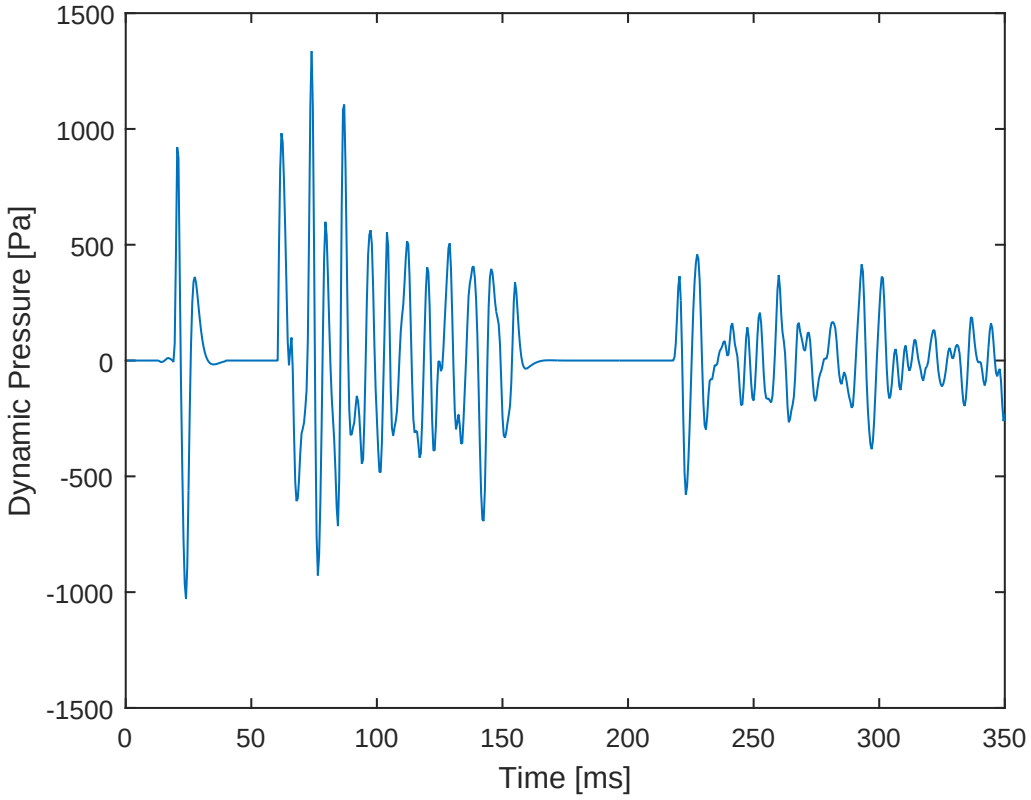

Figure 4.11: Result of stacking the bandpassed differentials.

4.1.4 The Precursor Hypothesis

Inverse-modelling the micro-oscillations under the assumption that they were created by the precursor requires accounting for the pressure pulses emitted by the main bubble. When modelling it, there is as previously stated controversy on whether or not to include Eq. (2.11). Whereas the farfield-term is overpowering at a distance of 20 metres (source-hydrophone distance), the nearfield-term's contribution is relatively greater at distances where the precursor could conceivably exist. Neglecting or including Eq. (2.11) when modelling hence has a small but notable impact on the precursor's behaviour. The absolute pressure the precursor might experience at a distance of 0.5 metres from the main bubble wall has for these two cases been illustrated in Figure 4.12.

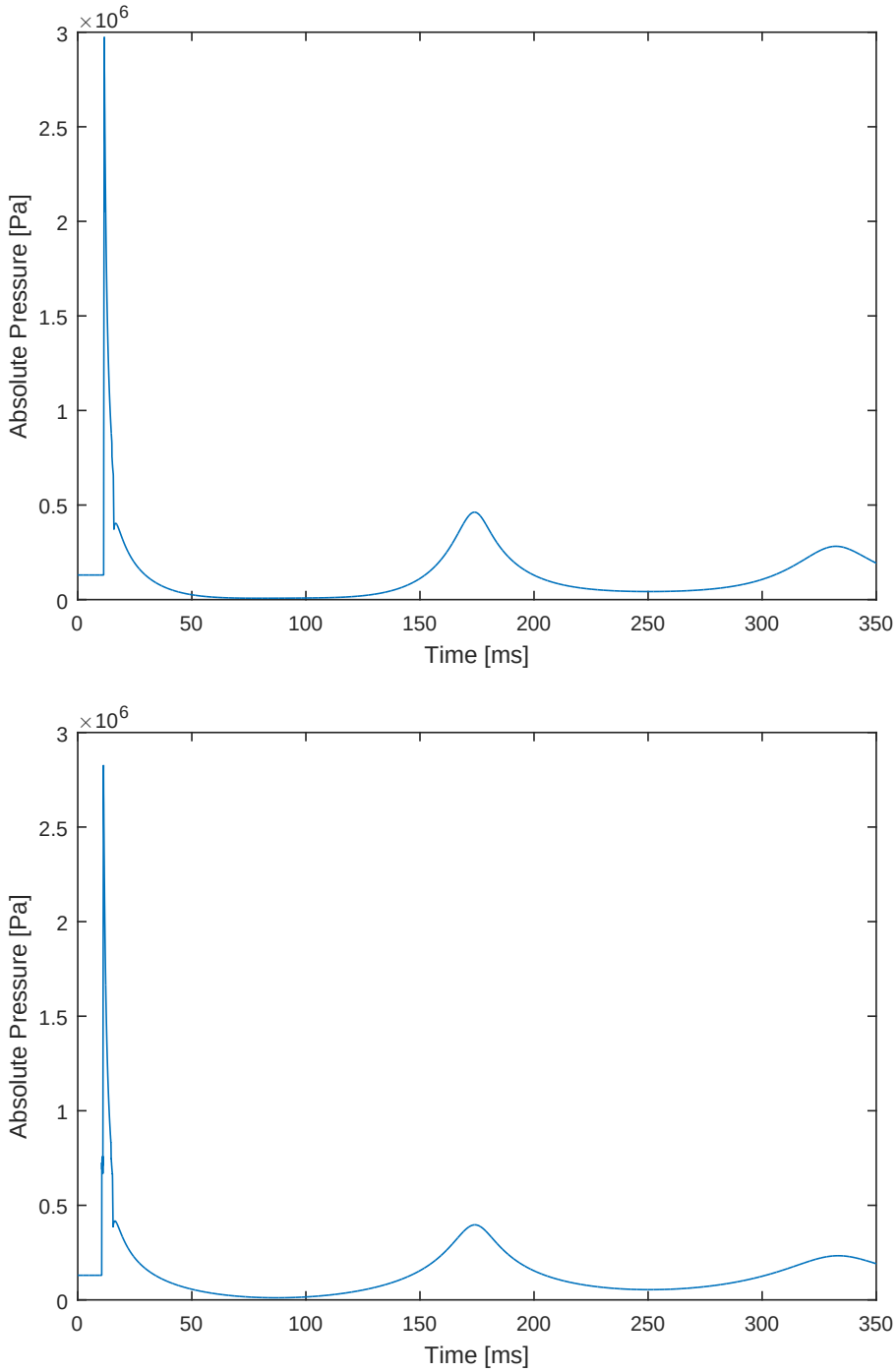

Figure 4.12: Modelled absolute pressure at a distance of 0.5 metres from the main bubble's wall when including the nearfield-term (top) and when excluding it (bottom). The primary dwarfs the ghost this close to the source due to geometric spreading and attenuation.

Besides the slightly stronger pressure pulses when including the afterflow-term, the general behaviour of the two pressure-fluctuation graphs are the same. As such, one would expect their overall effect on the bubble behaviour to be more or less equal. This is indeed what is observed in Figure 4.13, only that the effect is intensified upon the term's

inclusion. For both scenarios, the precursor loses its identity, and begins to oscillate with a period approximately equal to that of the main bubble. This was invariably the case for all modelled bubbles who matched the precursor's initial, undisturbed - behaviour. Consequently, the precursor hypothesis should most likely be discarded. On account of strong evidence that the precursor hypothesis is invalid, this analysis was not redone for the 5 metre dataset.

The same parameters used to model both precursor signatures in Figure 4.13 to illustrate the effect of including the afterflow-term. These are listed in Table 4.2 below for readers wanting to reproduce the results.

Table 4.2: Parameters used to model both the precursor's behaviour at 3 and 5 metres depth when exposed to the acoustic emissions of the main bubble.

R	Ψ	α	β	β_2	p_0	V_0
[ø]	[ø]	[m^2/s^2]a	[m^4/s^4]	[m^4/s^5]	[Pa]	[in^3]
-1.701	2.672	-0.227	-0.034	0.077	9.540×10^5	0.048

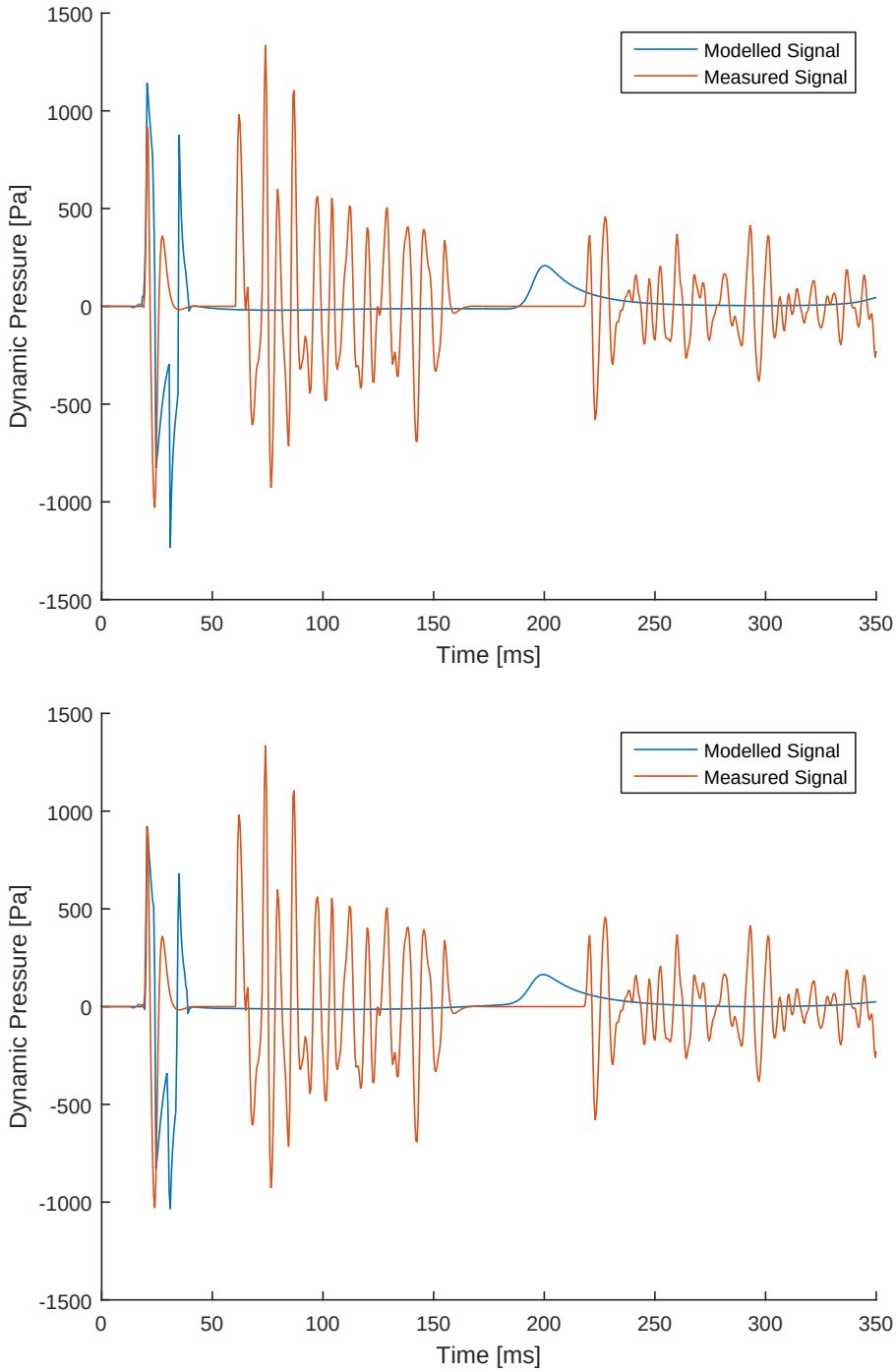

Figure 4.13: Results of inverse-modelling the micro-oscillations under the precursor hypothesis when including the nearfield-term (top) and when excluding it (bottom). All bubble behaviour after its first oscillation passing of the precursor's ghost has been dictated by the radiation incident upon it. The distance between the precursor and the main bubble wall was taken to be 0.5 metres at all times.

4.1.5 The Bubble Spawn Hypothesis

The bubble spawn hypothesis put forth in Section 2.1 states that the main bubble spawns a number of smaller bubbles which then oscillate separately between its free-bubble oscillations. As they are not exposed to the peaks of acoustic radiation emitted by the main bubble, they are able to preserve their identity, and oscillate close to their natural frequency. A few suggestions were also made as to the potential causal mechanisms for their generation, one being turbulence upon main bubble expansion. This cannot be tested using the numerical software available, and some studies done on bubble oscillation describe the first oscillation as "relatively smooth" (see *(Langhammer et al., 1995)*). Previous research is rather more supportive of the second suggested mechanism - interaction with the free-surface. If this is actually the method by which these smaller bubbles are generated, one would not expect to register them before the ghost. Seeing as the ghost arrives almost immediately after the primary for the shallow bubbles, it is necessary to go deeper to see if this is the case. The first depth at which the ghost became sufficiently delayed to distinctly observe the post-primary, pre-ghost data was at 25 metres. A zoom of the relevant interval in Figure 4.4 has hence been included.

As can be discerned, Figure 4.14 gives supporting evidence for surface-interaction being the generating mechanism: If the oscillations occurring post-ghost had all been an effect of causal filtering one would expect them to die out at the same rate as the oscillations earlier in the figure.

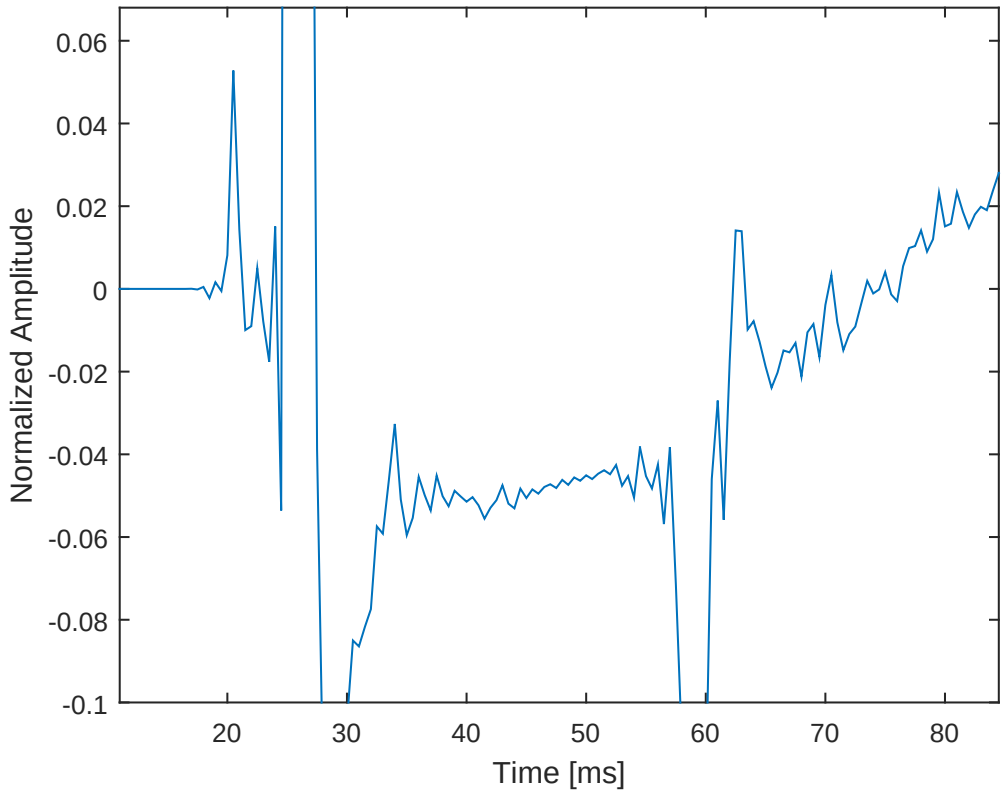

Figure 4.14: Zoom of the signal shown in Figure 4.4, i.e. the signal generated with the source at 25 metres depth. Displayed here are the precursor, the primary, large and smaller filtering effects, the ghost and micro-oscillations.

It should also be mentioned that while the causal mechanism for the micro-oscillations may be interaction with the down-going ghost, they need not be created through the spawning of new bubbles. Conceivably, the ghost might also cause the main bubble to deform from its spherical shape, this way causing a second oscillation in form super-positioned on the slower oscillation of volume. For this hypothesis to be tested shape deformation has to be accounted for, and it is hence left for future investigations.

The effect of the ghost on the main bubble is dependent on the depth of the source. This aspect of bubble dynamics has been investigated experimentally on numerous occasions, including by *Chahine (1982)*, who found the limiting distance of interaction to be 3.33 bubble (maximum) radii. Nevertheless, Chahine did work with spark-generated bubbles having a maximum radius of only 1 cm. Figure 4.14 seems to suggest that for larger, air gun-generated bubbles this distance is likely to be higher.

Pre-Collapse Micro-Oscillations

Regardless of whether these smaller bubbles are spawned by ghost or by other phenomena, one does get a decent result when inverse-modelling the signal in Figure 4.11 under the assumption that it was generated by a small, freely oscillating bubble.

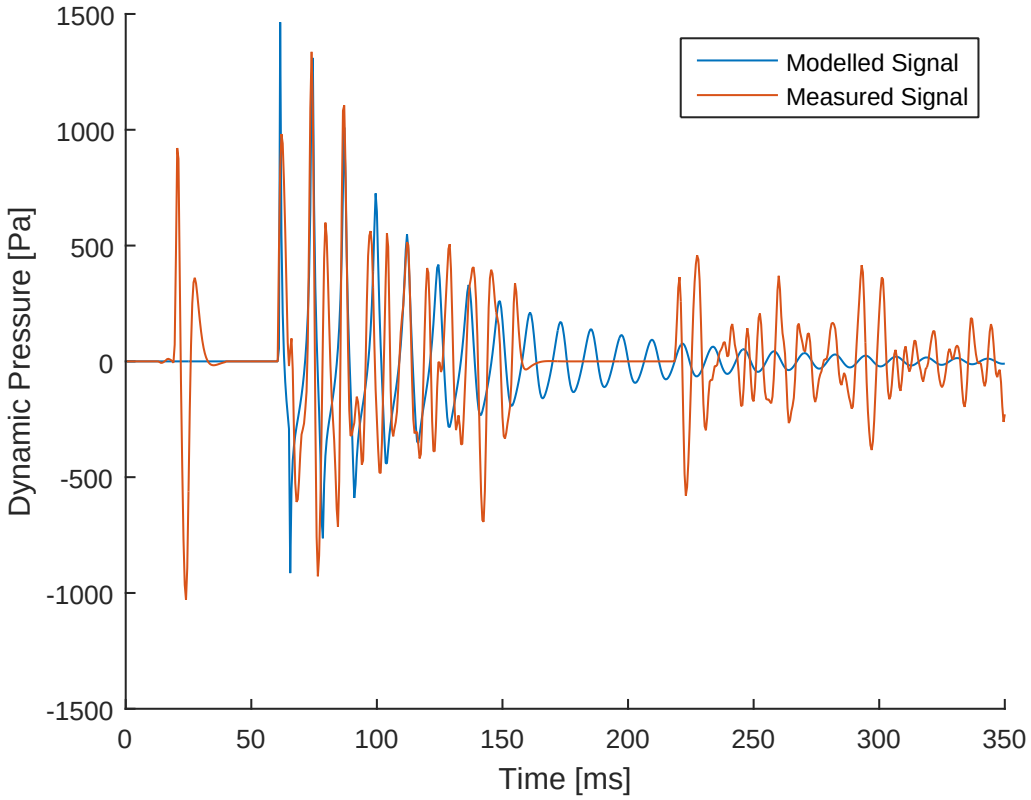

Figure 4.15: Result of inverse-modelling the 3 metre source depth pre-collapse micro-oscillations under the bubble-spawn hypothesis. The second grouping of micro-oscillations is modelled separately due to it being formed after the first collapse of the main bubble.

Figure 4.15 shows a close match in both amplitude and bubble period between the modelled and measured micro-oscillations. One can, however, expect more than one bubble to be formed, and likely bubbles of varying sizes. Variation in size would further cause a difference in period, which could hypothetically account for the peaks skipped by the inversion. Furthermore, the generated bubbles could due to their close proximity charge each other, causing variable damping. Besides bubble-bubble interaction this inverse-modelling has, like the ones before it, not accounted for change in bubble-hydrophone distance due to bubble rise. While the inversion-scheme was unable to reproduce an exact result, it does show the feasibility of a (system of) bubble(s) generating the micro-

oscillations. As earlier stated the bubble spawn hypothesis has also been investigated for the 5 metre source depth datasets, with the end result as displayed in Figure 4.16.

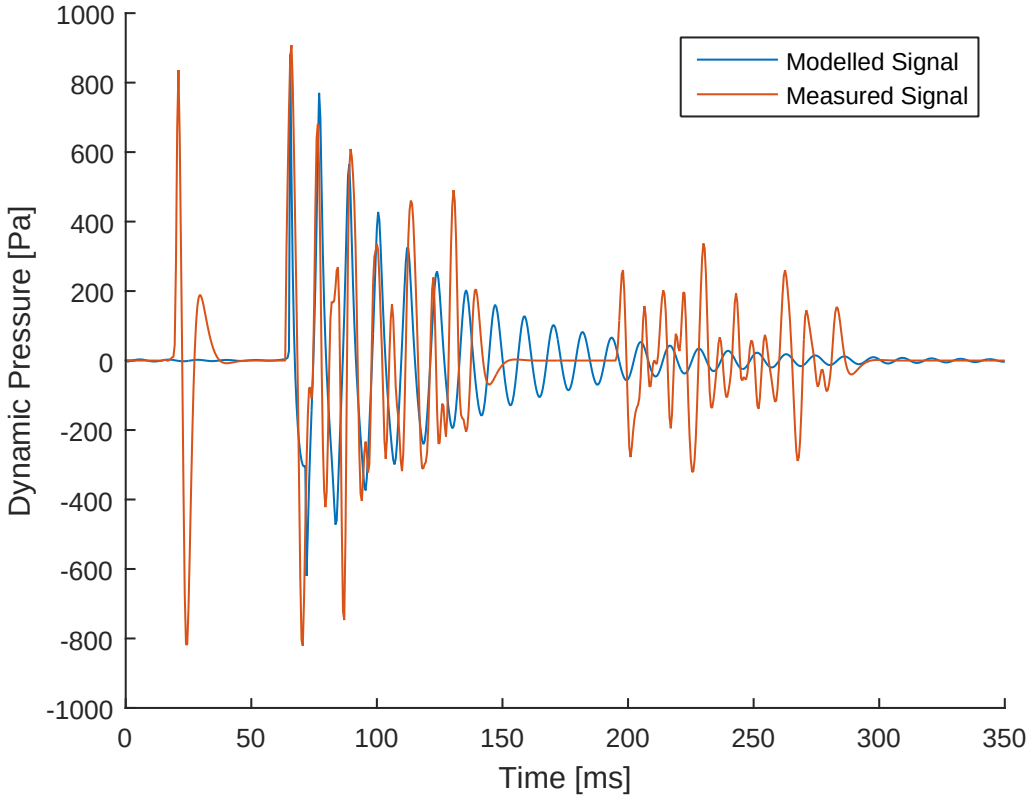

Figure 4.16: Result of inverse-modelling the 5 metre source depth pre-collapse micro-oscillations under the bubble-spawn hypothesis.

Like the inverse-modelling of the 3 metre datasets, inverse-modelling at this source depth did not provide a one-to-one match. However, the low deviation achieved does grant additional support to the feasibility of a system of bubbles doing so.

While the exact parameter values used to reproduce the micro-oscillations are considered of lesser importance than their ability to generate it, they have been included in Table 4.3 for readers wanting to reproduce the results. It should also be noted that the inverse-modelling, starting from a Monte Carlo approach, converged to relatively close values for both datasets. This is an additional point in favour of the hypothesis, as altering the source depth does not cause a drastic shift in bubble parameters.

Table 4.3: Parameters used to model the pre-collapse micro-oscillations in Figure 4.15 (3 metre source depth) and 4.16 (5 metre) respectively.

R	Ψ	α	β	β_2	p_0	V_0
[ø]	[ø]	[m^2/s^2]a	[m^4/s^4]	[m^4/s^5]	[Pa]	[in^3]
-0.544	0.235	1.65	-0.034	0	6.830×10^5	3.949
-0.515	0.220	1.928	-0.001	0	2.750×10^5	10.964

By plotting the energy spectral density of the inverse-modelled bubbles together, they can also be seen to adhere to the expected trend of lower energies and shorter periods with depth.

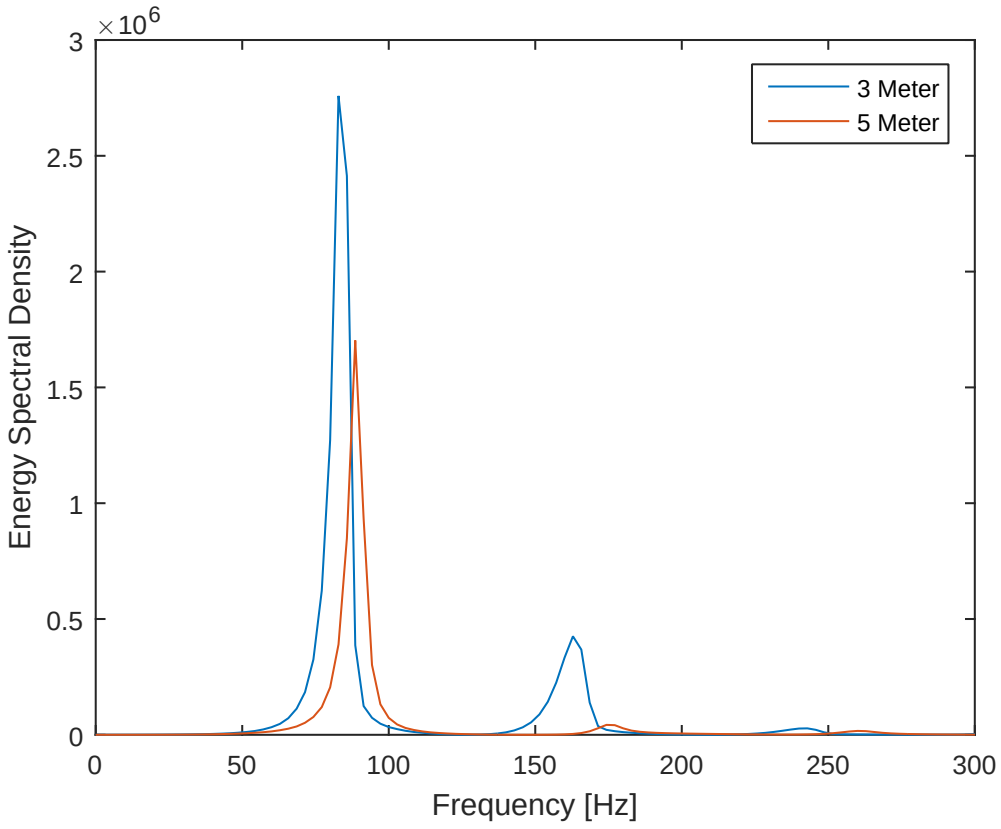

Figure 4.17: Energy distribution over frequency for the inverse-modelled micro-oscillations of Figures 4.15 and 4.16. Smaller peaks are harmonics of the greater ones.

Post-Collapse Micro-Oscillations

Having achieved a good match for the first grouping of micro-oscillations, those seen after the first collapse were inverse-modelled under the same conditions, with the results seen

in Figure 4.18.

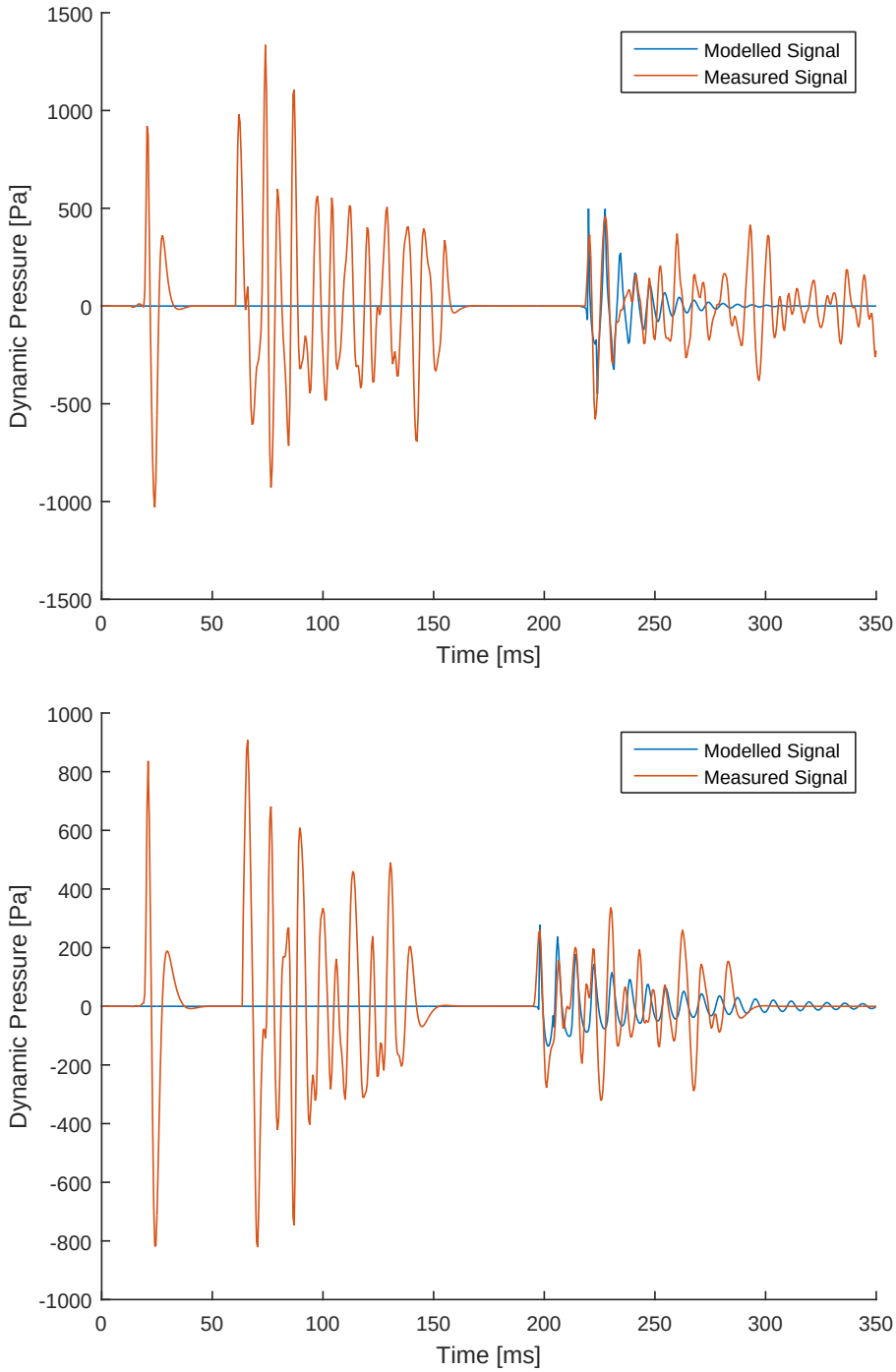

Figure 4.18: Result of inverse-modelling the post-collapse micro-oscillations under the bubble-spawn hypothesis for the 3 and 5 metre source depths respectively.

Compared to Figures 4.15 and 4.16, Figure 4.18 displays a relatively poor convergence between the modelled and measured signals. As mentioned in Section 2.1.2, this might be due to the complexity of the post-collapse micro-oscillations being greater than that

of earlier ones: Regardless of the mechanism generating these preceding oscillations, the same mechanism can be assumed to act in conjunction with additional (collapse-related) turbulent processes to form the post-collapse micro-oscillations (see Figures 2.1 and 2.4). Said turbulent process also seems to be more prevalent at 3 metres depth than at 5, which makes sense considering there is less hydrostatic pressure to work against. Whatever the reason, this increase complexity could not accurately be reproduced by the actions of one singular bubble: Adherence to the earlier parts of the signal often come at the expense of divergence from the latter. Thus, to model an accurate reproduction it would be necessary to include more bubbles with varying volumes and pressures. These would then mutually influence each other to a non-negligible degree - an interaction which for fidelity would need to be implemented along with a hypothesised distance between them. Said task was left for future works due to complexity and deadline concerns. The parameters used to generate the best-fit model of this later grouping is found in Table 4.4.

Table 4.4: Parameters used to model the 3 and 5 metre source depth post-collapse micro-oscillations in Figure 4.18.

R	Ψ	α	β	β_2	p_0	V_0
[ø]	[ø]	[m^2/s^2]	[m^4/s^4]	[m^4/s^5]	[Pa]	[in^3]
-0.648	8.508	0.200	-0.358	0	9.872 $\times 10^5$	0.446
-0.505	2.372	0.385	-0.061	0	1.179 $\times 10^5$	5.455

The modelled post-collapse micro-oscillations at 3 metre source depth display a very low fidelity, and the power spectrum resulting from them will not convey any meaningful information. It has hence not been plotted alongside the power spectrum for the slightly higher fidelity modelling performed for the 5 metre datasets (Figure 4.19).

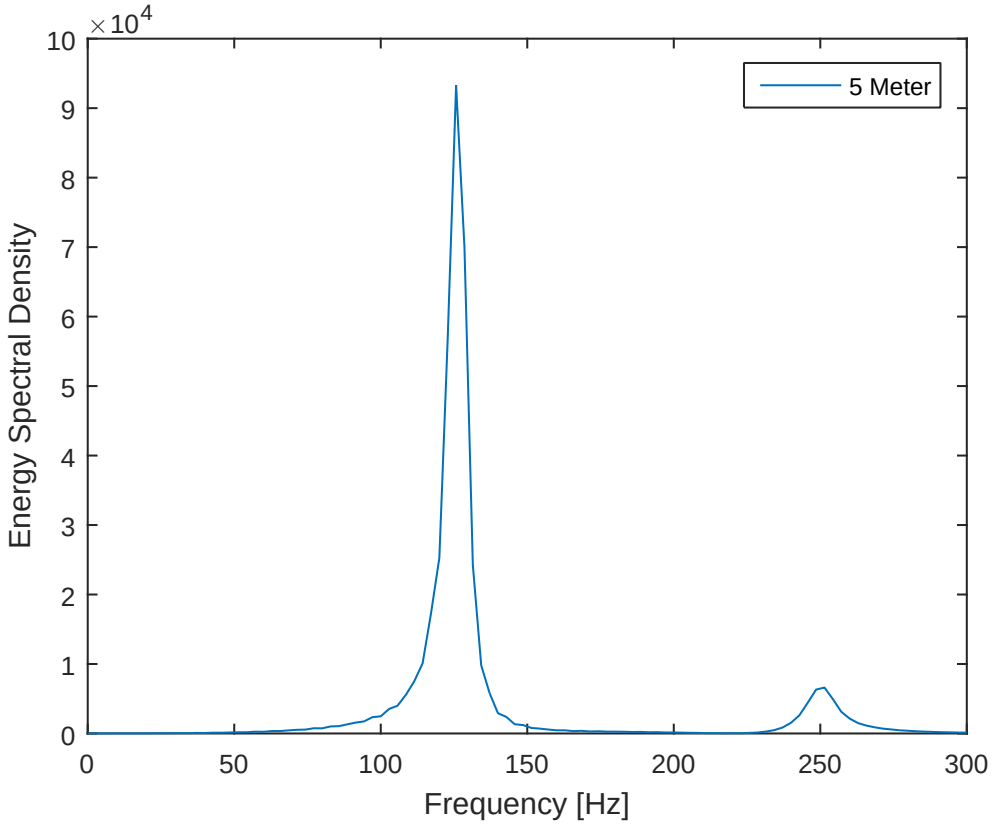

Figure 4.19: Energy distribution over frequency for the post-collapse micro-oscillations modelled for the 5 metre source depth datasets. Notice that the absolute values are lower than in Figure 4.17.

4.2 NRMS and Time of Bubble Breaching

In the previous section the power-spectrum of the differential was compared to that of an equally long post-shot noise record. A procedure to identify when the main bubble no longer influenced measurements was developed to prove that this latter spectrum was indeed unaffected by bubble dynamics. This section is dedicated to presenting said procedure, and the results it produced. Much of the theory applied here is peripheral to the micro-oscillation analysis, and has therefore been included in the appendix rather than in Chapter 2.

An important difference between this investigation and the inverse-modelling is the significance of noise: As the signal becomes progressively weaker, the noise becomes relatively stronger. This skews the results when performing operations such as calculating repeatability, and especially so if the noise is continuously supplied to the dataset throughout all measurement periods. Such ambient noise is, however, easily isolated by using power spectra, as one of their characteristics is that energies at the same frequency accumulate. For long measurement times repeatable noise therefore dominates the spectra as peaks. Taking advantage of this, notch filters were designed to remove frequencies such as the Gunnerus' mains frequency (60 Hz) from the dataset. Swell noise, covering a range of low frequencies rather than any particular one, was found to be eliminated when using a highpass frequency of 15 Hz. According to Eq. (B.3), reproduced below from Section B.1 in the appendix, bubble oscillation period decreases with depth. Coupled with the fact that bubbles lose most of their energy over the course of their collapse, this implies a faster convergence to the NRMS noise-ceiling for deeper shots.

$$\eta(t) = \frac{t}{\tau} = tk\frac{(z(t)+10)^{5/6}}{(p_0V_0)^{1/3}} = kt(z_{t=0} - v_r t + 10)^{5/6} \tag{B.3}$$

The theory behind NRMS, or Normalised Root-Mean-Square deviation, has also been covered in Section B.1. In this context, it suffices to say that it is a measure of difference between two datasets. With an NRMS value of $\sqrt{2}$ (1.41), both of the datasets are considered to only contain random noise, whereas lower values signify a better match. By calculating the NRMS values in stages using a moving window, it is possible to discern how repeatability changes over time. This has been done for the 3 and 5 metre source

depths in Figure 4.20.

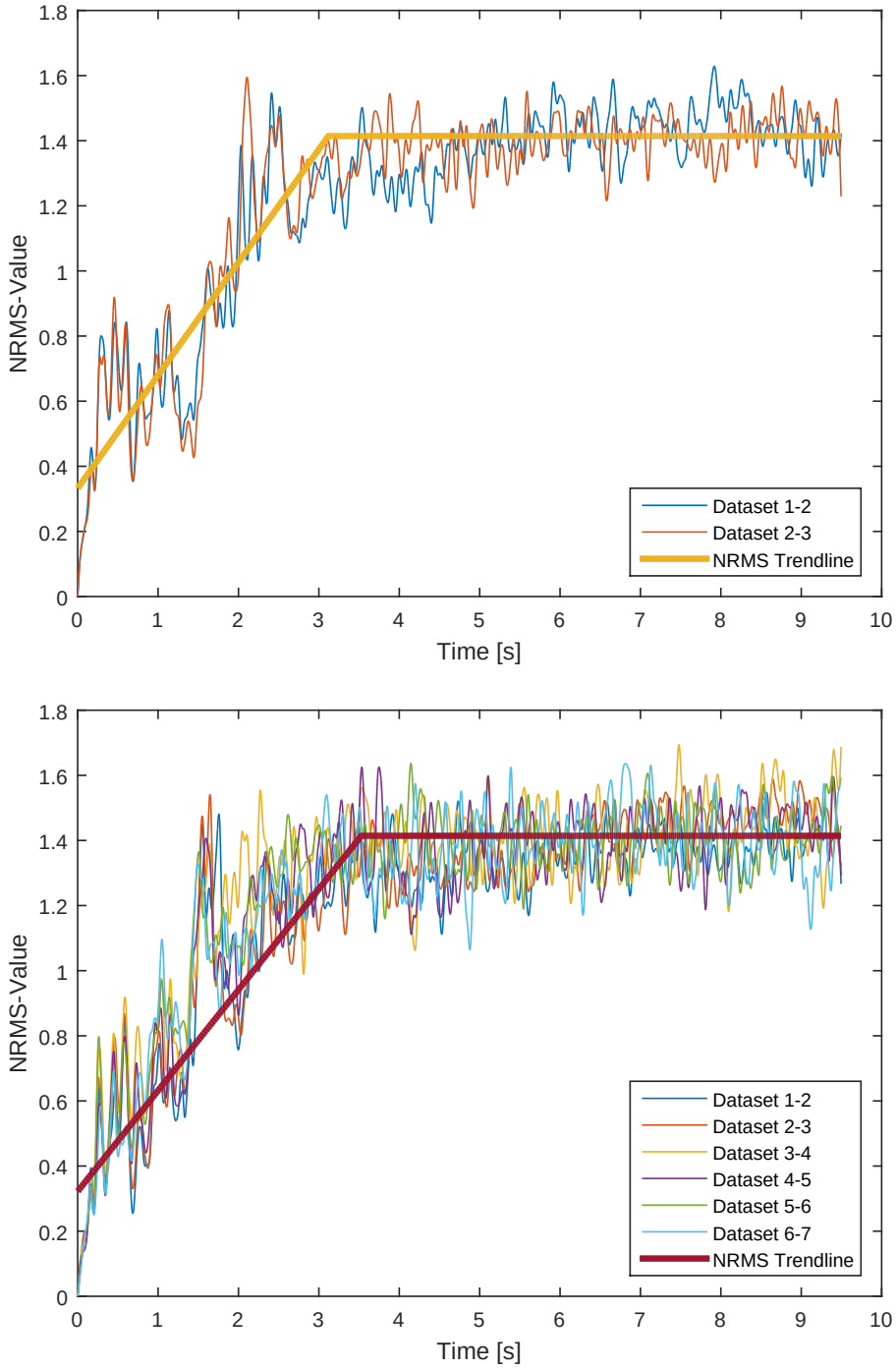

Figure 4.20: NRMS plots constructed of the 3 metre source depth datasets using a moving window of 10 ms (20 indeces) width. This width was chosen due to the low amount of lag found between datasets. The datasets have been highpassed to remove swell noise, and smoothed to extract a sensible behaviour. Only a subset of the 5 metre datasets were included in the analysis to speed up processing.

The trendline superimposed on the NMRS-plots above was constructed using an iterative best-fit method whereupon the x_0-, y_0-, and the x_1-coordinates were given no restrictions.

As can be observed, the latter of these correspond to the time at which the NRMS values reach the noise ceiling. Storing the x_1-values for each successive source depth hence allowed the construction of Figure 4.21.

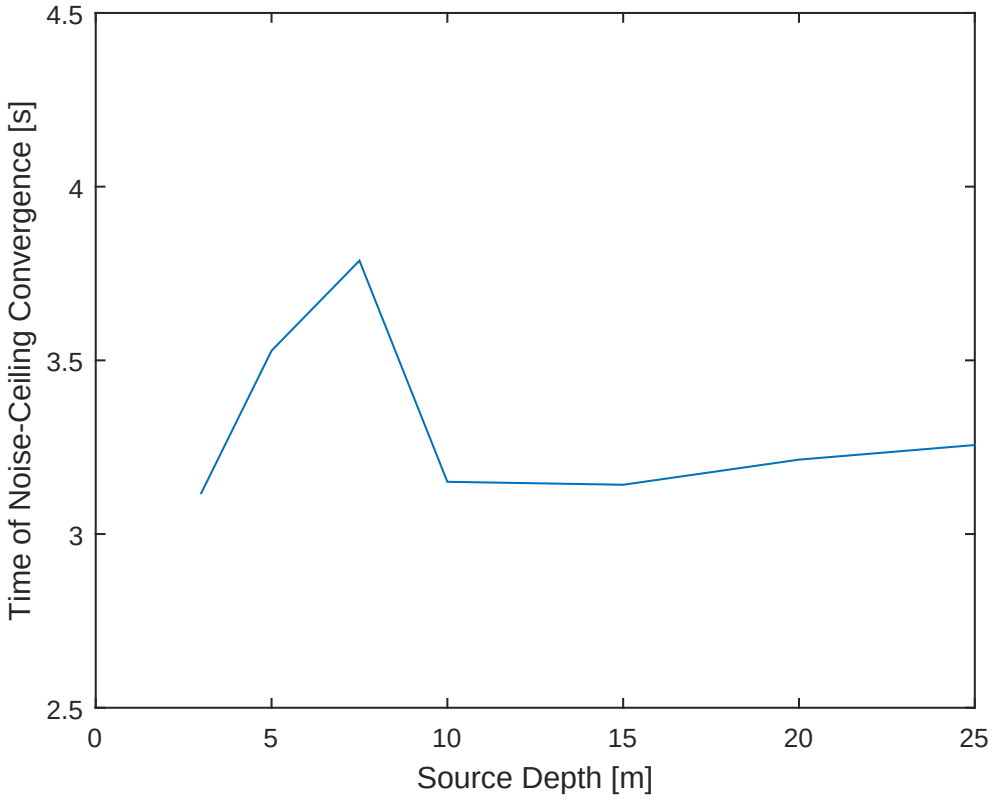

Figure 4.21: Time at which the NRMS plots of each respective source depth reached the noise-ceiling (an NRMS value of $\sqrt{2}$). The datasets gathered with the source at 30 - 40 metres proved to be particularly noisy and have been left out of the analysis.

If the bubble's life was truncated by it reaching the surface, one would - according to the theory put forth in Appendix B - expect its NRMS value convergence to $\sqrt{2}$ to occur at a steadily increasing recording time as the source is lowered. This is indeed what is observed in Figure 4.21 with the source at 3 to 7.5 metres depth. There is, however, a shift in NRMS behaviour for deeper shots. One possible explanation can be found when considering that the datasets were not lowpassed: Opening up the frequency range namely allows larger amounts of high-frequency noise into the analysis - raising the RMS noise-floor, and speeding up convergence to the NRMS noise-ceiling. Still, the noise-floors are not significantly higher for the deep datasets than for the shallow ones, leading to the possible conclusion of more repeatable high-frequency signals being generated for a

longer period of time by the shallower shots.

Theoretically, it should also possible to uncover a more distinct trend in Figure 4.21 for the deeper shots if they were bandpassed around the frequency of the main bubble: Not having the repeatable high-frequency signal of the shallower ones, frequency-filtering them should namely increase the overall signal-to-noise ratio. On the back of this, the NRMS noise-ceiling should either be hit progressively later for increasing depths (as the bubble breaks the surface), or earlier (due to it breaking up faster). A transition between the two when moving from one depth to another, as is illustrated in Figure 4.22, is also possible. An extensive investigation was set into action to determine whether any of these could in fact be found in the data, but none of the expected trends could be distinctly observed from the resulting depth/NRMS plots. This could possibly be because increasing the depth lowers the repeatability altogether: For one, the longer the bubble rises, the more its travelpath might deviate between shots.

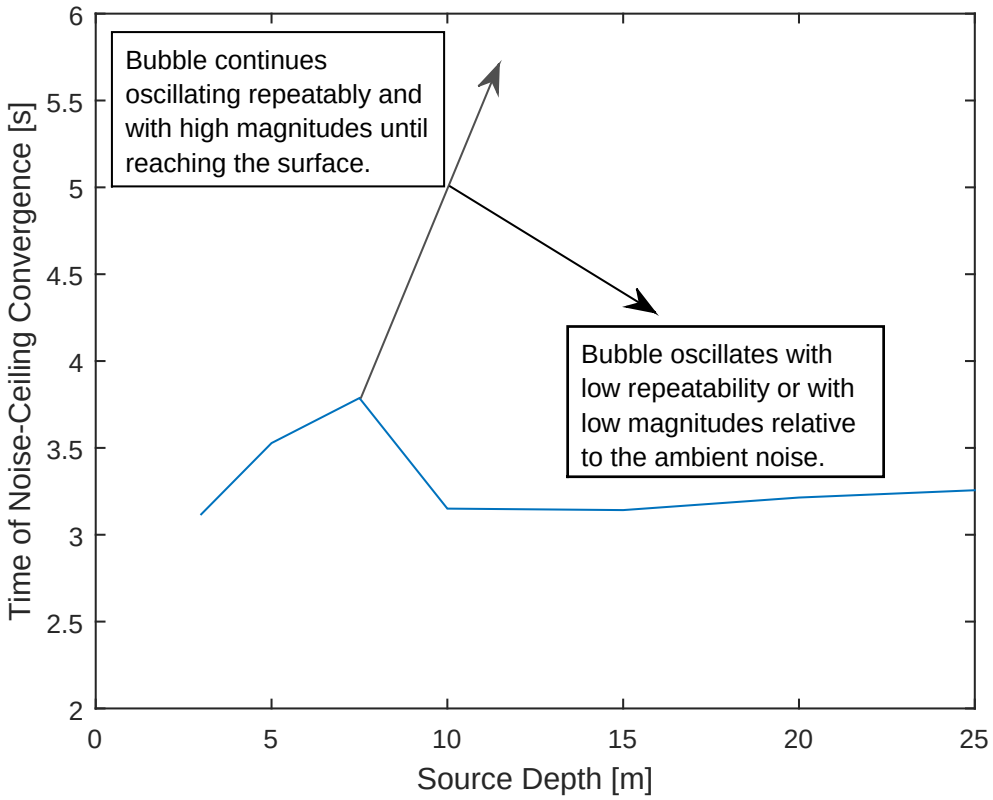

Figure 4.22: Projected NRMS trends for the deeper datasets given isolation of the main bubble's frequency.

The high-frequency signals causing good repeatability for the shallower datasets are not

likely to be acoustic radiations from the main bubble: Being exposed to a lower external pressure at shallow depths, it will actually oscillate at a lower frequency here than deeper. It could, however, cause them indirectly: Each of its collapses is followed by a violent expansion which creates turbulent conditions in the surrounding water. This turbulence might then create pockets where the absolute water pressure drops drastically. If said pressure reaches the saturation pressure, water will rupture and undergo a phase transition into vapour. The "voids" in the liquid formed by said vapour are called cavities, and are collectively referred to as cavitation clouds. When turbulence eventually decreases, the cavities are in disequilibrium with the surrounding pressure. This causes a swift collapse, and emission of acoustic radiation at frequencies in the kHz-range (too weak and high-frequent to cause the micro-oscillations) *(Khodabandeloo and Landrø, 2017)*.

Cavities might also form due to the presence of the air gun - having sharp edges over which water moves at a rapid velocity *(Landrø et al., 2011)*. Whatever their formation mechanism in this particular survey, their life-cycle is the same: Cavities generally expand to many times their original size before collapsing violently in on themselves, often disintegrating into many yet smaller bubbles. Throughout this singular cycle the mass of the vapour within the cavities will vary, but the pressure will always hover around the saturation pressure. When the hydrostatic pressure again becomes dominant there is thus little residual compressed gas to cushion the collapse *(Ronald, 1999)*. The resulting implosion is violent, momentarily producing extreme temperatures and pressures; in one experiment the temperature was measured to reach several thousand Kelvin *(Brenner et al., 2002)*.

While the pressure emission by each collapsing cavity is non-repeatable, the combined pressure output from the cavitation cloud they comprise might be: Caused by the (repeatable) oscillations of the main bubble it should form at the same time and depth given the same initial conditions. This provides an explanation for the high repeatability observed at shallow depths. Seeing as the air gun was fired with the same initial pressure throughout the survey, there should exist a threshold depth at which the hydrostatic pressure is too great to allow sustained creation of cavities. From Figure 4.21 it is reasonable to assume this threshold to be between 7.5 and 10 metres. While the deeper bubbles eventually rise past this threshold, they have either lost too much energy-, or have moved out of range of

the nucleation point (sharp edges of the air gun) to cause sufficient cavitation to continue the NRMS trend seen for the shallower source depths. Equation (B.5), included below from Appendix B is a rough mathematical description of the relation between cavitation and source depth when close to the bubble wall.

$$\dot{R} = \sqrt{\frac{2p_\infty}{\rho}} \tag{B.5}$$

In summary, as depth increases, the relative difference in water particle velocity necessary to create cavitation also increases. When inverse-modelling the signatures for increasing depths, the bubble wall velocity, and by proxy the adjacent water particle velocity, behaved much like the bubble radius: For the first expansion more violence was displayed for the shallow shots - yielding both higher velocities and larger radii. Less velocity was "lost" per oscillation for deeper bubbles, but over longer time-spans the shallower ones retained higher absolute speeds. It was decided not to include plots of the modelled main bubble wall velocity due to the normalisation of the data, and the accompanying uncertainties mentioned in Chapter 3.

Taken at face-value, Figure 4.21 thus implies that the average bubble rise velocity for the 3, 5 and 7.5 metre source depths are 0.94 m/s, 1.42 m/s and 1.98 m/s respectively. Theoretically, firing depth could account for some of the difference: According to *(Langhammer and Landrø, 1996)*, Eq (4.1) provides an estimate of bubble rise velocity v_r development.

$$v_r = \frac{2g}{R(t)^3} \int_0^t R(t)\,\mathrm{d}t \tag{4.1}$$

Due to the $1/R(t)^3$-term, the bubble velocity increases the most at its radial minima. With a higher surrounding hydrostatic pressure the bubble is more "squeezed" together, and its average radius will be smaller over time. Nevertheless, this effect is not likely to have a huge impact due to the small differences in hydrostatic pressure actually observed for these source depths. Rather, the low apparent velocity observed for the 3 metre source depth dataset is likely to be found in another possible cause of repeatable high-frequency signals; the bubble actually breaching the surface. As shown in Figure 4.23, this is a violent event, and may therefore produce a powerful high-frequency signal itself. Thus, the NRMS values can be assumed to converge to $\sqrt{2}$ not immediately as the bubble reaches

the surface, but after its violent venting has completed. A point in support of this claim, and indeed of the central hypothesis of this section, is the video of which the snapshots in Figure 4.23 was captured: With the source at 3 metres it takes between one and two seconds for the bubble to reach the surface, and about another second for the venting to complete. Another video of one of the shots fired at 5 metres depth shows the bubble taking between two and three seconds in reaching the surface, and slightly less than a second in venting. The event is less violent than for 3 metres (see Figure 4.24), but is still likely to emit high-frequency noise, meaning these timings match well with those found in Figure 4.21. While no video exists of the bubble generated at 7.5 metres depth, one was shot of the 10 metre depth one. Figure 4.25 shows that bubble breaching is for this case a rather calm event, and should not produce significant amounts of high-frequency noise. Its rise to the surface took approximately five seconds (matching well with the rise velocity calculated for the 7.5 metre source depth. The bubble released at 7.5 metres depth will naturally behave somewhere in-between what is illustrated in Figures 4.24 and 4.25. Generating less high-frequency noise by its venting than the bubbles released at shallower depths, its apparent average rise velocity is likely to be closer to the true average.

Therefore, to conclude, while the videos thus strongly imply the theory to be valid (at least for shallow datasets), the attentive reader will note that finding these very timings was what launched the investigation in the first place. However, seeing that access to the survey videos was granted in its end-stages, said investigation was necessary when initiated. The results and process developed could also be of use to future surveys where no videos have been recorded.

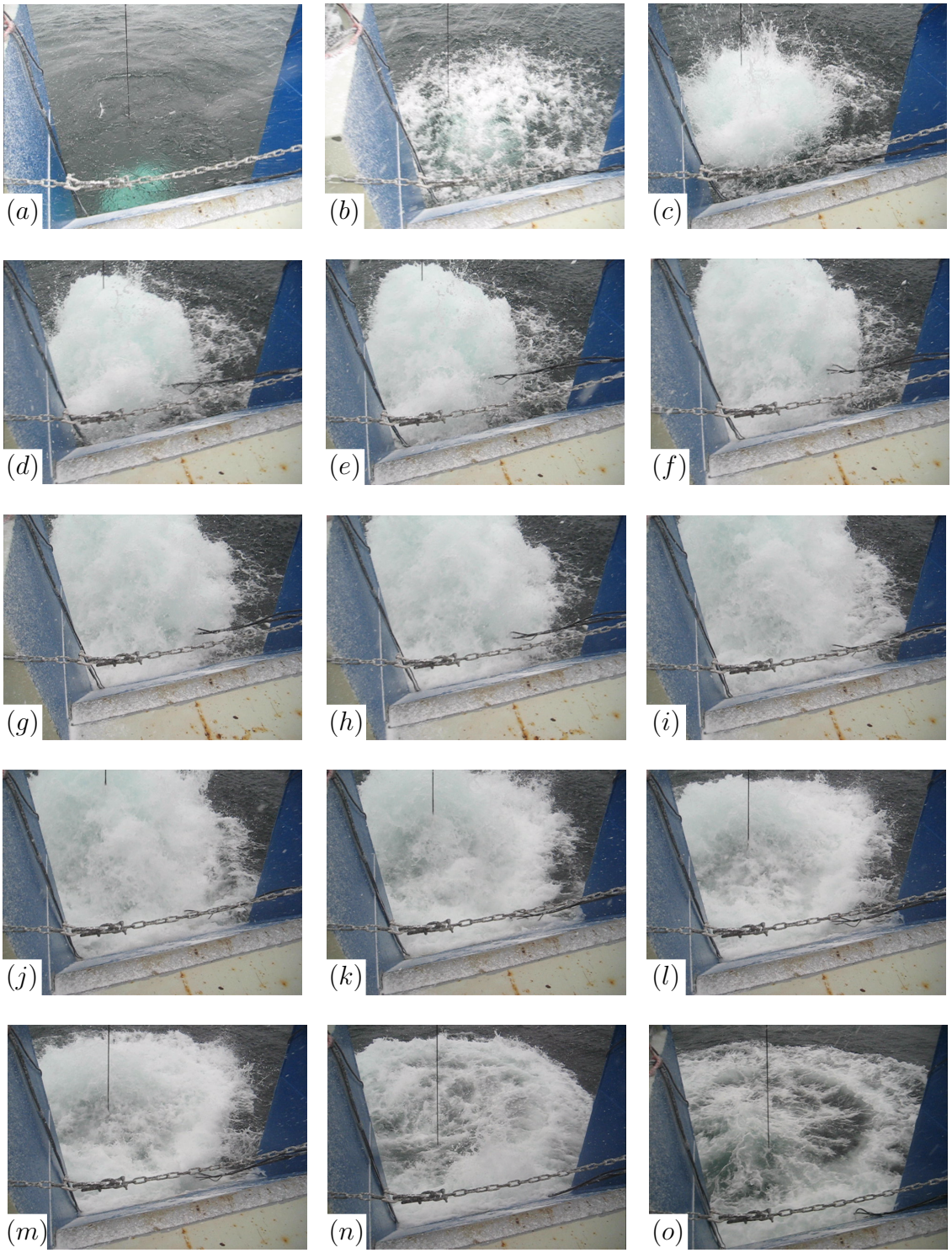

Figure 4.23: Snapshots of a video filmed with the source at 3 metres depth.
a) The bubble is formed.
b) The primary reaches the surface.
c $\rightarrow$ i) The bubble reaches the surface and vents into the atmosphere explosively.
j) $\rightarrow$ n) The water thrown skywards by the bubble falls back down.
o) Later sloughing due to the disturbance.

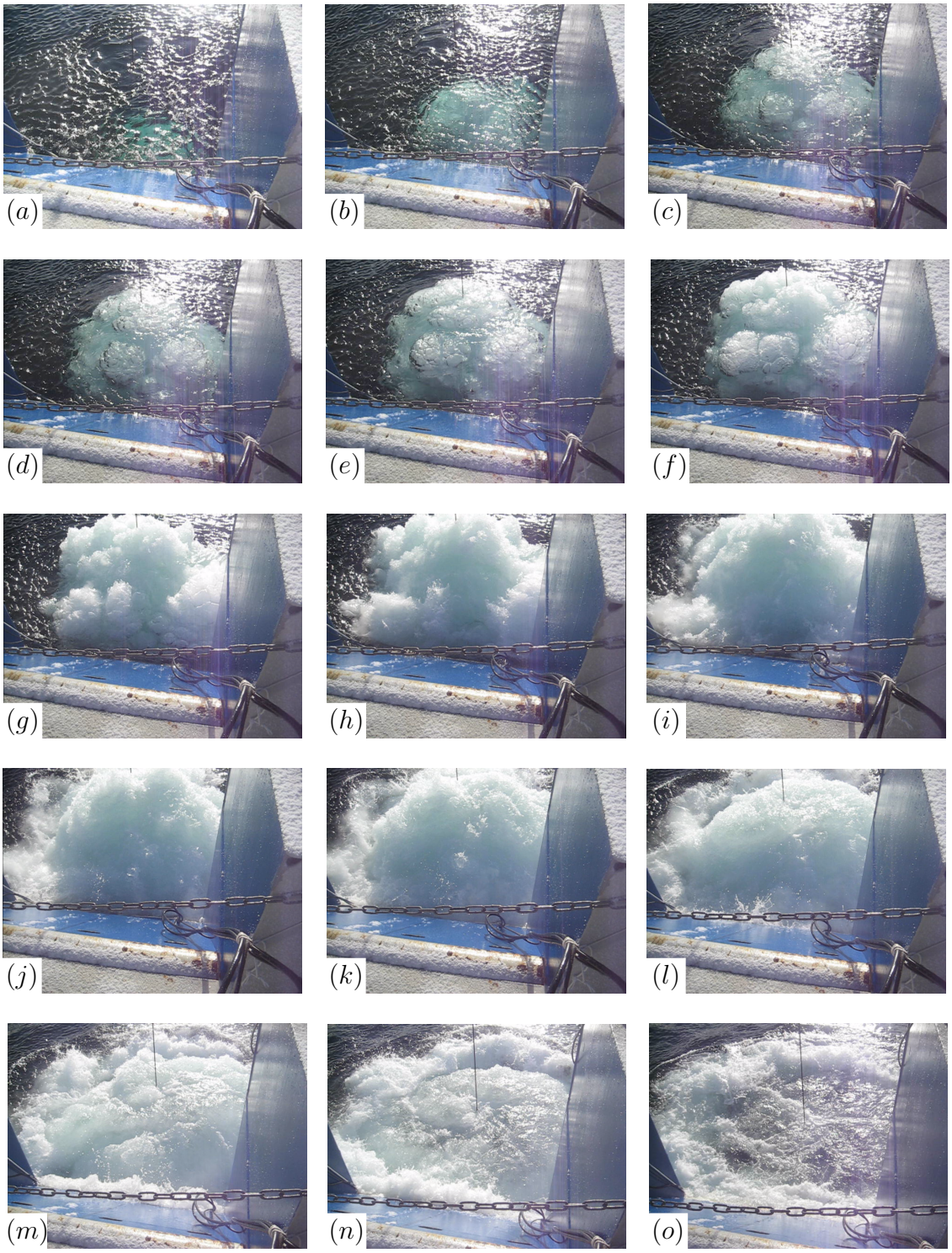

Figure 4.24: Snapshots of a video filmed with the source at 5 metres depth.
a) The bubble moves into frame.
b) → d) The bubble moves towards the surface, breaking up more and more in the process.
e) → i) The bubble reaches the surface and vents into the atmosphere explosively.
j) → n) The water thrown skywards by the bubble falls back down.
o) Later sloughing due to the disturbance.

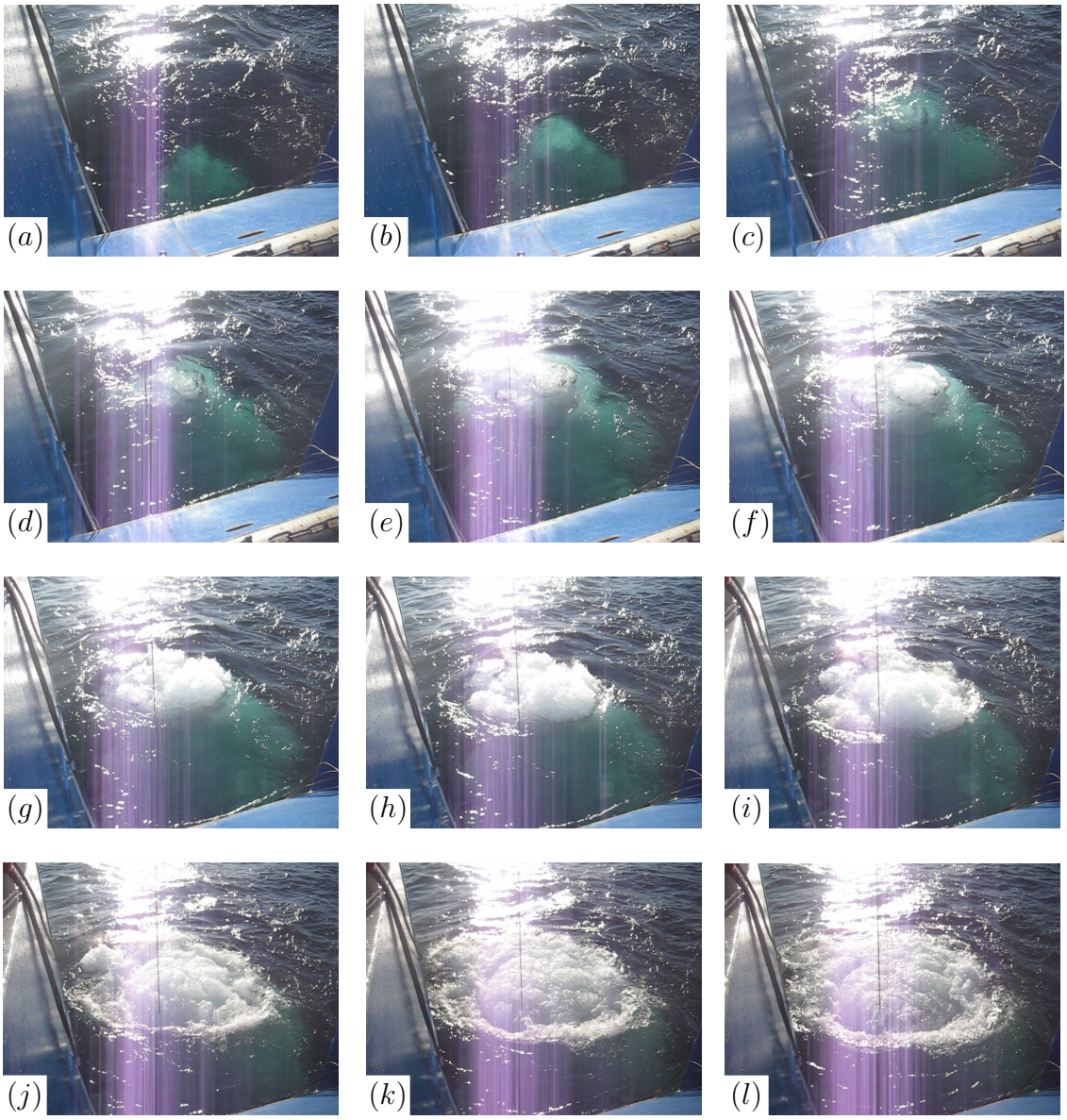

Figure 4.25: Snapshots of a video filmed with the source at 10 metres depth. Some detail is lost due to glare from the sun off the sea surface.
a) The bubble moves into frame.
b) $\rightarrow$ d) The bubble moves towards the surface, breaking up more and more in the process.
e) $\rightarrow$ i) The bubble, now severely broken up, reaches the surface and vents relatively non-explosively.
j) $\rightarrow$ k) The water displaced upwards by the bubble falls back down.
l) Small bubbles broken off by the main bubble in its ascent continue to stream to the surface.

Chapter 5

Conclusion

The aim of this thesis has been to investigate and ascertain the origin of repeatable micro-oscillations recorded by a survey performed in the Trondheim Fjord. This necessitated isolating them from the influence of the main bubble, which was achieved through inverse-modelling its behaviour and subtracting it from the dataset. Said inverse-modelling was performed under the governance of a genetic algorithm developed for the occasion, and the bubble dynamics equation used in this endeavour was put together using the works of multiple authors.

The isolated micro-oscillations were proved to be gun-related, consistently dropping in energy from their first appearance and displaying a high repeatability. Having eliminated external noise sources as a factor, there remain many possible mechanisms for their generation, including gun-/hydrophone movement amongst others. The central hypotheses investigated have, however, been *The Precursor Hypothesis* and *The Bubble Spawn Hypothesis* (hyperlinked) which were both tested using the inverse-modelling scheme developed.

From said inverse-modelling, it was found that the influence of the main bubble on the precursor was too great for the precursor hypothesis to be valid. The effect could have been reduced by increasing the distance between the two, but it was assumed that the geometry of the air gun used in the experiment set an upper limit of 0.5 metres. The bubble-spawn hypothesis fared better, as inverse-modelling with the assumptions it prescribes yielded a good match with the measured pre-collapse micro-oscillations. This, coupled with the micro-oscillations appearing to arise after the passing of the ghost, is a

strong point in its favour. However, a dedicated experiment is still needed to conclusively verify it. Inversion of the post-collapse micro-oscillations did not produce an equally good match, which could be due to the increased turbulence and ensuing complexity caused by the collapse. Any inversion-scheme wishing to reproduce these later micro-oscillations would therefore need to account more carefully for multiple bubbles of varying sizes, and the interaction between them - especially for shallow shots.

Due to the datasets being normalised there is some uncertainty in determining whether the bubble parameters found accurately represent real-life values. Equation (2.6) has many degrees of freedom and there are subsequently many potential local minima when minimising the deviation function. While the inversion-scheme was run multiple times to find the lowest deviation, it is possible that the solution converged to is only an easily accessible local minimum, with the global minimum being hard to reach. Until this investigation is reproduced on a non-normalised dataset, less attention should be given to the actual values (Tables 4.1 to 4.4), and more to the visual reproduction of the signal (Figures 4.5, 4.15, 4.16, and 4.18).

In the process of analysing the datasets, it was found that a relation existed between the NRMS plots of the direct signals and the bubble's rise to the surface: At shallow source depths the time of convergence to the noise-ceiling correlated well with the main bubble's breaching of the surface and venting into the atmosphere. Conversely, a nearly flat trend was found for the deeper shots. This was hypothesised to be due to lower amounts of (high-frequency) cavitation at depth. It was from there conjectured that the deeper shots would, if frequency filtered to the main bubble's oscillatory frequency, display a distinct trend. However, none could be uncovered.

Bibliography

Ayzenberg, M., Tsvankin, I., Aizenberg, A., Ursin, B., 2009. Effective reflection coefficients for curved interfaces in transversely isotropic media. Geophysics 74 (5), WB33–WB53.
URL https://doi.org/10.1190/1.3197862

Boeda, E., Bonilauri, S., Connan, J., Jarvie, D., Mercier, N., Tobey, M., Valladas, H., al Sakhel, H., 2008. New evidence for significant use of bitumen in middle palaeolithic technical systems at umm el tlel (syria) around 70,000 bp. PalÃl'orient 34 (2), 67–83.
URL http://www.jstor.org/stable/41496524

Brenner, M., Hilgenfeldt, S., Lohse, D., 2002. Single bubble sonoluminescence. Reviews of modern physics 74 (2), 425–484.

Chahine, G. L., 1982. Experimental and asymptotic study of nonspherical bubble collapse. Applied Scientific Research 38 (1), 187–197.

de Graaf, K., Brandner, P., Penesis, I., 2014. Bubble dynamics of a seismic airgun. Experimental Thermal and Fluid Science 55, 228 – 238.
URL http://www.sciencedirect.com/science/article/pii/S0894177714000491

Energy Education, 2006. Oil formation.
URL http://energyeducation.ca/encyclopedia/Oil_formation

Groenaas, H., Gerez, D., Larsen, O. P., Padula, M., 2016. On the anatomy of the air-gun signature. pp. 46–50.

URL http://library.seg.org/doi/abs/10.1190/segam2016-13841168.1

Hutchinson, D. R., Detrick, R. S., Sep 1984. Water gun vs air gun: A comparison. Marine Geophysical Researches 6 (3), 295–310.
URL https://doi.org/10.1007/BF00286531

International Energy Agency, 2018. Oil market report.
URL https://www.iea.org/oilmarketreport/omrpublic/

Johnson, D. T., 1994. Understanding air-gun bubble behavior. Geophysics 59 (11), 1729.
URL http://dx.doi.org/10.1190/1.1443559

Keller, J. B., Kolodner, I. I., Oct. 1956. Damping of Underwater Explosion Bubble Oscillations. Journal of Applied Physics 27, 1152–1161.

Khodabandeloo, B., Landrø, M., 2017. High frequency ghost cavitation - a comparison of two seismic air-gun arrays using numerical modelling. Energy Procedia 125, 153 – 160, european Geosciences Union General Assembly 2017, EGU Division Energy, Resources & Environment (ERE).
URL http://www.sciencedirect.com/science/article/pii/S1876610217336512

Kirkwood, J., 1942. OSRD Report no. 588. National Defense Research Committee of the Office of Scientific Research and Development.

Kragh, E., Christie, P., 2002. Seismic repeatability, normalized rms, and predictability. The Leading Edge 21 (7), 640–647.
URL https://doi.org/10.1190/1.1497316

Landrø, M., 12 1992. Source signature determination by inversion. Geophysics.

Landrø, M., Amundsen, L., Barker, D., 2011. High-frequency signals from air-gun arrays. GEOPHYSICS 76 (4), Q19–Q27.
URL https://doi.org/10.1190/1.3590215

Landrø, M., Ni, Y., Amundsen, L., 2016. Reducing high-frequency ghost cavitation signals from marine air-gun arrays. Geophysics 81 (3), 33–46.
URL https://doi.org/10.1190/geo2015-0305.1

Landrø, M., Zaalberg-Metselaar, G., Owren, B., Vaage, S., 1993. Modeling of water-gun signatures. Geophysics 58 (1), 101.
URL +http://dx.doi.org/10.1190/1.1443339

Langhammer, J., 1994. Experimental studies of energy loss mechanisms in airgun bubble dynamics.

Langhammer, J., Graciet, S., Vik, I., Espeland, M., Løkberg, O. J., 1995. Holographic studies of the bubble generated by a seismic airgun. The Journal of the Acoustical Society of America 97 (1), 362–369.
URL https://doi.org/10.1121/1.412321

Langhammer, J., Landrø, M., 1996. High-speed photography of the bubble generated by an airgun. Geophysical Prospecting 44 (1), 153–172.
URL http://dx.doi.org/10.1111/j.1365-2478.1996.tb00143.x

Lecerf, D., Burren, J., Hodges, E., Barros, C., 2015. Repeatability measure for broadband 4D seismic. pp. 5483–5487.
URL https://library.seg.org/doi/abs/10.1190/segam2015-5927745.1

Pedersen, Å., 2009. Sources & Signals - Phase II. Presentation.

Rayleigh, L., 1917. Viii. on the pressure developed in a liquid during the collapse of a spherical cavity. Philosophical Magazine 34 (200), 94–98.
URL http://dx.doi.org/10.1080/14786440808635681

Ronald, Y., 1999. Cavitation. World Scientific Publishing Company.
URL https://books.google.no/books?id=H_e3CgAAQBAJ

Vaage, S., Haugland, K., Utheim, T., 2006. Signatures from single airguns. Geophysical Prospecting 31 (1), 87–97.

URL https://onlinelibrary.wiley.com/doi/abs/10.1111/j.1365-2478.1983.tb01043.x

Ziolkowski, A., 1970. A method for calculating the output pressure waveform from an air gun. Geophysical Journal of the Royal Astronomical Society 21 (2), 137–161.
URL http://dx.doi.org/10.1111/j.1365-246X.1970.tb01773.x

Ziolkowski, A. A., Parkes, G. E., Hatton, L., Haugland, T., 1984. The signature of an air gun array; computation from near-field measurements including interactions. Geophysics 49 (2), 105–111.
URL http://geophysics.geoscienceworld.org/content/49/2/105

Appendix A

5 Metre Source Depth Plots

Most of the discussion related to these results have already been covered in Section 4.1, and points raised there will not be restated here. Rather, the aim of this section is to provide the reader with additional plots by which to contrast the results found for the 3 and 5 metre datasets if so desired.

The measured main bubble signal for the 5 metre source depths could not be satisfactorily modelled with conservative constraints. To make the inverse-modelling converge on the answer either initial air gun-pressure or volume had to be increased beyond the survey specifications. There may be many potential influencing factors contributing to the discrepancy: Perhaps most intuitive, the air gun might actually have been fired at a higher pressure than specified. According to Martin Landrø who was present at the survey, the firing pressure had an approximate uncertainty of 5 bars. Coupled with the fact that source depths were not measured with high precision, this could account for at least some of the divergence (149 bars vs 140 bars). Conceivably, the parameters granting the global minima of the deviation function *within* the conservative constraints could also be hard to reach for the genetic algorithm applied. The actual values converged upon, and the signature they generate, are found in Table A.1 and Figure A.1.

Table A.1: Parameters used to model the 5 metre source depth main bubble signal in Figure A.1. Note that these yield only one of many local minima in the deviation function: Another solution converged to a pressure within the mission specifications, but with an initial volume larger than the firing chamber.

R	Ψ	α	β	β_2	p_0	V_0
[ø]	[ø]	[m^2/s^2]	[m^4/s^4]	[m^4/s^5]	[Pa]	[in^3]
-1.375	7.919	0.130	0.095	0	149×10^5	599

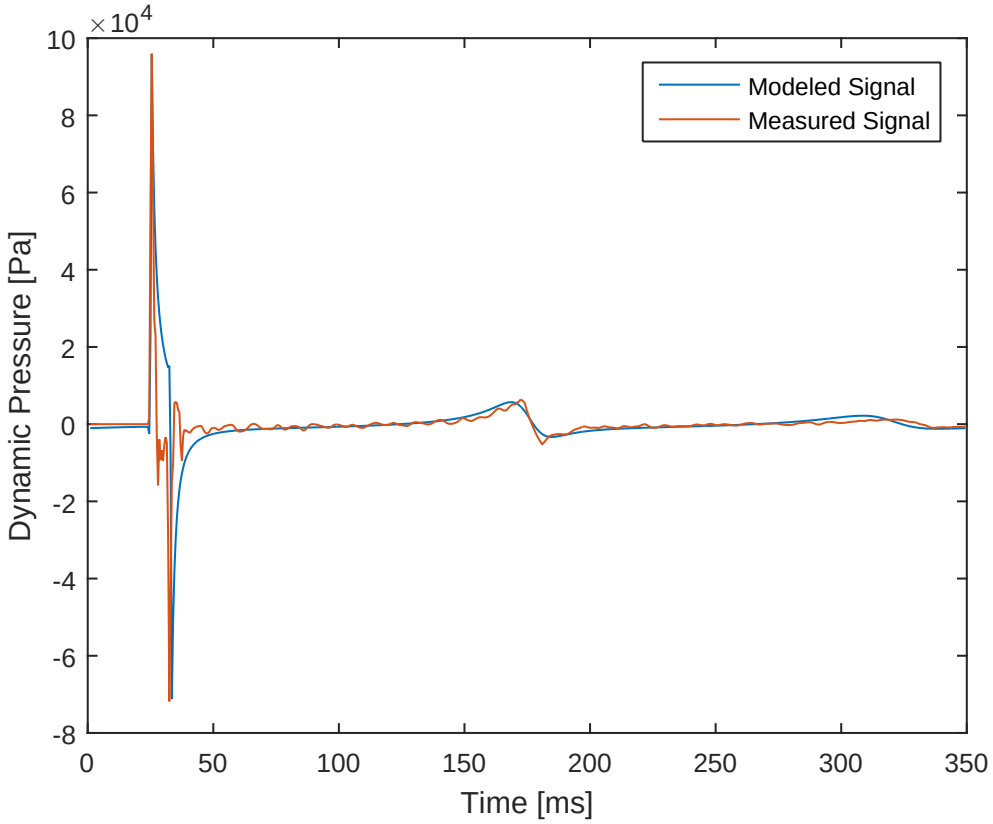

Figure A.1: Measured- and inverse-modelled signatures overlain each other for a shot fired at 5 metres depth. Magnitudes displayed in the plot are the ones found through inverse-modelling, and cannot be verified due to the normalisation of the measured dataset. The signal labelled "measured" has undergone a lowpass for illustrative purposes.

The 5 metre source depth micro-oscillations were isolated following the process described in the main body of the thesis. Also following said procedure, their power spectra were calculated, and these been displayed below the differentials in Figure A.2.

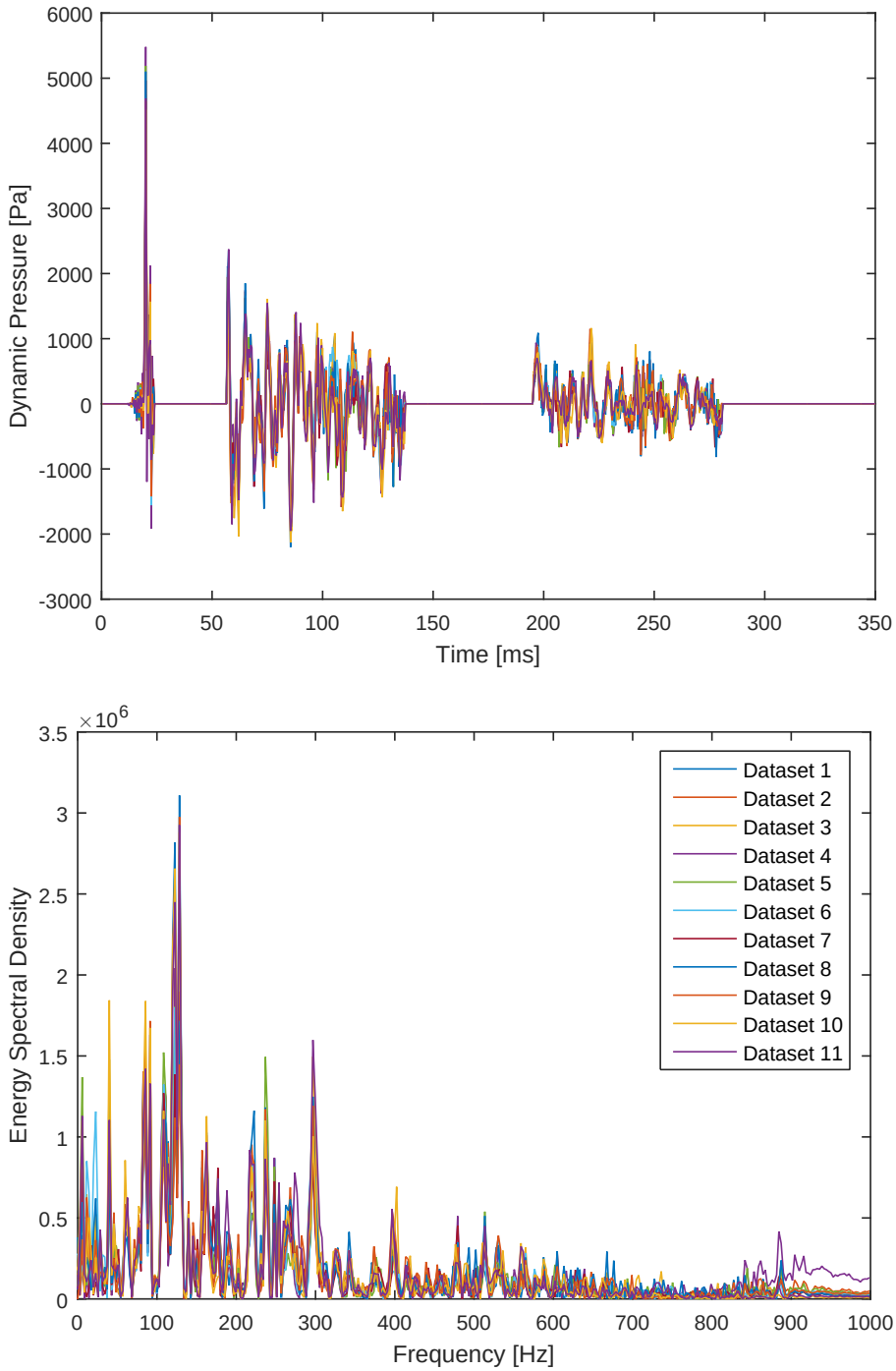

Figure A.2: Differentials and frequency spectra for the 5 metre source depth datasets. The legend could not be legibly displayed when plotting the differentials without covering the data. It has, however, been included with the same colour-coding with the power spectra below.

Like done for the 3 metre datasets, a conservative frequency range was chosen, removing data outside the 70 - 200 Hz range. The resulting bandpassed differentials are found in Figure A.3.

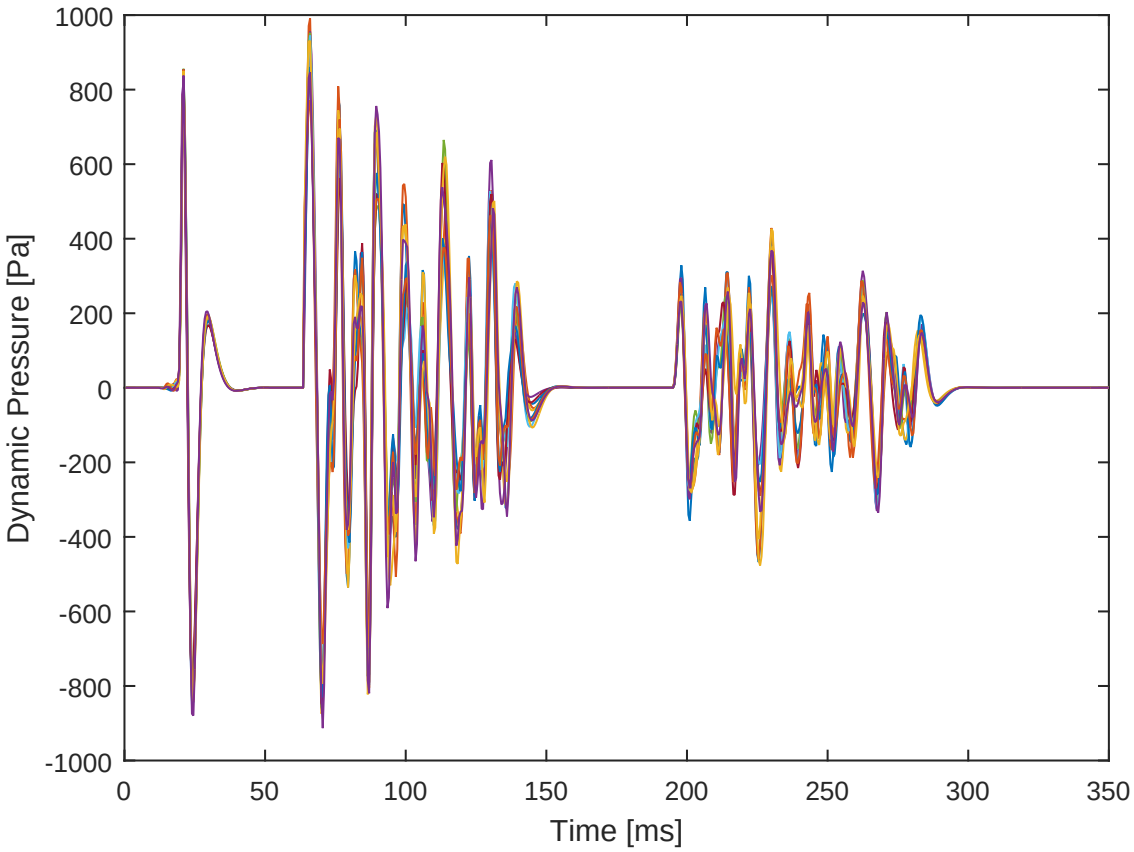

Figure A.3: Bandpassed 5 metre source depth differentials. Colour-coding is the same as in Figure A.2.

The advantage of stacking many shots is that more random noise is eliminated, and signal skipping is reduced to the average. Figure A.4, being comprised of 11 shots can thus be assumed to act as a good representation of isolated micro-oscillation.

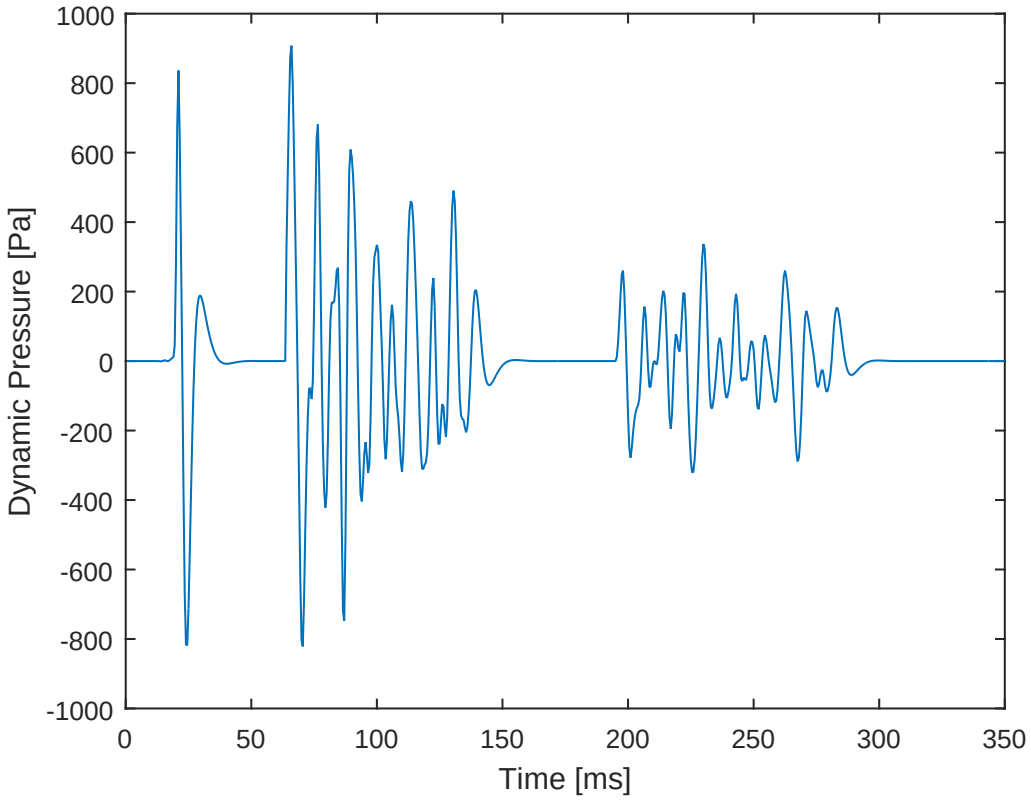

Figure A.4: Result of stacking the bandpassed 5 metre source depth differentials.

Having earlier found strong evidence for the precursor hypothesis' invalidity, the inverse-modelling under its prescribed conditions was not redone for the 5 metre dataset. Inverse-modelling was, however, performed under the conditions of the bubble spawn hypothesis. As for the 3 metre source depth analysis, good results were found for the pre-collapse micro-oscillations (Figure A.5), and poor results were found for the post-collapse ones (Figure A.6). The parameters to generate the modelled signals shown have been included in Tables A.2 and A.3 below each respectable figure.

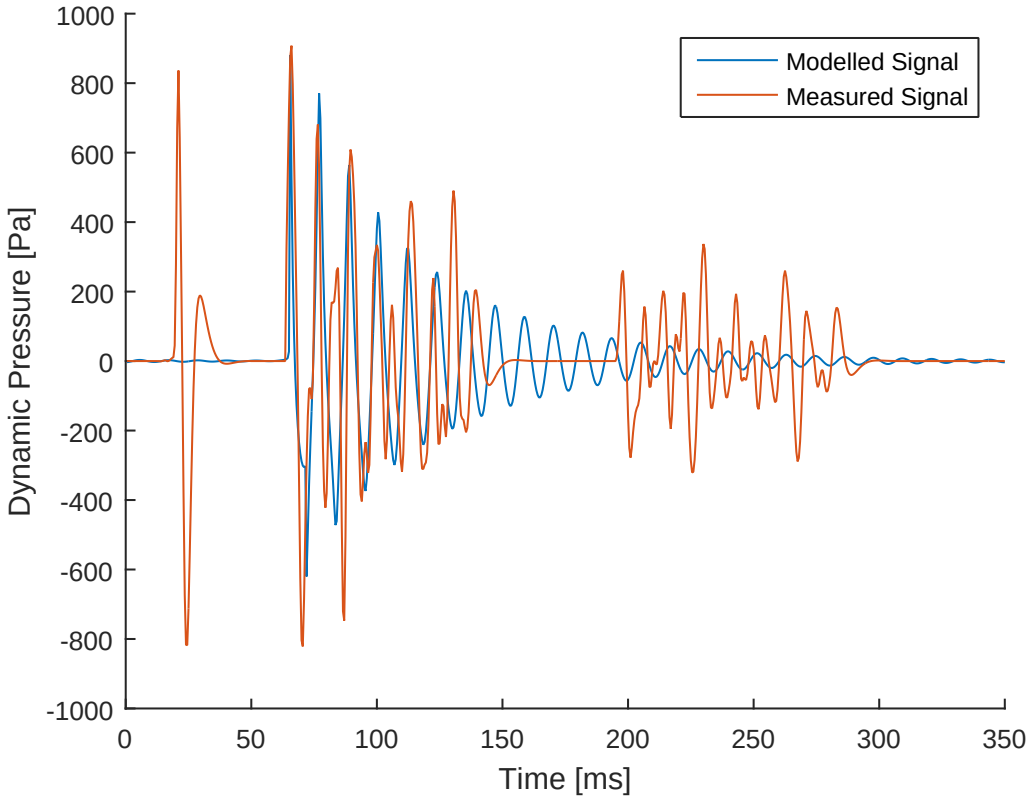

Figure A.5: Result of inverse-modelling the 5 metre source depth pre-collapse micro-oscillations under the bubble-spawn hypothesis.

Table A.2: Parameters used to model the 5 metre source depth pre-collapse micro-oscillations in Figure A.5.

R	Ψ	α	β	β_2	p_0	V_0
[ø]	[ø]	[m^2/s^2]	[m^4/s^4]	[m^4/s^5]	[Pa]	[in^3]
-0.515	0.220	1.928	-0.001	0	2.750×10^5	10.964

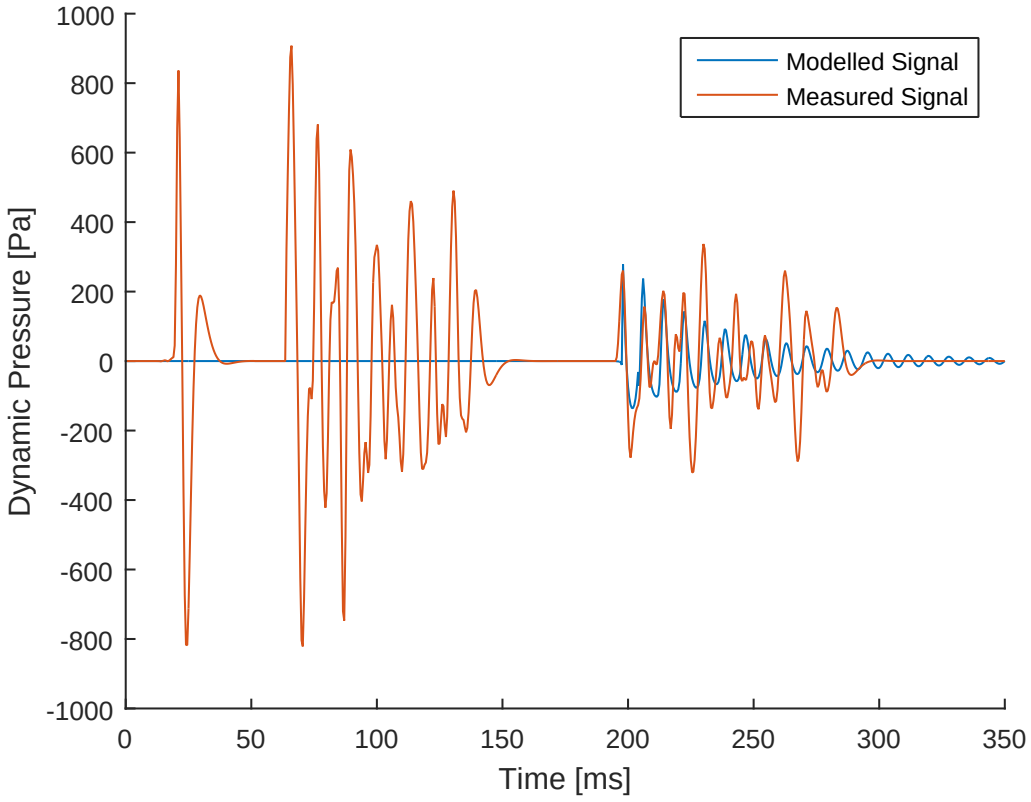

Figure A.6: Result of inverse-modelling the post-collapse micro-oscillations for the 5 metre source depth datasets under the bubble-spawn hypothesis.

Table A.3: Parameters used to model the 5 metre source depth post-collapse micro-oscillations in Figure A.5.

R	Ψ	α	β	β_2	p_0	V_0
[ø]	[ø]	[m^2/s^2]	[m^4/s^4]	[m^4/s^5]	[Pa]	[in^3]
-0.505	2.372	0.384	-0.061	0	1.179×10^5	5.455

Appendix B

Bubble Breaching Theory

B.1 Repeatability and Energy

Signal repeatability is commonly measured in Normalised Root-Mean-Square deviation (NRMS). More precisely, NRMS is "*the normalised energy of the difference between two datasets*", D_1 and D_2 calculated by Eq (B.1) *(Lecerf et al., 2015)*.

$$NRMS(D1, D2) = 2 \cdot \frac{RMS(D_2 - D_1)}{RMS(D_2) + RMS(D1)} \tag{B.1}$$

Like Eq. (3.1), the equation for calculating deviation used in the inverse-modelling, Eq. (B.1) compares the datasets index-to-index. This makes them sensitive to repeatable noise, and further accentuates the importance of minimising it. RMS, of which the formula is written in Eq. (B.2), is a measure of the power in the signal. It can be visualised as the area under the line made if all negative peaks in the dataset were rectified and the resulting curve averaged.

$$RMS(D) = \sqrt{\frac{1}{N}\sum_{i=1}^{N}|D_i|^2} \tag{B.2}$$

The theoretical values possible for an NRMS plot lies within the range of 0 (the datasets being the same) to 2 (one of the datasets being zero-valued or the two being anti-correlated). Furthermore, a value of $\sqrt{2} \approx 1.41$ indicates that both datasets contain random noise *(Kragh and Christie, 2002)*. From such background knowledge, it was for this thesis postulated that NRMS plots constructed of bubble signals would experience two main trends: At first the main bubble is the dominant source of energy. The signals produced

by it are repeatable, but diminish in strength as recording time progresses. When plotting the NRMS values over time it is thus natural to expect them to start off low, but experiencing a gradual increase as the main bubble becomes weaker and less influential. Seeing as bubbles lose most of their internal energy in the contraction-expansion transition, the energy emitted in a pressure pulse is in large part inversely proportional to the number of oscillations preceding the emission. Taking the Rayleigh-Willis equation for bubble period τ as a starting point and assuming a constant bubble rise velocity v_r, one can relate the recording time and source depth to number of oscillations η using an unknown constant k as follows.

$$\eta(t) = \frac{t}{\tau} = tk\frac{(z(t)+10)^{5/6}}{(p_0V_0)^{1/3}} = kt(z_{t=0} - v_r t + 10)^{5/6} \tag{B.3}$$

Note that this formula is not exact; in reality bubble rise velocity increases at every contraction (until reaching a terminal velocity), and the equation does not take into account changes in pressure and volume. It is nevertheless roughly proportional to the number of oscillations experienced by a bubble under known initial conditions. Equation (B.3) thus implies that the rate of energy dissipation, and therefore the speed of NRMS convergence to $\sqrt{2}$, is proportional to the source depth. This trend of faster convergence with depth is likely to be further reinforced by the fact that the main bubble splits off daughter bubbles after each collapse through turbulence, and in the process decreases in sphericity. If, however, the main bubble reaches the surface before its dominance of the ambient noise wanes this trend should reverse, resulting in *increased* time for NRMS convergence with depth.

B.2 Depth, Temperature and Cavitation

For cavitation to occur, a point in the water needs to reach the water saturation pressure. This pressure is largely decided by temperature, and can be determined using the Clausius-Clapeyron equation:

$$p_{Sat} = p_{atm} e^{\Delta H_{vap}(1/T_{Boil} - 1/T_{Sat})/R_G} \tag{B.4}$$

Here R_G and ΔH_{vap} are respectively the universal gas constant (8.3145 J mol^{-1} K^{-1}) and the latent heat of vaporisation (for water equal to 40650 J mol^{-1}). With a boiling temperature of 373.15 K (at atmospheric pressure p_{atm}) and an ambient temperature of 277.15 K, the saturation pressure is calculated to be 1080 Pa.

B.2.1 Bubble Wall Velocity and Cavitation

In *Landrø et al. (1993)*, a method is developed for calculating the critical jet velocity for water guns necessary to create cavitation. This theory is easily modified for air guns to determine the minimum bubble-wall velocity necessary to cause the same phenomenon at each source depth. By assuming incompressibility and neglecting gravity, Bernoulli's equation can be written for a point in the water close to the bubble wall, and one further away. The primer is assumed to move with the speed of the bubble wall, and the second is taken to be stationary ($c_2 \approx 0$). For the cavities to form at this first point, the water will need to be at the vapour saturation pressure (earlier calculated to be 1080 Pa at 277 Kelvin). This pressure is magnitudes lower than the hydrostatic pressure at the second point. Bernoulli's equation can due to these assumptions be simplified to

$$\begin{aligned} p_{Sat} - p_\infty =& \frac{1}{2}\rho(c_2^2 - \dot{R}^2) \\ p_\infty \approx& \frac{1}{2}\rho\dot{R}^2. \end{aligned}$$

The minimum bubble wall velocity necessary to cause cavitation in its vicinity is thus found by solving for $\dot{R}$.

$$\dot{R} = \sqrt{\frac{2p_\infty}{\rho}} \tag{B.5}$$

Equation (B.5) has been plotted against depth in Figure B.1.

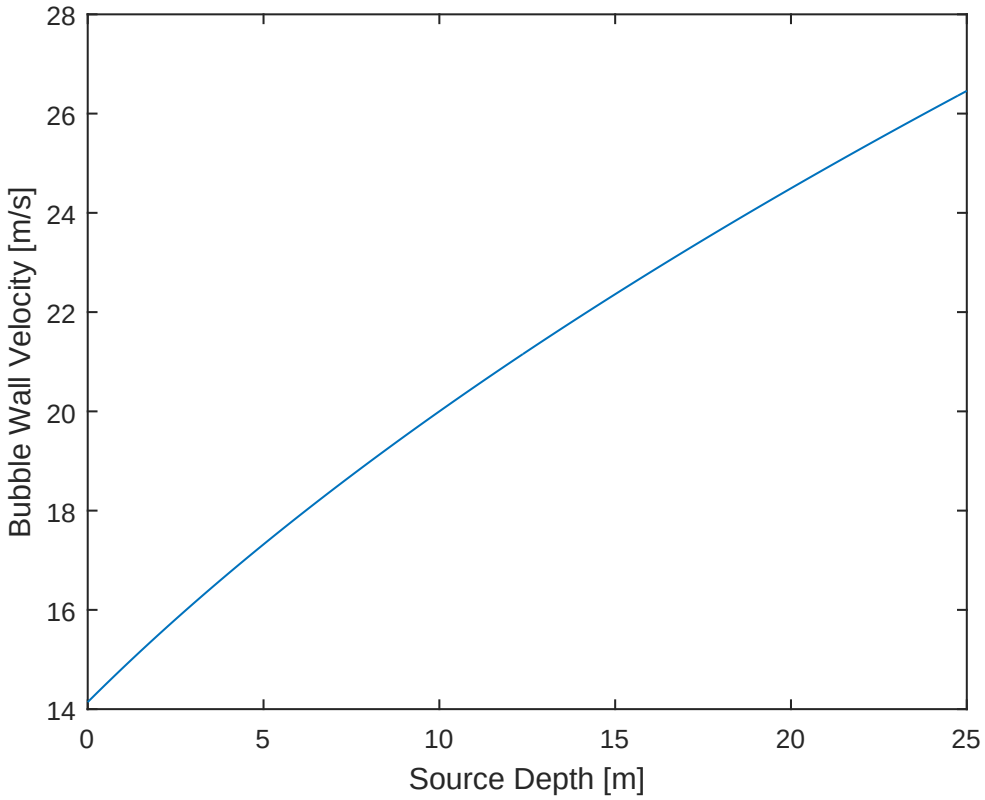

Figure B.1: The critical bubble wall velocity for causing cavitation as described by Eq. (B.5) plotted over depth. The actual values require experimental testing, but the overall trend observed is likely to be valid.